Title
Measurement and Quantum State Transfer in Superconducting Qubits

Author
Mlinar, Eric

Publication Date
2016

UNIVERSITY OF CALIFORNIA
RIVERSIDE

Measurement and Quantum State Transfer in Superconducting Qubits

A Dissertation submitted in partial satisfaction
of the requirements for the degree of

Doctor of Philosophy

in

Electrical Engineering

by

Eric Mlinar

March 2017

Dissertation Committee:

Dr. Alexander Korotkov, Chairperson
Dr. Ilya Dumer
Dr. Roger Lake

The Dissertation of Eric Mlinar is approved:

Committee Chairperson

University of California, Riverside

Acknowledgments

I am incredibly grateful for so many positive influences throughout my life that have led me to completing this dissertation. “To whom much is given, much will be required” — I hope that, beyond this thesis, I can do well with all the gifts that I have been given, from great friends, colleagues, and family, and that I can return the favor whenever the opportunity presents itself.

I first want to thank all my colleagues in the Quantum Computing And Measurement Physics (QCAMP) group who have helped me develop over the years. The post-doctoral scholars have been immensely informative, helpful, and generous with their time. To Eyob Sete, with your positive spirit, I thank you for patiently (and repeatedly) explaining various mechanics of quantum physics and gently helping me with my first steps on the road to a doctorate. To Justin Dressel, I thank you for all your keen physics and professional insights and many interesting discussions. To Juan Atalaya, I thank you for your tireless assistance with this dissertation; you have been a great example to me of humble service. I also want to thank my comrade-in-arms, Mostafa Khezri, who will be left to hold the fort as the lone Ph.D. student in QCAMP (and is my nomination for the prestigious lab safety coordinator opening that I leave). It was a privilege to be a collaborator with you, and I am excited to see what great things lie ahead in your future.

Next, I am grateful to the staff of the Electrical and Computer Engineering department; in particular, William Bingham, Trudi Loder, and Adrienne Thomas. I doubt that it is usual for a department staff to be so supportive, so thank you.

I want to thank my family, especially my father who has always been willing to put in that extra hour to help me on my latest project, or a troublesome paragraph in my dissertation. To my mother, thank you for your complete and total support. Thank you to Alison and Rebecca, my sisters, who give me great encouragement and invest themselves in keeping our family close. And of course, thank you to my Julia, my wife, for doing all in your power to pave the path for my success.

I also want to acknowledge all the friends who have supported me and helped me get to this point, especially the folks at UCLA, Hank Lopez, and all the people at the Tilden Study Center.

Finally, I want to thank my advisor, Dr. Alexander Korotkov, who has been the model of a gentleman for me. He has led by example in all things, especially hard work. He never asks of any of us what he is not already giving himself — a genuine lesson in leadership. The fact that he has a singular, uncanny intuition when it comes to all things physics-related is also an invaluable addition from an advisor. Thank you, Sasha; I hope that one day I will know “high school level” quantum physics as well as they know it at that level in Russia (a running joke within our group).

Financial Support. I would like to acknowledge the support that I received from the following funding agencies and grants. Support for this work was provided by the Graduate Assistance in Areas of National Need (GAAAN) fellowship from the Department of Education. It was also supported by Army Research Office (ARO) Grants W911NF-10-1-0334, W911NF-15-1-0496, and W911NF-11-1-0268.

Academic Publications in this Work. The text of this dissertation incorporates material presented in the following journals and conference presentations.

Journal Articles:

- M. Khezri, E. Mlinar, J. Dressel, A. N. Korotkov, "Measuring a transmon qubit in circuit QED: dressed squeezed states," *Phys. Rev. A*, vol. 94, p. 012347, Jul 2016.

  `http://journals.aps.org/pra/pdf/10.1103/PhysRevA.94.012347`

- E. A. Sete, E. Mlinar, and A. N. Korotkov, "Robust quantum state transfer using tunable couplers," *Phys. Rev. B*, vol. 91, p. 144509, Apr 2015.

  `http://journals.aps.org/prb/pdf/10.1103/PhysRevB.91.144509`

- E. A. Sete, A. Galiautdinov, E. Mlinar, J. M. Martinis, and A. N. Korotkov, "Catch-disperse-release readout for superconducting qubits," *Phys. Rev. Lett.*, vol. 110, p. 210501, May 2013.

  `http://journals.aps.org/prl/pdf/10.1103/PhysRevLett.110.210501`

Conference Presentations:

- E. Mlinar, Mostafa Khezri, J. Dressel, and A. N. Korotkov, "Analysis of non-adiabatic effects in circuit QED measurement of a transmon," in *APS Meeting Abstracts*, Mar 2016.

  `http://meetings.aps.org/Meeting/MAR16/Session/P48.8`

- E. Mlinar, E. A. Sete, and A. N. Korotkov, "Robust quantum state transfer using flying microwave qubits," in *APS Meeting Abstracts*, Mar 2015.

  `https://meetings.aps.org/Meeting/MAR15/Session/A39.10`

- E. A. Sete, E. Mlinar, A. N. Korotkov, A. Galiautdinov, and J. M. Martinis, "Catch-disperse-release readout for superconducting qubits," in *APS Meeting Abstracts*, Mar 2013.

  `http://meetings.aps.org/Meeting/MAR13/Session/U25.9`

- E. A. Sete, A. Galiautdinov, E. Mlinar, J. M. Martinis, and A. N. Korotkov, "Catch-disperse-release readout for superconducting qubits, in *The 43rd Winter Colloquium on the Physics of Quantum Electronics*, Jan 2013.

- E. Mlinar, E. A. Sete, A. Galiautdinov, J. M. Martinis, and A. N. Korotkov, "Superconducting qubit readout using capture-disperse-release of a microwave field," *Southwest Quantum Information and Technology Workshop*, Santa Barbara, CA: Feb 21-23, 2013. Poster.

  `http://physics.unm.edu/SQuInT/2013/abstracts.php?type=poster`

- E. Mlinar, E. A. Sete, A. Galiautdinov, A. N. Korotkov, and J. M. Martinis, "Superconducting qubit readout using capture-disperse-release of a microwave field," *APS March Meeting*, Baltimore, MD: Mar 18-22, 2013. Poster.

  `http://meetings.aps.org/Meeting/MAR13/Session/H1.294`

- E. Mlinar, E. A. Sete, A. Galiautdinov, J. M. Martinis, and A. N. Korotkov, "High-fidelity readout for superconducting qubits via catch, dispersion, and release of a microwave field," *IV Quantum Information School and Workshop*, Paraty, Brazil: Aug 5-16, 2013. Poster.

To my beautiful wife, Julia, and to the fruits of our love:

those that may come, and the one well on her way.

Deo gratias.

ABSTRACT OF THE DISSERTATION

Measurement and Quantum State Transfer in Superconducting Qubits

by

Eric Mlinar

Doctor of Philosophy, Graduate Program in Electrical Engineering
University of California, Riverside, March 2017
Dr. Alexander Korotkov, Chairperson

The potential of superconducting qubits as the medium for a scalable quantum computer has motivated the pursuit of improved interactions within this system. Two challenges for the field of superconducting qubits are measurement fidelity, to accurately determine the state of the qubit, and the efficient transfer of quantum states. In measurement, the current state-of-the-art method employs dispersive readout, by coupling the qubit to a cavity and reading the resulting shift in cavity frequency to infer the qubit's state; however, this is vulnerable to Purcell relaxation, as well as being modeled off a simplified two-level abstraction of the qubit. In state transfer, the existing proposal for moving quantum states is mostly untested against non-idealities that will likely be present in an experiment. In this dissertation, we examine three problems within these two areas.

We first describe a new scheme for fast and high-fidelity dispersive measurement specifically designed to circumvent the Purcell Effect. To do this, the qubit-resonator interaction is turned on only when the resonator is decoupled from the environment; then, after the resonator state has shifted enough to infer the qubit state, the qubit-resonator interaction is turned off before the resonator and environment are recoupled. We also show that the effectiveness of this "Catch-Disperse-Release" procedure partly originates from quadrature squeezing of the resonator state induced by the Jaynes-Cummings nonlinearity.

The Catch-Disperse-Release measurement scheme treats the qubit as a two-level system, which is a common simplification used in theoretical works. However, the most promising physical candidate for a superconducting qubit, the transmon, is a multi-level system. In the second work, we examine the effects of including the higher energy levels of the transmon. Specifically, we expand the eigenstate picture developed in the first work to encompass multiple qubit levels, and examine the resulting changes to the system. In particular, we analyze the population of the non-target eigenstates as a result of this expanded model, and provide an analytical form for these deviations from the simpler model in Catch-Disperse-Release (i.e., the dressed state approximation).

Lastly, we assess the robustness of the existing quantum state transfer protocol, testing its performance under typical experimental deviations from the ideal case. We show that the procedure is resilient to almost all non-idealities, except frequency mismatch between the two cavities. We also demonstrate a method to compensate for one such error in frequency-matching.

Contents

List of Figures

Chapter 1

Introduction

1.1 Motivation

A marriage between two of the greatest scientific developments in the twentieth century, quantum mechanics and the digital computer, could provide the twenty-first century with the next big leap in information processing in the form of the quantum computer. Made possible by the introduction of quantum algorithms, quantum information processing will allow for major breakthroughs in some traditionally difficult areas of computation. Specifically, several known quantum algorithms will run significantly faster than their classical counterparts. One of the most prominent examples is Shor's algorithm, which can solve integer factorization exponentially faster than known classical algorithms, and therefore has huge implications in the decryption of modern day communication security protocols.

The great enthusiasm for quantum information processing is tempered by the main prerequisite of the field: the implementation of quantum algorithms necessitates access to a controllable quantum system — a quantum computer. Such a device incorporates and directly takes advantage of quantum mechanical behavior to implement algorithms which are impossible for a classical computer to perform.

Two properties intrinsic to the quantum computing system which make this advancement possible are quantum superposition and quantum entanglement. Whereas a classical binary digit (bit) can only be in one of two possible states (e.g. "zero" or "one"; "false" or "true"), its quantum analogue, the quantum bit (qubit), can exist in any linear combination of these two states. That is, a qubit can be in a superposition of both "zero" and "one" states simultaneously. Entanglement allows this superposition to be extended over multiple qubits. These characteristics can be used to create a seemingly highly-parallel computing device and are exploited by quantum algorithms.

However, these potential benefits come with a new set of challenges. It is a difficult task to physically implement a controllable qubit, and then also to keep it coherent long enough to interact with it in some desired manner. In the search for an appropriate system, realizations of qubits have been designed in many different physical domains. The list can be split into two categories: traditional quantum systems (e.g., nuclear spins and trapped ions) and artificial ones (e.g., quantum dots and superconducting qubits), with each having its own advantages and disadvantages. The work presented in this dissertation focuses on the use of artificial atoms in superconducting circuits, but even in this promising domain, progress towards a scalable quantum computer remains difficult.

Nevertheless, efforts in this field can lead to greater knowledge of quantum physics, regardless of the fate of the quantum computer. For example, the characterization of quantum systems can be used to study the behavior of quantum systems in general. From a scientific standpoint, the field of quantum information will likely be greatly developed under current pursuits. Even for those who are skeptical a quantum computer will ever be realized, the quest for one provides a rich medium for scientific learning. Thus, the advancement of superconducting qubits as a subset of quantum computing can play a major role in both the progress towards a scalable quantum computer, as well as the study of fundamental quantum mechanics and quantum information processing.

Before moving into a discussion of superconducting qubits and concepts related to the main work of this dissertation, we will first review some general aspects of quantum computing. A good overview of this topic can be found in Ref. [1], but a brief introduction will be presented here. We will start with quantum information processing, including a short synopsis of quantum algorithms, qubits, and quantum operations. We will then briefly examine the various domains for the physical realization of a qubit.

1.2 Quantum Information Processing

1.2.1 Quantum Algorithms

The enthusiasm for quantum computing has its origins in the development of quantum algorithms because of the signifcant speedup that these algorithms offer over classical ones for a variety of applications. It is the need for a quantum computer to perform these algorithms which fuels the current quest for one. We therefore begin with a brief overview of the development of quantum algorithms.

Richard Feynman is credited with the initial proposal of a quantum computer, when in 1982 he suggested the use of one for simulating quantum systems [2]. The next big event for quantum information processing occurred in 1985 when David Deutsch challenged the strong Church-Turing thesis, proposing that quantum algorithms cannot be efficiently simulated with a classical Turing machine [3]. The initial Deutsch algorithm was a toy problem, set up to determine whether a function is constant or balanced — essentially, whether a coin toss is fair or not. This algorithm was improved in 1992 to include a system of many binary-valued inputs and is known as the Deutsch-Jozsa algorithm [4].

One of the most influential developments came in 1994 with Shor's algorithm, which solves integer factorization and the discrete logarithm problem [5]. Because integer factorization is the mechanism of security in the popular RSA encryption method of public-key cryptography, the implementation of this algorithm has far-reaching consequences to communication security. Whereas a classical computer will take super-polynomial time to factorize a number (and for modern day security, a solution to the classical algorithm, even on a super-computer, can take longer than the lifetime of the universe), Shor's algorithm run on a quantum computer does this in polynomial time, conceivably within a single day. In addition to decryption, quantum encryption schemes have been proposed that would provide completely secure communication [6].

Another notable quantum algorithm is Grover's algorithm, which can run a search through an unordered database quadratically faster than known classical algorithms: runtime of $\mathcal{O}(\sqrt{N})$ compared to $\mathcal{O}(N)$ classically [7], where N is the database size. While not exponential, such speedups in search algorithms are highly sought after. There are numerous other quantum algorithms, and as the list grows, so too the interest in a quantum computer which can apply them.

1.2.2 Qubits

Simply put, a qubit is a quantum system with two energy levels (or eigenstates). Below, we briefly discuss two important properties of qubits, quantum superposition and entanglement, as well as their mathematical description in terms of density matrices.

1.2.2.1 Quantum Superposition

Following the conventional notation for the states of classical bits (0 or 1), the two eigenstates of the qubit are usually denoted, using bra-ket notation, by $|0\rangle$ (e.g., the lowest energy level) and $|1\rangle$. Unlike classical bits, however, the qubit state is not confined to $|0\rangle$ or $|1\rangle$; it can be any linear combination of these two states.

This property is known as the principle of quantum interference or superposition (similar to the superposition of classical waves). More precisely, the state of, say, qubit "α" is given by the wavefunction

$$|\psi_\alpha\rangle = \alpha_0 |0\rangle + \alpha_1 |1\rangle \,, \tag{1.1}$$

where the coefficients α_0 and α_1 are, in general, complex, and satisfy the normalization condition, $|\alpha_0|^2 + |\alpha_1|^2 = 1$. In this superposition state, the qubit interacts with its environment through both eigenstates simultaneously, with interaction strength proportional to the coefficients α_0 and α_1.

The quantum superposition is generally destroyed by the act of measurement (in the considered case, the measured quantity is the qubit energy). According to the postulate of orthodox collapse [8], after the measurement, the state $|\psi_\alpha\rangle$ is collapsed to state $|0\rangle$ with probability $P_0 = |\alpha_0|^2$ or to state $|1\rangle$ with probability $P_1 = |\alpha_1|^2 = 1 - P_0$.

The qubit state $|\psi\rangle_\alpha$ is often depicted by the Bloch vector $\mathbf{r} = (x, y, z)$ on the Bloch sphere: $|\mathbf{r}| = 1$. The Bloch coordinates for the considered state are defined by

$$x = 2\,\mathrm{Re}[\alpha_0 \alpha_1^*], \;\; y = -2\,\mathrm{Im}[\alpha_0 \alpha_1^*], \;\;\text{ and }\;\; z = |\alpha_0|^2 - |\alpha_1|^2. \tag{1.2}$$

Note that, in the Bloch representation, the eigenstates $|0\rangle$ and $|1\rangle$ are at the poles of the Bloch sphere, as shown in Fig. 1.1.

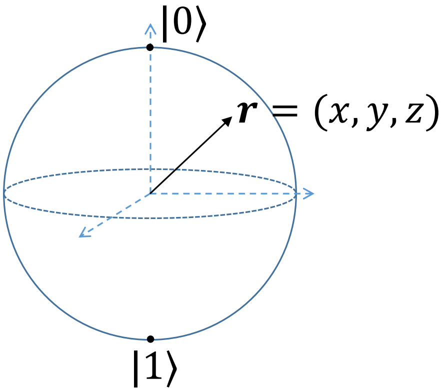

Figure 1.1: The Bloch sphere. The Bloch vector $\mathbf{r} = (x, y, z)$ depicts a qubit state. For pure states, e.g. $|\psi\rangle_\alpha$ in Eq. (1.1), the Bloch vector is on the surface of the Bloch sphere ($|\mathbf{r}| = 1$), as can be shown from the transformation Eq. (1.2). For mixed states, the Bloch vector is inside the sphere ($|\mathbf{r}| < 1$).

1.2.2.2 Quantum Entanglement

Let us now discuss the state of a two-qubit system, formed by the qubit "α" mentioned above and another qubit "β" (physically separated and not interacting with qubit "α"), with wavefunction of the form Eq. (1.1), but with coefficients β_0 and β_1. The state of this two-qubit system can either be entangled or not.

When the two-qubit state is not entangled, measurement of one qubit does not affect the state of the other qubit. This situation is an analog to two independent classical systems. The wavefunction in this case is just the product of the two individual wavefunctions; that is,

$$\begin{aligned} |\psi_{\text{non-entangled}}\rangle &= |\psi_\alpha\rangle\,|\psi_\beta\rangle \\ &= \alpha_0\beta_0\,|0\rangle_\alpha\,|0\rangle_\beta + \alpha_0\beta_1\,|0\rangle_\alpha\,|1\rangle_\beta + \alpha_1\beta_0\,|1\rangle_\alpha\,|0\rangle_\beta + \alpha_1\beta_1\,|1\rangle_\alpha\,|1\rangle_\beta\,. \end{aligned} \tag{1.3}$$

From Eq. (1.3), we find that the joint probability distribution for the measurement result combination i, j is equal to $P(i, j) = P_i^{(\alpha)} P_j^{(\beta)}$ (for $i, j = \{0, 1\}$), where $P_i^{(\alpha)} = |\alpha_i|^2$ and $P_i^{(\beta)} = |\beta_i|^2$. This joint probability distribution is what we would expect for independent classical systems.

However, quantum mechanical systems are richer than classical ones and can "entangle" with each other. For the considered two-qubit system, the following wavefunction is also allowed

$$|\psi_{\text{entangled}}\rangle = \frac{1}{\sqrt{2}} \left(|0\rangle_\alpha |0\rangle_\beta + |1\rangle_\alpha |1\rangle_\beta \right) . \tag{1.4}$$

The system in the above entangled state (one of the famous Bell states, or EPR pairs [9]) has the peculiarity that if we perform a measurement on, say, qubit "α" and obtain the result, say, zero (with 50% chance), then we immediately collapse the state of the other qubit to $|0\rangle_\beta$ with 100% certainty. Note that this entanglement property does not rely on any physical interaction between the qubits, and the spatial separation between them can be arbitrarily large.

This cause-effect interaction seemingly violates Einstein's theory of relativity, but there is an important restriction: although some effect travels faster than the speed of light, no useful (i.e., classical) information is transmitted. As such, in order to extract some meaningful information, the two observers must still communicate with each other classically [1].

1.2.2.3 Density matrix

When working with the wavefunction notation for quantum systems, the implication is that the system is fully defined (i.e., we have complete information).

These examples of perfect information are known as “pure” states. While these are commonly assumed in theory, the case is different in the real world. For instance, experimental systems are constantly interacting with their environment in a way which is impossible to perfectly describe, nor are measurements of the system itself perfect (e.g., output signals of detectors have noise strength larger than that of ideal, quantum-limited detectors [10]). As a result, the state of a system is often defined as a mixture (not a superposition) of possible pure states. Such type of states are called “mixed” states.

Both pure and mixed states are mathematically described by density matrices (or density operators) [11, 1]

$$\hat{\rho} = \sum_i p_i \left|\psi_i\right\rangle \left\langle\psi_i\right|, \tag{1.5}$$

where each term represents a pure state, $\left|\psi_i\right\rangle \left\langle\psi_i\right|$, and the weighting factors p_i (probabilities) reflect our uncertainty about what the exact state of the system is. We also have the normalization condition $\sum_i p_i = 1$. Note that, while pure states may be represented in terms of wavefunctions [see Eqs. (1.1), (1.3) and (1.4)], mixed states cannot.

The density matrix, $\hat{\rho}$, is a Hermitian matrix ($\hat{\rho}^\dagger = \hat{\rho}$) with unit trace. For a qubit, it has the form ($\rho_{01}^* = \rho_{10}$, $\rho_{00} + \rho_{11} = 1$)

$$
\begin{aligned}
\hat{\rho} =& \begin{bmatrix} \rho_{00} & \rho_{01} \\ \rho_{10} & \rho_{11} \end{bmatrix} \\
=& \rho_{00} \left|0\right\rangle \left\langle 0\right| + \rho_{01} \left|0\right\rangle \left\langle 1\right| + \rho_{10} \left|1\right\rangle \left\langle 0\right| + \rho_{11} \left|1\right\rangle \left\langle 1\right| . \qquad (1.6)
\end{aligned}
$$

The diagonal elements have the classical interpretation of probabilities (i.e. $\rho_{00} = P_0$ and $\rho_{11} = P_1$). A visual representation of Eq. (1.6) can be achieved by using the Bloch parametrization

$$\hat{\rho} = \frac{1}{2}\left(1 + x\sigma_x + y\sigma_y + z\sigma_z\right), \qquad (1.7)$$

where the Bloch vector is $\mathbf{r} = (x, y, z)$. The Bloch coordinates as defined in Eq. (1.7) apply to both mixed and pure states, and also agree with the definition in Eq. (1.2) for pure states. In Eq. (1.7), σ_x, σ_y, and σ_z are the Pauli matrices, defined as

$$\sigma_x = \begin{bmatrix} 0 & 1 \\ 1 & 0 \end{bmatrix}, \sigma_y = \begin{bmatrix} 0 & -i \\ i & 0 \end{bmatrix}, \text{ and } \sigma_z = \begin{bmatrix} 1 & 0 \\ 0 & -1 \end{bmatrix}. \qquad (1.8)$$

Physical states correspond to Bloch vectors, $\mathbf{r}$, inside of (mixed states) or on (pure states) the Bloch sphere, as depicted in Fig. 1.1.

When modeling experimental setups, pure states cannot handle the loss of information by the system, such as the introduction of noise, or other sources of decoherence that result in a mixed state. For this reason, although wavefunctions are generally easier to work with, the density matrix is often used in simulations, including results presented in this work (e.g., Sec. 3.4).

1.2.3 Quantum Operations

Quantum operations are, generally speaking, linear mappings which map one physically valid density matrix to another one. In particular, such mappings are trace preserving. Quantum (logic) gates are a type of quantum operations which can be regarded as unitary transformations performed on wavefunctions (or pure states). This implies that the operation is reversible (unlike most classical gates) and can be achieved by engineering some specific Hamiltonian. Below, we discuss some examples of quantum logic gates operating on states of one- and two-qubit systems. Quantum gates involving three or more qubits can be implemented in terms of one- or two-qubit quantum logic gates [12, 1].

Examples of one-qubit quantum logic gates are:

- **Pauli X, Y, and Z gates.** These are single-qubit operations represented by the Pauli matrices, see Eq. (1.8). In particular, the quantum gate $X \equiv \sigma_x$ (similarly, $Y \equiv \sigma_y$ and $Z \equiv \sigma_z$) is the analogue to the classical NOT gate; i.e.,

$$\text{If } \left|\psi\right\rangle = \alpha_0 \left|0\right\rangle + \alpha_1 \left|1\right\rangle , \text{ then } X \left|\psi\right\rangle = \alpha_1 \left|0\right\rangle + \alpha_0 \left|1\right\rangle . \tag{1.9}$$

- **Hadamard gate.** Represented by the unitary transformation, H,

$$H = \frac{1}{\sqrt{2}} \begin{bmatrix} 1 & 1 \\ 1 & -1 \end{bmatrix}, \tag{1.10}$$

  this creates a "cat" state, $(|0\rangle \pm |1\rangle)/\sqrt{2}$, from a state in the computational basis, $|0\rangle$ or $|1\rangle$, and vice-versa.

Again using the Bloch sphere as a visual aid, single-qubit gates are represented by rotations of Bloch vectors. For instance, the Pauli X (or NOT) quantum gate can be seen as a π-rotation about the x-axis.

Examples of two-qubit quantum logic gates are:

- **Swap gate.** This is a two-qubit gate that exchanges the states of the two qubits, it is represented by the unitary transformation, $SWAP$,

$$SWAP = \begin{bmatrix} 1 & 0 & 0 & 0 \\ 0 & 0 & 1 & 0 \\ 0 & 1 & 0 & 0 \\ 0 & 0 & 0 & 1 \end{bmatrix}, \tag{1.11}$$

  and it maps an initial two-qubit wave function $|\psi_{\text{in}}\rangle = \alpha_{00}|00\rangle + \alpha_{01}|01\rangle + \alpha_{10}|10\rangle + \alpha_{11}|11\rangle$ into $|\psi_{\text{f}}\rangle = \alpha_{00}|00\rangle + \alpha_{10}|01\rangle + \alpha_{01}|10\rangle + \alpha_{11}|11\rangle$.

- **Controlled-NOT.** This gate uses the state of one qubit (the control qubit) to determine if an operation on another qubit (the target qubit) is performed. If the control qubit is in the state $|1\rangle$, then the operation is performed on the target qubit; otherwise, no operation is done. This is achieved by the unitary transformation

$$CNOT = \begin{bmatrix} 1 & 0 & 0 & 0 \\ 0 & 1 & 0 & 0 \\ 0 & 0 & 0 & 1 \\ 0 & 0 & 1 & 0 \end{bmatrix}. \tag{1.12}$$

1.3 Physical Realizations of Qubits

Because of the potential benefits that motivate the desire for a quantum computer, there is a strong push to find the best physical realizations of qubits. While any two-level quantum system may be considered a qubit, the demands of a scalable quantum computer impose certain conditions which successful realizations have to satisfy.

1.3.1 Requirements

DiVincenzo formulated in 1997 five requirements for a quantum system to be a quantum computer [13, 14]. They are as follows:

1. The Hilbert space of the system is "precisely delineated" (a system of well-defined qubits).
2. The system must be able to create initial states (good state preparation).
3. It is isolated from coupling to the environment (low decoherence).

4. It is possible to subject the system to controlled sequence of unitary transformations (quantum gates are defined).
5. The system allows for a “strong” form of measurement (i.e., it can project the state to an eigenstate, or “measurement basis”).

Since 1997, there have been some refinements to these initial conditions. A 2010 publication on the state of quantum computing expanded on these to add the following [15]:

- **Scalability:** exponential growth of the Hilbert space without an exponential cost in resources (e.g. time, space, energy).
- **Universal Logic:** access to the system using finite set of control operations, for which the resources must also not scale exponentially.
- **Correctability:** extraction of the entropy of the computer to maintain a coherent state.

Creating a physical realization of qubits which meets all of the above requirements to make a functional, scalable quantum computer is an extremely challenging endeavor. Each of the necessary conditions is difficult by itself, albeit achievable, but these conditions have a general conflict with each other. For example, quantum systems should minimize interaction with the environment to avoid decoherence, but measurement and control necessarily involve this interaction. The realization of a quantum computer thus involves the more difficult goal of simultaneously controlling the quantum system, measuring it, and preserving its isolation from the environment.

1.3.2 Experimental Domains

Due to the challenges involved in the physical setup for quantum information processing, various different physical domains have been considered for the task. While advancing the understanding of quantum systems in each of these different areas is by itself already a worthwhile undertaking, the target for much of this research is finding the appropriate physical system for a scalable quantum computer. Here we provide a cursory glance at some of the domains that have been probed for their potential in quantum computing; this list is not exhaustive, but rather meant to provide some background on the efforts in this field, and it may not reflect the current state-of-the-art.

Nuclear Magnetic Resonance. One of the first systems explored experimentally for use as a quantum computer was nuclear magnetic resonance (NMR). By 1997, there were already proposed quantum computing schemes based on NMR [16, 17]. In 1998, it was employed to show experimental quantum error correction [18]. By 2001, simple forms of quantum algorithms had been demonstrated, for example: Deutsch's algorithm [19], the quantum Fourier transform [20], and Shor's factoring [21].

The popularity of NMR can be partially attributed to the broad research that already existed in the field by the 1990s, thanks to magnetic resonance technology (e.g. magnetic resonance imaging, or MRI). NMR quantum computing uses the nuclear spins in liquid state molecules as the two-level system (spin up or spin down). The advantages of this technology are that, first and foremost, it has great coherence times, with nuclei maintaining their spin orientation for many seconds [15]. Entanglement is produced through indirect coupling via molecular electrons. The main limitations of NMR are scalability (systems with more than 20 qubits are very challenging [22, 23]) and the difficulty to address individual qubits.

Trapped Atoms. We divide the field of trapped atoms into two main groups: trapped electrically charged atoms (ions), and trapped neutral atoms. The former of these is the "leading experimental playground in which to explore the evolution of quantum systems" [24], setting the benchmark for coherence times in relation to the time for initialization, measurement, and logical gate operations. The typical ion trap geometry is the linear radio frequency Paul trap [25, 26, 27], whereby the ions are confined by electrodes and spaced from mutual Coulomb repulsion between each other. An important ingredient is the laser-cooling (Doppler cooling) which lowers the atomic energy to the bottom of the trap, and special techniques can bring it almost to rest in the trap [28]. Entangling in these systems involves the direct interaction of atoms because of spacial proximity (e.g. Coulomb interaction of ions), and have reached 99% entangled state fidelities [29]. Initialization can be done through optical pumping for nearly perfect state preparation. Measurement takes advantage of state-dependent optical fluorescence for almost 100% efficiency in detection.

Despite this strong list of advantages, ion traps suffer from the limiting factor in many potential quantum computing domains: scalability. With enough ions present, laser-cooling becomes inefficient and decoherence increases. Tens of ion traps can presently be realized, even up to roughly a hundred, which is likely sufficient to demonstrate the potential of the quantum computer in a way that is intractable to classical computers [30]. Groups in the field are seeking to increase scalability further in a number of ways, including the use of a quantum charge-coupled device (QCCD) [31].

Trapped neutral atoms, sometimes referred to as cold atom systems, have not yet achieved the same remarkable results as their ion trap brethren. In these systems, arrays of neutrally-charged atoms form an optical lattice by using patterns of crossed laser beams to create potential wells [15, 32]. The challenges in this system include controlled initialization of, interaction with, and measurement of these atomic qubits.

Photons. All-optical systems have great access to highly coherent sources of qubits in the form of photons. One of the main limitations of photons is a biproduct of one of their greatest advantages, which is their lack of interaction with the environment. While this means coherence times for photons are very good, it also means that entangling photons together is very challenging, with the majority of successful quantum operations being based on one qubit [15] (with some exceptions [33]). Photons are often considered for their ability to carry quantum states over great distances in quantum communication, which ideally can integrate into other quantum systems.

Although only non-deterministic quantum computers are achievable with photons because of probabilistic photon sources [34, 35] and detectors [36, 37], recent efforts in the field seek to push beyond this in hybrid systems. Atom-photon interactions have been heavily studied, known as cavity quantum electrodynamics (QED) [38]. This also leads to studies in circuit QED [39], which is a significant development in the field of superconducting qubits.

Semiconductor Qubits. Semiconductor qubits include quantum dots and the use of dopants in solids. These quantum systems were among the original systems suggested for the realizations of qubits, with the quantum-dot-based Loss-DiVincenzo quantum computer proposed in 1998 to satisfy DiVincenzo's own criteria (previously mentioned in Sec. 1.3.1) [40]. One of the main advantages, shared with the superconducting field, is that semiconductor qubits can take advantage of the mature fabrication processes developed for the classical computer industry [41].

Computation in semiconductor qubits is typically based on two spin states: parallel and anti-parallel to an external magnetic field. Measurement in these systems involves a spin-to-charge conversion, either through a single electron transistor or a quantum point contact [42, 15]. One problem with use of these spin states is interaction with the nuclear spins in the substrate, which is a major source of decoherence. The use of nuclear-spin-free lattices (such as silicon and carbon) is able to avoid this, and there are several semiconductor qubit system realizations that demonstrate coherence times of seconds, compared to nanoseconds when nuclear spin interactions were present [43, 44]. The problem can also be avoided through the use of dynamical decoupling protocols [41]. While scalability remains a challenge similar to other fields, the recent advancements in the semiconducting qubit field, such as the many orders of magnitude improvement in coherence times, are very promising for quantum spintronics as well as the possibility of quantum information processing in this domain.

Superconducting Qubits. While an in-depth discussion of superconducting qubits follows in Ch. 2, here is a very brief glimpse of the field. As classical electrical circuits are used for present day information processing, it is natural to ask if similar circuit devices can be constructed for quantum computing. A known concern with classical circuits is their dissipation of energy, which creates high decoherence in a quantum system. This can explain one of the current limitations of the field: low coherence times of the qubits. Nonetheless, superconducting circuits, and in particular the use of the the Josephson junction (see Sec. 2.1), may provide the best prospects for the realization of a quantum computer.

The reason for such optimism comes from the most notable advantage of superconducting qubits: the potential for scalability. Because such devices can be constructed on 2-D wafers, similar to classical computing, known device-scaling techniques can be adapted for use in scaling up the number of qubits. This field of fabrication is already very mature thanks to today's [classical] computers. The main disadvantage for quantum computing with superconducting circuits is the difficulty of isolating these systems from their environment. Coherence times are still short in contrast to other domains, which makes their improvement a main goal. Other areas for improvement are the fidelity of measurement operations and quantum gates, as well as decreasing the time needed to perform these tasks.

1.4 Dissertation Outline

The dissertation is organized as follows. In Chapter 2, we discuss some aspects of superconducting qubits, relevant to the work presented in later chapters. In Chapter 3, we discuss an innovative measurement technique for faster and higher-fidelity determination of a qubit state by avoiding the Purcell effect. In Chapter 4, we continue the discussion of measurement, examining the effect of higher energy levels of transmons on the measurement physics. In Chapter 5, we consider the experimental viability of the state-of-the-art quantum state transfer protocol for superconducting systems, by examining the robustness of this protocol to experimental non-idealities. In Chapter 6, the key points of this work are highlighted with some concluding remarks.

Chapter 2

Implementation of Superconducting Qubits

Superconducting circuits can be used to create artificial atoms which satisfy the DiVincenzo criteria for a scalable quantum computer. These circuits can be constructed using many of the techniques that are already well-developed in the fields of integrated circuits and consumers electronics. In this chapter, we will discuss some of the basic principles of superconducting qubits, examine physical implementations of qubits in this domain, and also provide some background to the main body of work in this dissertation.

The microscopic theory of superconductivity was proposed in 1953 by Bardeen, Cooper, and Schrieffer ("BCS" theory), describing the resistanceless transport of electrons due to the interaction of electrons and atomic/molecular lattice vibrations (phonons) [45, 46]. The dependence of the critical temperature (T_C) for superconductivity on the nuclear mass of the material, known as the isotope effect, showed a reliance of superconductivity on the lattice vibrations, and not on the electrons alone [47, 48]. This electron-phonon interaction creates Cooper pairs, where two electrons are effectively coupled through the lattice vibrations (phonons). The bound pair acts as a single entity and exhibits Bosonic behavior, as the two electrons can condense into the ground state, which would normally violate the Pauli exclusion principle for two individual electrons (or any fermions). Below the critical temperature, the attractive force mediated by the positive ions in the lattice overcomes the usually-dominant force of Coulomb repulsion between the electrons.

One important observation from superconducting materials is that, although it is a macroscopic object with millions of particles, it exhibits quantum behavior. As such, it can be represented as a wavefunction, with an amplitude and phase component:

$$\Psi(\mathbf{r}, t) = |\Psi(\mathbf{r}, t)| \exp\left[i\theta(\mathbf{r}, t)\right], \tag{2.1}$$

where $\mathbf{r}$ is the spatial variable, and θ is the global phase. A superconducting ring then has one collective wavefunction, and the wavefunction is continuous along the wire. When the wavefunction loops back to original point, there can be no jump, so only changes of phase by factors of 2π are allowed.

The discrete nature of jumps in the wavefunction's phase may seem to conflict with the continuous modes of nature, for example, when a superconducting loop is exposed to an external flux. On the one hand, Faraday's law of induction states that the changing magnetic field induces an electric field (Lenz's law specifies this induced current acts to oppose the original magnetic flux) [49]. The Meissner effect states that the external magnetic field is expelled from inside a superconducting loop. Thus, the external flux should create an opposing flux in the ring via induced current. One the other hand, this change of current cannot break the wavefunction's continuity. The loop may acquire shifts in its phase, but they must obey the following relation:

$$\frac{\Delta\theta}{2\pi} = \frac{\Delta\phi}{\phi_0} = n, \tag{2.2}$$

where $\Delta\phi$ is the change of magnetic flux, $\phi_0 = h/2e = 2.07 \times 10^{-15}$ Wb is a single flux quantum, h is Planck's constant, e is the charge of an electron, and n takes integer values ($n = 0, 1, 2, ...$).

This leads to two conclusions. First, in the context of a loop of superconducting wire, phase and flux are interchangeable terms, with a relation given by Eq. (2.2). Second, flux displays discrete, quantized behavior, with allowed levels at integer multiples of ϕ_0. Below, we will show that breaking the continuity of this loop leads to the superconducting qubit.

2.1 Josephson Junctions

The standard Josephson junction is two superconducting electrodes separated by an insulated barrier (often an oxide), which acts as a tunnel junction between two superconducting wires. Josephson first demonstrated that a supercurrent, I, flows in such a device as [50, 51]

$$I = I_C \sin\varphi, \tag{2.3}$$

where I_C is the critical current, and φ is the difference between the global phase of each electrode's wavefunction, $\varphi = \Delta\theta$. If this junction is placed within a loop of wire, the loop no longer has a continuous wavefunction: a finite phase difference is allowed across the tunnel junction.

To model the Josephson junction in a superconducting loop, we break down its circuit contribution to a capacitive element (from the two electrodes separated by a short distance) and an inductive one (from the [super]current flowing in the loop). An important feature of this device is that the Josephson inductance is non-linear, which we show here.

From Eq. (2.3), we can extract $\dot{I} = I_C (\cos\varphi)\,\dot{\varphi}$, and from Faraday's Law, we have $V = (\phi_0/2\pi)\,\dot{\varphi}$. Substituting $\dot{\varphi}$ from the second equation into the first, we have the classical equation for an inductor,

$$V = \left(\frac{\phi_0}{2\pi I_C}\frac{1}{\cos\varphi}\right)\,\dot{I}, \tag{2.4}$$

with inductance, L, equal to the middle term in parentheses. We can further separate this term into the linear inductance, $\phi_0/(2\pi I_C)$, and the nonlinear component, $1/\cos\varphi$.

Whereas a standard (linear) LC circuit acts as a harmonic oscillator, nonlinear inductance creates an uneven spacing between subsequent energy levels in the system. This anharmonicity allows for unique energies for the transition between different states, providing a means to target specific levels of the system. A qubit can thus be engineered by isolating one such transition between states, creating a pseudo-two-level system. In this manner, the Josephson inductance is the basis for quantum computing in the superconducting domain.

The energy stored in a superconducting element is ($\Phi = \varphi\phi_0/2\pi$)

$$U = \int I \, d\Phi \tag{2.5}$$

Using the Josephson current definition in Eq. (2.3) and substituting the relation between phase and flux [e.g., in Eq. (2.2)], we find the energy stored in a Josephson Junction:

$$\begin{aligned} U &= -\frac{\phi_0}{2\pi} \; I_C \; \cos\varphi, \\ &= -E_J \; \cos\varphi, \end{aligned} \tag{2.6}$$

where $E_J \equiv (\phi_0/2\pi) \; I_C$.

2.2 Superconducting Qubits

The Josephson junction can be used in different circuit setups to provide the different "flavors" (types) of superconducting qubits. Using the anharmonicity of Josephson junction, as described in Sec. 2.1, these different architectures are capable of isolating two energy levels for use as a pseudo-two-level system.

The qubit must be engineered around common sources of decoherence, such background charge fluctuations, trapped magnetic eddies (flux loops in the substrate), or even preparation-related errors, such as not initializing in the desired state. For instance, even below T_C (experimental setups use a dilution refrigerator and typically operate at around T = 50mK or below [52]), higher energy states can be thermally populated, preventing localization in the ground state.

The various systems in which superconducting qubits are realized typically involve tradeoffs. In the process of engineering a setup that is less sensitive to decoherence from background charge noise, one might make the system more sensitive to stray magnetic fields. Similarly, making a system too insensitive to interactions, while improving coherence times, might adversely affect measurement or the use of quantum gates to manipulate the qubit state.

In this section, we will look briefly at each of the different setups used for superconducting qubits. One distinguishing characteristic is how localized (or "well-defined") specific observables are within a system. Flux and charge are conjugate operators, $[\phi, q] = i\hbar$, which can alternatively be expressed in terms of phase and number of Cooper pairs, $[\varphi, N] = i$. To determine which term is well-defined, the ratio between the Josephson coupling energy, $E_J = I_C\phi_0/2\pi$, and the charging energy, $E_C \equiv (2e)^2/2C$, is compared. Lower values of E_J/E_C means that the charge, q, is well-defined, whereas higher values means that phase, φ, is the better-defined term [53].

2.2.1 Charge Qubit

The first realized superconducting qubit was the charge qubit [54], which is also referred to as the Cooper pair box because it involves an isolated island of superconducting wire for Cooper pairs between a Josephson junction and a

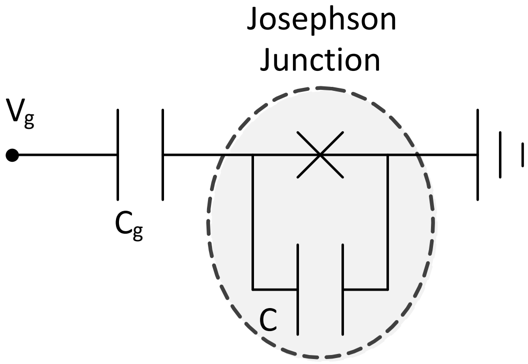

Figure 2.1: Circuit schematic of the charge qubit; the Cooper pair box exists between the capacitor, C_g and the Josephson junction (which is represented by both its capacitive component, C, and its Josephson tunneling component, which appears as a cross.

capacitor (as depicted in Fig. 2.1). The relevant quantum variable, the number of Cooper pairs that cross the junction, can be controlled by applying a voltage, V_g, as depicted in Fig. 2.1. For instance, a superposition of zero and one additional Cooper pairs on the island can be created. The gate charge that manipulates the number of Cooper pairs is $Q_g = V_g C_g$. Note that, as the charge is well-defined in this setup, phase is not ($E_J \approx E_C$).

The total electrostatic energy of the circuit is

$$E_{charge} = \frac{2e^2}{C_g}(n - n_g)^2, \tag{2.7}$$

where $n_g = C_g V_g / 2e$, with n assuming only integer values but n_g is a continuous variable defined by the gate voltage (and by the fabrication value of the capacitor C_g). The charging energy as a function of n_g and n is depicted in Fig. 2.2 (dashed lines).

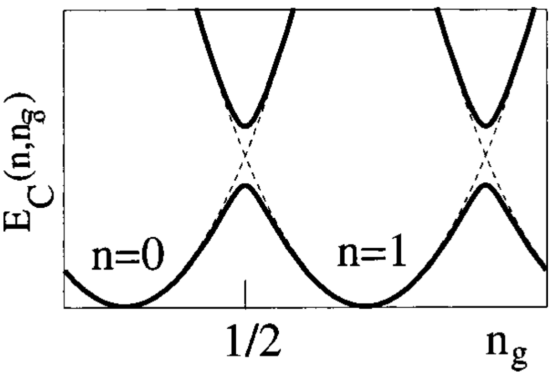

Figure 2.2: Graph of the total energy (solid lines) and charging energy (dashed lines) versus value of n_g in charge qubit system, as adapted from [52].

The Hamiltonian of this system is [53]

$$H = E_c\,(n - n_g)^2 - E_J \cos\varphi, \tag{2.8}$$

which is the Josephson junction (second term) with an added charging energy for the shunted capacitor (first term), as expected. Readout of these systems is accomplished through a single electron transistor (SET) [55], which is similar to a quantum point contact (QPC), both of which are sensitive electrometers.

A main disadvantage of charge qubits is their sensitivity to low-frequency ($1/f$) noise from background electrons. This major source of decoherence led to new designs for the charge qubit, for example the transmon (see Sec. 2.2.2) and the quantronium.

2.2.2 Transmons

The transmon qubit is a variation of the charge qubit, with higher values of E_J/E_C (although still far below those for the flux or phase qubits) [56]. This is done by shunting the Josephson junction with a large external capacitor. Compared to the charge qubit that was highly susceptible to background electric noise, the transmon is insensitive to such sources of decoherence. Because of its insensitivity to the environment, coupling to this system for measurement purposes is difficult; this will be discussed further in Sec. 2.3.

Higher values of E_J/E_C reduce the charge dispersion, and thus the sensitivity to charge noise; however, as this ratio increases, anharmonicity decreases, which reduces the distinguishability of particular state transitions. The transmon operates in the middle ground, $E_J/E_C \approx 50$, where the qubit is mostly immune to background charge, but still has unique transition energies in order to isolate two levels as a qubit.

The Hamiltonian can be reduced to the same form as the charge qubit:

$$H = 4E_C\left(n - n_g\right)^2 - E_J \cos\varphi. \tag{2.9}$$

An example of the eigenenergies vs. phase profile of the transmon is shown in Fig. 2.3. The lowest two energy levels, E_0 and E_1, are isolated as the two-level qubit. The transition energy between any two levels is given by $\omega_n = E_{n+1} - E_n$ ($\hbar = 1$), and from this we get the qubit frequency: $\omega_q = \omega_0 = E_1 - E_0$. The anharmonicity parameter, η, is defined as $\eta = \omega_1 - \omega_0 = (E_2 - E_1) - (E_1 - E_0)$.

These devices are considered an improvement over the previous flavors of qubits, and at present transmons have become the most popular of the superconducting qubits. Although the qubit is ideally a two-level system, it is clear

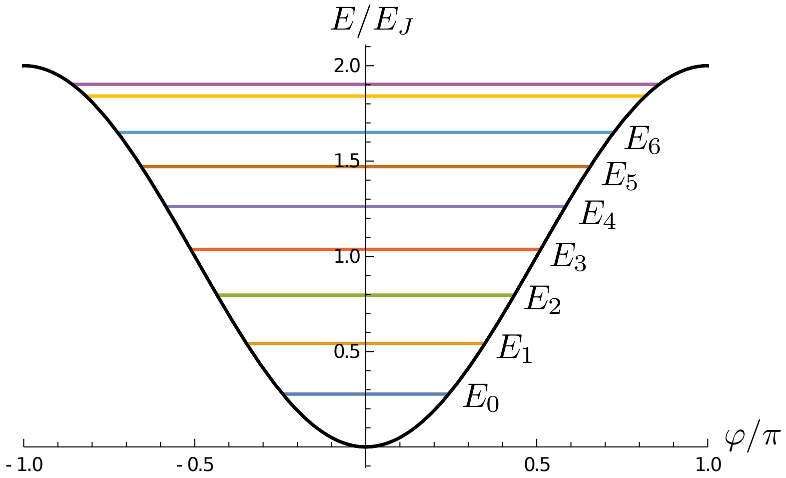

Figure 2.3: The potential of the transmon with respect to phase. Also shown (in color) are the lowest eigenenergy states, with the lowest two isolated to act as a qubit.

that the transmon has multiple higher levels which can be excited. A look at the effects of incorporating these higher levels into common theoretical models is the focus of the discussion found in Chapter 4.

2.3 Qubit State Readout and Preservation

The transmon (Sec. 2.2.2) has become the most popular superconducting qubit in current experimental setups. Its weak interaction with the environment leads to insensitivity to background charge noise, which is a major advantage, but also makes the measurement of its state difficult. A solution is adapted from Cavity QED in atomic physics and quantum optics, where the state of an atom inside a cavity is inferred from state-dependent changes to the cavity's transmission properties [57].

The same principle applies to an artificial atom and microwave resonator [39]: in circuit quantum electrodynamics (cQED) setups, a superconducting qubit is coupled to the electric field of a confined electromagnetic mode (resonator). The coupling is typically linear in the field and modeled by the Jaynes-Cummings (JC) Hamiltonian. In the dispersive measurement scheme, the state of the qubit is inferred from changes in the resonator frequency resulting from the qubit-resonator interaction. Note that in Chapter 4, we will extend the conventional JC model to include higher energy levels of transmon qubits and study the ring-up dynamics of this multi-level system coupled with a resonator.

The introduction of a resonator to interact with the transmon — an important feature in cQED setups to set, manipulate, and read the state of the qubit — unfortunately also adds sources of decoherence. We note here two useful performance parameters for the qubit: the energy relaxation rate (determined by, e.g., the Purcell effect), "T_1^{-1}", and the dephasing rate, "$(T_2)^{-1}$". The dephasing rate has contributions from energy relaxation and other mechanisms of dephasing; i.e., $(T_2)^{-1} = (2T_1)^{-1} + T_\varphi^{-1}$, where T_φ is the pure dephasing time.

In particular for transmons, the coupling of the qubit to a confined electromagnetic mode leads to an increase of its energy relaxation rate (i.e., it decreases the qubit T_1-time). Several ideas have been put forward to enhance the T_1- and T_2-times of transmon qubits; for instance, a Purcell filter may be used [58], or a tunable coupler can decouple the resonator from the continuum (physically represented by a transmission line). The latter idea is discussed in detail in Chapter 3.

2.3.1 cQED Dispersive Readout

Often used in atomic physics, quantum optics and, more recently, superconductor-based quantum circuits, the JC model describes the exchange of quanta between a two-level system and a harmonic oscillator, as shown by the following Hamiltonian

$$H = \hbar\omega_{\rm r}\left(a^\dagger a + \frac{1}{2}\right) + \frac{\hbar\omega_{\rm q}}{2}\sigma_z + \hbar g\left(a^\dagger\sigma_- + \sigma_+ a\right), \tag{2.10}$$

where $\omega_{\rm r}$ and $\omega_{\rm q}$ are the eigenfrequencies of the resonator and qubit, respectively. The creation and annihilation operators of quanta of the oscillator are, respectively, $a^\dagger$ and a. Similarly, the creation and annihilation operators for the qubit are σ_+ and σ_-, respectively. The last term in Eq. (2.10) is the coupling term, describing the coherent exchange of quanta between the oscillator and the qubit at a rate given by the coupling parameter g (assumed to be real for simplicity).

We now discuss the dispersive limit of large frequency detuning: $|\Delta| \gg g$, where $\Delta = \omega_{\rm q} - \omega_{\rm r}$. In this limit, there is no exchange of energy; however, the qubit can still modulate the oscillator eigenfrequency and vice versa. To see this, we first go to the rotating frame by applying the transformation, $U_{\rm rw}(t) = \exp[-i\omega_{\rm r}(a^\dagger a + \sigma_z/2)t]$. The Hamiltonian is then transformed to $H_{\rm rw} = \hbar\Delta\sigma_z/2 + \hbar g(a^\dagger\sigma_- + \text{h.c.})$. We then apply another unitary transfomation, U,

$$U = \exp\left[\frac{g}{\Delta}\left(a\sigma_+ - a^\dagger\sigma_-\right)\right], \tag{2.11}$$

so that the Hamiltonian, in the rotating frame, is transformed to $H_{\rm rw} \to U H_{\rm rw} U^\dagger$, which is approximately equal to (in the laboratory frame)

$$H \approx \hbar \left[\omega_{\mathrm{r}} + \frac{g^2}{\Delta} \sigma_z \right] a^\dagger a + \frac{\hbar}{2} \left[\omega_{\mathrm{q}} + \frac{g^2}{\Delta} \right] \sigma_z, \tag{2.12}$$

where we have neglected terms of cubic order in the coupling parameter, g, and dropped constant terms. In Eq. (2.12), the term $(\hbar g^2/\Delta)\sigma_z a^\dagger a$ is the effective dispersive coupling whereby the qubit modulates the eigenfrequency of the resonator and vice versa. This term leads to the ac Stark shift of the qubit eigenfrequency. Note also that the qubit frequency is shifted by g^2/Δ, which is known as the Lamb-shift.

2.3.2 The Purcell Effect

Ideally, we would like the qubit to be isolated from its environment in order to avoid loss of coherence and to protect its state; however, the processes of measuring the qubit and using gates to control it necessitate interaction, and this means complete isolation is not possible. In dispersive measurement, the qubit is coupled to a detuned readout resonator, and the qubit state is inferred by measuring the state-dependent phase shift of the leaked resonator field. In this setup, the qubit is indirectly coupled to the environment (i.e., the transmission line) via the resonator. This interaction of the qubit with its environment through the readout resonator will degrade the qubit lifetime, and is called the Purcell effect in cQED.

Let us now present a simple formula for the qubit energy decay rate due to the aforementioned process, called the Purcell rate. When the qubit is excited, there is a $(g/\Delta)^2$ probability that this excitation exists in the resonator. This is because of the eigenstate formation (hybridization) in the joint qubit-resonator system. The resonator energy decays with a rate κ, and this leads to the decay of the qubit excitation from the resonator with the same rate. As such the qubit experiences the rate of decay (Purcell rate) [39]

$$\Gamma_{\text{Purcell}} \approx \kappa \left(\frac{g}{\Delta}\right)^2 . \tag{2.13}$$

This is an approximate formula for the strong-dispersive-regime that can be useful for most practical purposes. For a more detailed analysis of the Purcell effect in cQED, see Ref. [59].

The Purcell effect reduces the qubit lifetime by decreasing T_1, and degrades qubit operations and measurement fidelities. However, this effect can be mostly avoided by using Purcell filters [58, 60, 61]. For example, Ref. [60] used a bandpass Purcell filter to avoid the excitation leakage at the qubit frequency, while allowing the readout pulse at the resonator frequency to leak. Fig. 2.4 shows the design of this Purcell filter that allowed for measurement fidelities of 99% within 150 ns.

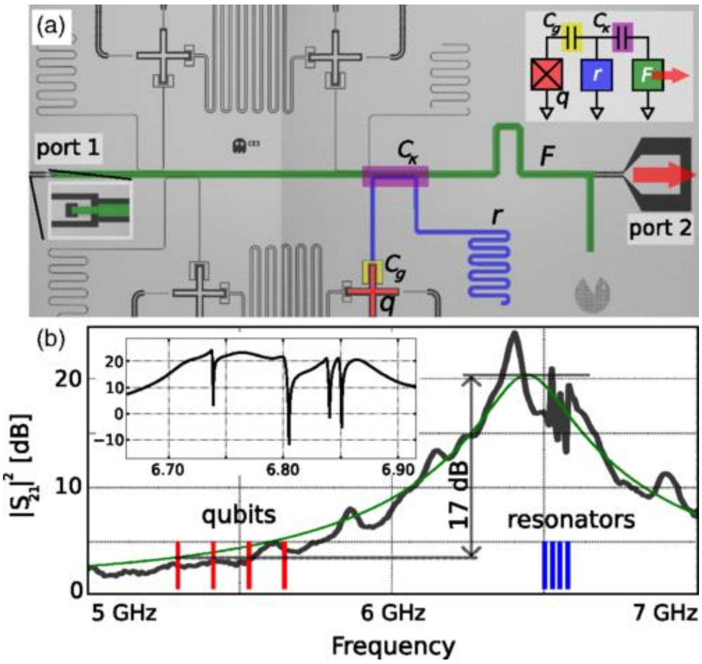

Figure 2.4: The Purcell filter (adapted from Ref. [60]). Panel (a) shows the optical micrograph, with the qubit (red), readout resonator (blue), and Purcell filter (green) in false color. The inset shows the lumped element circuit model of the device. Panel (b) shows the transmission spectrum of the device, with qubit frequencies shown in red and readout resonator frequencies in blue, showing that the bandpass filter masks qubit frequencies, while allowing photons at the readout frequencies to pass through.

Chapter 3

Catch-Disperse-Release Measurement

A new scheme for fast and high-fidelity measurement in superconducting qubits is the focus of this chapter. The main idea behind this single-shot readout is the use of a controlled catch, dispersion, and release of microwave field in the resonator. A tunable coupler decouples the microwave resonator from the transmission line during the dispersive qubit-resonator interaction, which circumvents harmful damping from the Purcell effect. If the qubit frequency in this scheme is sufficiently adiabatic, a fast and high-fidelity qubit readout is possible, even in the strongly nonlinear dispersive regime.

An interesting result from the research of this approach is the discovery that the Jaynes-Cummings nonlinearity leads to quadrature squeezing of the resonator field below the standard quantum limit. While scientifically interesting in itself, this additionally leads to a significant decrease in measurement error.

3.1 Introduction

One main source of error in the method of dispersive readout comes from the interaction of the qubit with the environment through its entanglement with the resonator. This is known from optics as the Purcell effect, and in cQED is the cavity-induced relaxation of the qubit from the coupling of the resonator to the outgoing transmission line [62]. There are several ways to minimize this negative effect. One may increase the detuning between the qubit and resonator, although this has the harmful side effect of slowing down the readout process. Some other recent proposals are the use of a Purcell filter [58], or use of a Purcell-protected qubit [63].

Another idea is that, because this decay happens only when there is significant coupling between the qubit and resonator as well as between the resonator and transmission line, the resonator-transmission coupling should be turned off while the qubit-resonator coupling is turned on. In this manner, the Purcell effect is avoided. To accomplish this, the measurement is divided into three operations: "catch", "disperse", and "release" of the microwave field. During the first two stages, a tunable coupler decouples the transmission line from the resonator, thus eliminating the Purcell effect.

During the "catch" phase, the initially empty resonator is driven by a microwave pulse and populated with $\sim$10 photons. At this stage the qubit is far detuned from the resonator [Fig. 3.1(b)], which makes the dispersive coupling negligible, leaving a coherent state (to high approximation) in the resonator. At the next "disperse" stage of the measurement, the qubit frequency is adiabatically

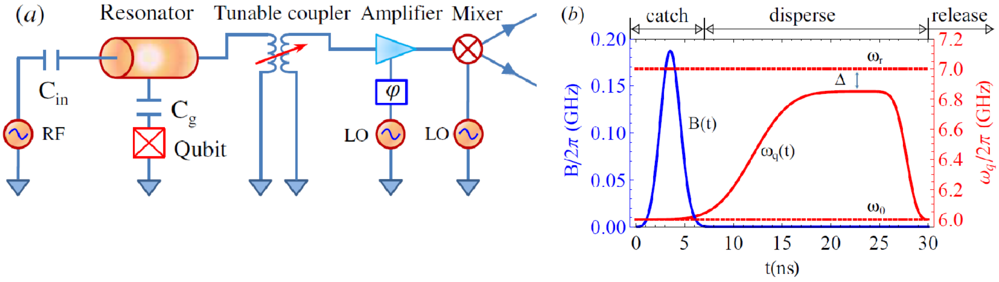

Figure 3.1: (a) Schematic of the measurement setup. The radio frequency (RF) source produces a microwave pulse, which populates the resonator via a small capacitor $C_{\rm in}$. The resonator photons then interacts with a capacitively ($C_{\rm g}$) coupled qubit. The interaction with the outgoing transmission line is controlled by a tunable coupler, which releases photons at the end of the procedure. The released field is then amplified and mixed with the local oscillator (LO) signal to be measured via homodyne detection. (b) The RF pulse $B(t)$ (blue curve) and varying qubit frequency $\omega_{\rm q}(t)$ (red curve), with approximate indication of the "catch", "disperse", and "release" stages. Dashed lines show the resonator frequency $\omega_{\rm r}$ and initial/final qubit frequency ω_0; $\Delta = \omega_{\rm r} - \omega_{\rm q}$ is the detuning at the "disperse" stage.

tuned closer to the resonator frequency to produce a strong qubit-resonator interaction (it may even be pushed into the nonlinear regime). During this interaction, the resonator field amplitudes ($\lambda_{\rm eff}$) associated with the initial qubit states $|0\rangle$ and $|1\rangle$ rapidly accumulate additional phases and separate in the complex phase plane [see Fig. 3.2(a)]. Finally, at the last "release" stage of the measurement, after the qubit frequency is again detuned from the resonator, the resonator photons are released into the outgoing transmission line. The signal is subsequently amplified (by a phase-sensitive parametric amplifier) and sent to the mixer where homodyne detection is performed.

With realistic parameters for superconducting qubit technology, we numerically show that the measurement of 30–40 ns duration can be realized with an error below 10^{-3}, neglecting the intrinsic qubit decoherence. The latter assumption requires the qubit coherence time to be over 40 μs, which is already possible experimentally [64]. It is interesting that because of the interaction nonlinearity [65, 66], increasing the microwave field beyond ∼10 photons only slightly reduces the measurement time. The nonlinearity also gives rise to about ∼50% squeezing of the microwave field (see [67, 68]), which provides an order-of-magnitude reduction of the measurement error.

3.2 Model

We consider a superconducting phase or transmon qubit capacitively coupled to a microwave resonator [Fig. 3.1(a)]. We use a two-level qubit as a simple approximation, while possible effects of the third level are discussed later. The system is described (as from Sec. 2.3) by the Jaynes-Cummings Hamiltonian [39] with a microwave drive ($\hbar = 1$),

$$\begin{aligned} H = {} & \omega_{\rm q}(t)\sigma_+\sigma_- + \omega_{\rm r}a^\dagger a + g(a\sigma_+ + \sigma_- a^\dagger) \\ & + B(t)a^\dagger e^{-i\omega t} + B^*(t)ae^{i\omega t}, \end{aligned} \tag{3.1}$$

where $\omega_{\rm q}(t)$ is the qubit's frequency (previously the atomic frequency "Ω"), g (assumed real) is the qubit-resonator coupling, and and ω is the effective frequency of the microwave drive. In this work we assume $\omega = \omega_{\rm r}$.

For the microwave drive $B(t)$ and the qubit frequency $\omega_q(t)$ [Fig. 3.1(b)], we use Gaussian-smoothed step-functions:

$$B(t) = \frac{B_0}{2}\left\{\mathrm{Erf}[\frac{(t-t_\mathrm{B})}{\sqrt{2}\sigma_\mathrm{B}}] - \mathrm{Erf}[\frac{t-t_\mathrm{B}-\tau_\mathrm{B}}{\sqrt{2}\sigma_\mathrm{B}}]\right\}, \text{ and} \tag{3.2}$$

$$\omega_\mathrm{q}(t) = \omega_0 + \frac{\Delta_0-\Delta}{2}\left\{\mathrm{Erf}[\frac{t-t_\mathrm{q}}{\sqrt{2}\sigma_\mathrm{q}}] - \mathrm{Erf}[\frac{t-t_\mathrm{qe}}{\sqrt{2}\sigma_\mathrm{qe}}]\right\} \tag{3.3}$$

where t_B, $t_\mathrm{B}+\tau_\mathrm{B}$, t_q, and t_qe are the centers of the front/end ramps, and σ_B, σ_q, and σ_qe are the corresponding standard deviations. In numerical simulations, we use $\sigma_\mathrm{B} = \sigma_\mathrm{qe} = 1$ ns (typical experimental value for a short ramp), while we use longer σ_q to make the qubit front ramp more adiabatic. Other fixed parameters are: $g/2\pi = 30$ MHz, $\tau_\mathrm{B} = 1$ ns, $t_\mathrm{B} = 3$ ns, $\omega_\mathrm{r}/2\pi = 7$ GHz, and $\omega_0/2\pi = 6$ GHz, so that initial and final detuning $\Delta_0 = \omega_\mathrm{r} - \omega_0$ is 1 GHz, while the disperse-stage detuning Δ is varied. The measurement starts at $t = 0$ and ends at $t_\mathrm{f} = t_\mathrm{qe} + 2\sigma_\mathrm{qe}$, when the field is quickly released[1] [69].

3.3 Simplified Analysis

Let us first consider a simple dispersive scenario at large qubit-resonator detuning, $|\Delta| \gg g\sqrt{\overline{n}+1}$, where $\overline{n}$ is the average number of photons in the resonator. In this case, the system is described by the usual dispersive Hamiltonian [39] $H_d = (\omega_0 - g^2/\Delta)\sigma_z/2 + (\omega_r - \sigma_z g^2/\Delta)a^\dagger a$, where σ_z is the Pauli matrix. After the short "catch" stage the system is in a product state $(\alpha|0\rangle + \beta|1\rangle)|\lambda_\mathrm{in}\rangle$, where α and β are the initial qubit state amplitudes and λ_in is the amplitude of the coherent resonator field, $\lambda_\mathrm{in} = -i\int B(t)\,dt$ (so $\overline{n} = |\lambda_\mathrm{in}|^2$). Then during the "disperse"

---

[1] Actually, for $\omega_\mathrm{q}(t)$ we additionally use small compensating ramps at the beginning and end of the procedure to provide the exact value ω_0 and to zero $\dot{\omega}_\mathrm{q}(t)$ at $t = 0$ and $t = t_\mathrm{f}$.

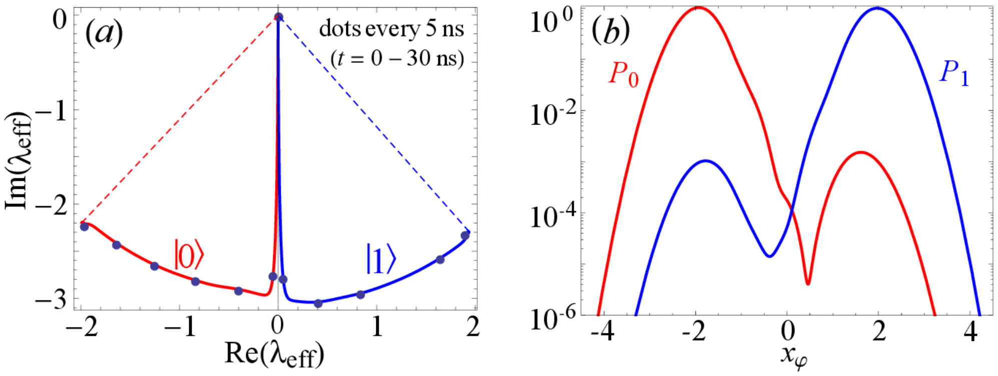

Figure 3.2: (a) Evolution in time of the effective field amplitude $\lambda_{\rm eff}$ on the phase plane for initial qubit states $|0\rangle$ and $|1\rangle$, computed numerically. The dots indicate time moments $t = 0$, 5, 10, 15, 20, 25, and 30 ns. (b) Corresponding probability distributions $P_0(x_\varphi)$ and $P_1(x_\varphi)$ for measurement (at $t = t_{\rm f}$) of the optimum quadrature x_φ. Side bumps of P_0 and P_1 are due to non-adiabaticity. We used $\Delta/2\pi = 50$ MHz, $|\lambda_{\rm in}|^2 = 9$, $\sigma_{\rm q} = 3$ ns, $t_{\rm q} = 3.25$ ns, $t_{\rm qe} = 30$ ns, and $t_{\rm f} = 32$ ns.

stage the qubit-resonator state becomes entangled, $\alpha|0\rangle|\lambda_0(t)\rangle + \beta|1\rangle|\lambda_1(t)\rangle$, with $\lambda_0 = \lambda_{\rm in}e^{-i\phi}$, $\lambda_1 = \lambda_{\rm in}e^{i\phi}$, and $\phi(t) = \int_0^t [g^2/\Delta(t')]dt'$.

The distinguishability of the two resonator states depends on their separation $|\delta\lambda| \equiv |\lambda_1 - \lambda_0| = 2|\lambda_{\rm in}|\sin|\phi|$ (see numerical results in Fig. 3.2). The released coherent states are measured via the homodyne detection using the optimal quadrature connecting λ_0 and λ_1, i.e., corresponding to the angle $\varphi = \arg(\lambda_1 - \lambda_0)$. We rescale the measurement results to the dimensionless field quadrature $\hat{x}_\varphi = (ae^{-i\varphi} + a^\dagger e^{i\varphi})/2$, which corresponds to the φ-angle axis in the phase space of Fig. 3.2(a). In resolving the two coherent states, we are essentially distinguishing two Gaussian probability distributions, $P_0(x_\varphi)$ and $P_1(x_\varphi)$, centered at $\pm|\delta\lambda|\sigma_{\rm coh}$ with $\sigma_{\rm coh} = 1/2$ being the coherent-state width (standard deviation) for both distributions. Then the measurement error has a simple form

$$E = \frac{1}{2}\int_{-\infty}^{\infty} \min(P_0, P_1)\, dx_\varphi = \frac{1 - \mathrm{Erf}(|\delta\lambda|\sqrt{\eta/2})}{2}, \tag{3.4}$$

where $\eta = \eta_{\rm col}\eta_{\rm amp}$ is the detection efficiency [70], which includes the collection efficiency $\eta_{\rm col}$ and quantum efficiency of the amplifier $\eta_{\rm amp}$. Unless mentioned otherwise, we assume $\eta = 1$, which corresponds to a quantum-limited phase-sensitive amplifier (for a phase-preserving amplifier $\eta \leq 1/2$).

3.4 Full Analysis

In general the JC qubit-resonator interaction [Eq. (3.1)] is non-linear for $|\lambda_{\rm in}|^2 \gtrsim \overline{n}_{\rm crit} \equiv \Delta^2/4g^2$ [39] and the resonator states are not coherent. The measurement error E is still given by the first part of Eq. (3.4), while the probability distributions $P_{0,1}(x_\varphi)$ of the measurement result for the qubit starting in either state $|0\rangle$ or $|1\rangle$ can be calculated in the following way. Assuming an instantaneous release of the field, we are essentially measuring the operator $\hat{x}_\varphi$. Therefore the probability $P(x_\varphi)$ for the ideal detection ($\eta = 1$) can be calculated by converting the Fock-space density matrix ρ_{nm} describing the resonator field, into the x_φ-basis, thus obtaining $P(x_\varphi) = \sum_{nm} \psi_n(x_\varphi)\rho_{nm}(t)\psi_m^*(x_\varphi)e^{-i(n-m)\varphi}$, where $\psi_n(x)$ is the standard nth-level wave function of a harmonic oscillator. For a non-instantaneous release of the microwave field the calculation of $P(x_\varphi)$ is non-trivial; however, since the qubit is already essentially decoupled from the resonator, the above result for $P(x_\varphi)$ remains the same [71] for optimal time-weighting of the signal. In the case of a non-ideal detection ($\eta < 1$) we should take a convolution of the ideal $P(x_\varphi)$ with the Gaussian of width $\sqrt{\eta^{-1} - 1}\,\sigma_{\rm coh}$. Calculation of the optimum phase angle φ minimizing the error is non-trivial in the general case. For simplicity we still use the natural choice $\varphi = \arg(\lambda_{\rm eff,1} - \lambda_{\rm eff,0})$, where the effective amplitude of the resonator field [72] is defined by $\lambda_{\rm eff} = \sum_n \sqrt{n}\rho_{n,n-1}$. The field density matrix ρ_{nm} is calculated numerically using the Hamiltonian [Eq. (3.1)] and then tracing over the qubit.

Extensive numerical simulations allowed us to identify two main contributions to the measurement error E in our scheme. The first contribution is due to the insufficient separation of the final resonator states $|\lambda_{\rm eff,1}\rangle$ and $|\lambda_{\rm eff,0}\rangle$, as described above. However, there are two important differences from the simplified analysis: the JC nonlinearity may dramatically change $|\delta\lambda|$ and it also produces a self-developing squeezing of the resonator states in the quadrature x_φ, significantly decreasing the error compared with Eq. (3.4) (both effects are discussed in more detail later). The second contribution to the measurement error is due to the nonadiabaticity of the front ramp of the qubit frequency pulse $\omega_q(t)$, which leads to the population of "wrong" levels in the eigenbasis. This gives rise to the side peaks ("bumps") in the probability distributions $P_{0,1}(x_\varphi)$, as can be seen in Fig. 3.2(b) (notice their similarity to the experimental results [73, 74], though the mechanism is different). During the dispersion stage these bumps move in the "wrong" direction, halting the exponential decrease in the error, and thus causing the error to saturate. The nonadiabaticity at the rear ramp of $\omega_q(t)$ is not important because the moving bumps do not have enough time to develop. Therefore the rear ramp can be steep, while the front ramp should be sufficiently smooth [Fig. 1(a)] to minimize the error.

Now let us discuss the effect of nonlinearity (when $|\lambda_{\rm in}|^2 > \overline{n}_{\rm crit}$) on the evolution of $\lambda_{\rm eff,0}$ and $\lambda_{\rm eff,1}$ during the disperse stage. Since the RF drive is turned off, the interaction described by the Hamiltonian [Eq. (3.1)] occurs only between the pairs of states $|0,n\rangle$ and $|1,n-1\rangle$ of the JC ladder. Therefore, if the front ramp of the qubit frequency pulse is adiabatic, the pairs of the JC *eigenstates* evolve only by accumulating their respective phases while maintaining their populations. Then for the qubit initial state $|0\rangle$, the qubit-resonator wavefunction evolves approximately as $|\psi_0(t)\rangle \simeq e^{-|\lambda_{\rm in}|^2/2}\sum_n(\lambda_{\rm in}^n/\sqrt{n!})e^{-i\phi_{0,n}(t)}|\overline{0,n}\rangle$, where the overbar denotes the (dressed) eigenstate and $\phi_{0,n}(t) = \int_{t_{\rm D}}^t dt'[\sqrt{\Delta(t')^2+4g^2n} - \Delta(t')]/2$ is the accumulated phase, with $t_{\rm D} = t_{\rm B} + \tau_{\rm B}/2$ being the center of the $B(t)$-pulse, which is crudely the start of the dispersion. Similarly, if the qubit starts in state $|1\rangle$ (following the ideology of Ref. [75], we then use $\overline{|10\rangle}$ as the initial state), the state evolves as $|\psi_1(t)\rangle \simeq e^{-|\lambda_{\rm in}|^2/2}\sum_n(\lambda_{\rm in}^n/\sqrt{n!})e^{i\phi_{1,n}(t)}|\overline{1,n}\rangle$, where $\phi_{1,n}(t) = \int_{t_{\rm D}}^t dt'[\sqrt{\Delta(t')^2+4g^2(n+1)} - \Delta(t')]/2$. Using the above definition of $\lambda_{\rm eff}$ and assuming $|\lambda_{\rm in}|^2 \gg 1$ we derive an approximate formula

$$\lambda_{\rm eff,0} = \lambda_{\rm in}\exp\left[-i\int_{t_{\rm D}}^t \frac{g^2}{\sqrt{\Delta(t')^2+4g^2|\lambda_{\rm in}|^2}}\,dt'\right]. \tag{3.5}$$

The corresponding expression for $\lambda_{\rm eff,1}$ can be obtained by replacing $-i$ with i and $|\lambda_{\rm in}|^2$ with $|\lambda_{\rm in}|^2+1$. These formulas agree well with our numerical results.

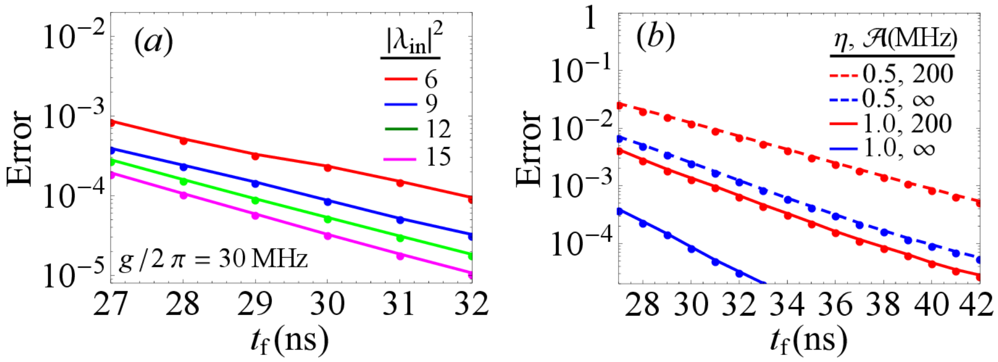

Figure 3.3: Optimized measurement error E vs measurement time $t_{\rm f}$ (optimization is over Δ, $\sigma_{\rm q}$, and $t_{\rm q}$). (a) For two-level qubit and for mean photon number $|\lambda_{\rm in}|^2 = 6, 9, 12$, and 15. (b) For $|\lambda_{\rm in}|^2 = 9$ and $\eta = 1$ or $1/2$ (e.g. for a phase-preserving amplifier), taking into account the qubit level $|2\rangle$ (with anharmonicity $\mathcal{A}/2\pi = 200$ MHz) or assuming a two-level qubit ($\mathcal{A} = \infty$).

Equation (3.5) shows that a decrease in detuning leads to an increase in the rotation speed of $\lambda_{\rm eff}$. However, in the strongly nonlinear regime $|\lambda_{\rm in}|^2 \gg \overline{n}_{\rm crit}$, the angular speed saturates at $d(\arg(\lambda_{{\rm eff},0/1}))/dt = \mp g/2|\lambda_{\rm in}|$. Thus, the rate at which the $\lambda_{{\rm eff},1}$ and $\lambda_{{\rm eff},0}$ separate is limited by

$$d|\delta\lambda|/dt \le |g|, \tag{3.6}$$

which does not depend on $|\lambda_{\rm in}|$. This means that the measurement time should not improve much with increasing the mean number of photons $|\lambda_{\rm in}|^2$ in the resonator, as long as it is sufficient for distinguishing the states with a desired fidelity (crudely, $|\lambda_{\rm in}|^2 \gtrsim 7/\eta$ for $E \lesssim 10^{-4}$).

Figure 3.3(a) shows the results of a three-parameter optimization of the measurement error E for several values of the average number of photons in the resonator, $|\lambda_{\rm in}|^2$ (assuming $\eta = 1$). The optimization parameters are the qubit-resonator detuning Δ, the width σ_q, and the center t_q of the qubit front ramp. We see that for 9 photons in the resonator the error of 10^{-4} can be achieved with 30 ns measurement duration, excluding time to release and measure the field. The optimum parameters in this case are: $\Delta/2\pi = 60$ MHz, $\sigma_q = 4.20$ ns, and $t_q = 3.25$ ns (this is a strongly nonlinear regime: $|\lambda_{\rm in}|^2/\overline{n}_{\rm crit} = 9$). As expected from the above discussion, increasing the mean photon number to 12 and 15 shortens the measurement time only slightly (by 1 ns and 2 ns, keeping the same error). The dashed blue curve in Fig. 3.3(b) shows the optimized error for $|\lambda_{\rm in}|^2 = 9$ and imperfect quantum efficiency $\eta = 1/2$. As we see, the measurement time for the error level of 10^{-4} increases to 40 ns, while the error of 10^{-3} is achieved at $t_{\rm f} = 32$ ns.

So far, we considered the two-level model for the qubit. However, real superconducting qubits are only slightly anharmonic oscillators, so the effect of the next excited level $|2\rangle$ is often important. It is straightforward to include the level $|2\rangle$ into the Hamiltonian [Eq. (3.1)] by replacing its first term with $\omega_{\rm q}|1\rangle\langle 1| + (2\omega_{\rm q} - \mathcal{A})|2\rangle\langle 2|$, where $\mathcal{A}$ is the anharmonicity. The dispersion can then be understood as due to repulsion of three eigenstates: $\overline{|0, n\rangle}$, $\overline{|1, n-1\rangle}$, and $\overline{|2, n-2\rangle}$. As the result, $\lambda_{\rm eff,0}$ rotates on the phase plane faster than in the two-level approximation, while $\lambda_{\rm eff,1}$ rotates slower (sometimes even in the opposite direction). In Fig. 3.3(b), we present the optimized error for $\mathcal{A}/2\pi = 200$ MHz (a typical value for transmon and phase qubits), $|\lambda_{\rm in}|^2 = 9$ and $\eta = 1$ (solid-red curve) or $\eta = 1/2$ (dashed-red curve). An error of 10^{-3} can be achieved with 31 ns ($\eta = 1$) and 39 ns ($\eta = 1/2$) measurement durations.

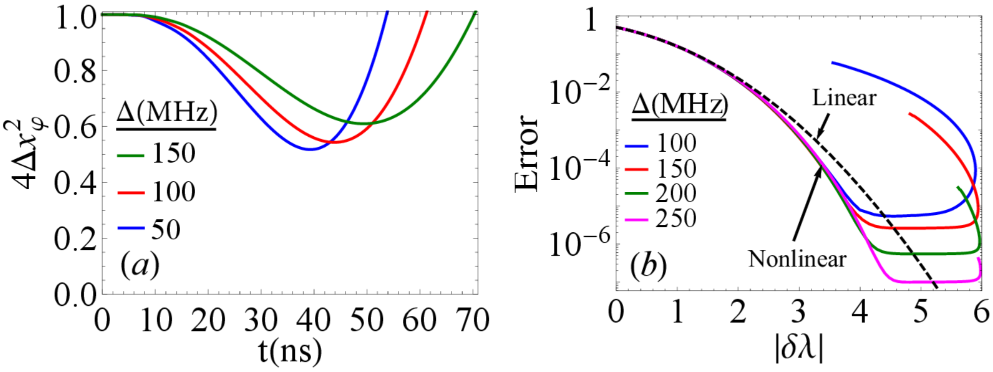

Figure 3.4: (a) Evolution of the quadrature squeezing (the qubit is initially in state $|0\rangle$). (b) Measurement error vs $|\delta\lambda|$ calculated numerically in the nonlinear regime (solid lines) and using the linear approximation (3.4) (dashed line); here the evolution stops at 98 ns. $|\lambda_{\rm in}|^2 = 9$, $\sigma_q = 4$ns, $t_q = 3.25$ ns.

We next discuss the self-generated quadrature squeezing of the microwave field induced by the JC nonlinearity. To quantify the degree of squeezing, we calculate the variance $\Delta x_\varphi^2 = \langle x_\varphi^2\rangle - \langle x_\varphi\rangle^2 = 1/4 + \langle a^\dagger a\rangle/2 - |\langle a\rangle|^2/2 + {\rm Re}[(\langle a^2\rangle - \langle a\rangle^2)e^{-2i\varphi}]/2$. For a coherent field $\Delta x_\varphi^2 = 1/4$, thus the state is squeezed [72] when $4\Delta x_\varphi^2 < 1$. Figure 3.4(a) shows evolution of $4\Delta x_\varphi^2$ when the initial qubit state is $|0\rangle$, for $\eta = 1$ and assuming a two-level qubit (a similar result is obtained for qubit initially in state $|1\rangle$). Notice that at first the field stays coherent, which is due to the linearity of the qubit-resonator interaction at large detuning. Later on, however, the interaction becomes nonlinear due to decreased detuning and leads to quadrature squeezing reaching the level of ~50% for $\Delta/2\pi \lesssim 100$ MHz (see Supplemental Materials of Ref. [76] for the Wigner function evolution). Figure 3.4(b) shows the measurement error as a function of $|\delta\lambda|$ in the nonlinear regime calculated numerically (solid curves) and in the linear regime based on Eq. (3.4) (dashed curve). As expected, with the squeezing developing, the error becomes significantly smaller than the linear (analytical) prediction, for instance, up to a factor of 30 for $\Delta/2\pi = 250$ MHz. Note also that the error shown in Fig. 3.4(b) saturates in spite of increasing separation $|\delta\lambda|$. This is because of the non-adiabatic error discussed above.

We do not focus on the quantum non-demolition (QND) [77] property of the readout, because in the proposed implementation of the surface code [78] the measured qubits are reset, so the QNDness is not important. For the results presented in Fig. 3.3 the non-QNDness (probability that the initial states $|00\rangle$ and $\overline{|10\rangle}$ are changed after the procedure) is crudely about 5%, which is mainly due to non-adiabaticity of the rear ramp. It is possible to strongly decrease the non-QNDness by using smoother rear ramp, but it cannot be reduced below few times $(g/\Delta_0)^2$, essentially because of the Purcell effect during the release stage. Furthermore, we do not consider the measurement-induced dephasing of the qubit, since our readout is not intended for a continuous qubit monitoring or a quantum feedback. We neglect the qubit relaxation and excitation due to “dressed dephasing” [79], because its rate is smaller than the intrinsic pure dephasing, which for transmons is usually smaller than intrinsic relaxation.

3.5 Summary

We have analyzed a fast high-fidelity readout scheme for superconducting qubits in a cQED architecture using the controlled catch, dispersion, and release of microwave photons. This readout scheme uses a tunable coupler to decouple the resonator from the transmission line during the dispersion stage of the measurement, thus avoiding the Purcell effect. Our approach may also be used as a new tool to beat the standard quantum limit via self-developing field squeezing, directly measurable using the state-of-the-art parametric amplifiers.

Chapter 4

Deviations from Dressed-Coherent State Model

In the previous chapter, we considered a specialized scheme for measurement of a qubit-resonator system that avoids the Purcell effect to achieve fast and high-fidelity readout. This chapter will further explore the same system; specifically, we consider the measurement of a superconducting transmon qubit via a coupled microwave resonator.

For ideally dispersive coupling, ringing up the resonator produces coherent states with frequencies matched to transmon energy states. Realistic coupling is not ideally dispersive, however, so transmon-resonator energy levels hybridize into joint eigenstate ladders of the Jaynes-Cummings type. Previous work has shown that ringing up the resonator approximately respects this ladder structure to produce a coherent state in the eigenbasis (a dressed coherent state).

One of the simplifications of the model used in the work on Catch-Disperse-Release, however, was the assumption in the Jaynes-Cummings model of a two-level artificial atom. Although this approximation is commonly used in the theory for transmon-based systems, the latter has multiple levels which can be excited. The effect of the $|2\rangle$ level was estimated, but this basic investigation was meant more to approximate the effect of higher levels on the discussed measurement scheme than to examine the general effects of an extended Jaynes-Cummings ladder. Here, we more accurately model the transmon qubit with many levels (typically, seven).

In this chapter, we numerically investigate the validity of the coherent state approximation in this extended system, and find one of the primary deviations to be that resonator ring-up leaks small stray populations into eigenstate ladders corresponding to different transmon states. We then quantify these deviations and find their analytical forms.

We organize this chapter as follows. In Sec. 4.1 we begin with an introduction to the dressed coherent state and outlining the problem we will solve in this chapter. In Sec. 4.2 we describe the resonator-transmon system and how the numerical simulations are performed. In Sec. 4.3 we discuss the dressed coherent state model and focus on analyzing the inaccuracy of this model relative to numerical simulation. We also quantify the stray population leakage into incorrect eigenstate ladders as a major deviation from the dressed coherent state model. We conclude in Sec. 4.4.

4.1 Introduction

Qubit technology using superconducting circuit quantum electrodynamics (QED) [39, 80] has rapidly developed over the past decade to become a leading contender for realizing a scalable quantum computer. Most recent qubit designs favor variations of the transmon [56, 81, 64, 82, 83, 84, 85] due to its charge-noise insensitivity, which permits long coherence times while also enabling high-fidelity quantum gates [86, 87, 88] and high-fidelity dispersive qubit readout [89, 74, 60] via coupled microwave resonators. Transmon-based circuit operation fidelities are now near the threshold for quantum error correction protocols, some versions of which have been realized [90, 91, 92, 93].

The quantized energy states of a transmon are measured in circuit QED by coupling them to a detuned microwave resonator. For low numbers of photons populating the readout resonator, the coupling is well-studied [39, 56, 94] and approximates an idealized dispersive quantum non-demolition (QND) measurement [77]. Each transmon energy level dispersively shifts the frequency of the coupled resonator by a distinct amount, allowing the transmon state to be determined by measurement of the leaked and amplified resonator field. However, nondispersive effects become important when the number of resonator photons becomes comparable to a characteristic ("critical") number set by the detuning and coupling strength [39, 95, 66]; present-day experiments often operate in this nondispersive (or nonlinear dispersive) regime [60, 96, 97, 98].

We analyze and model the nondispersive effects that occur during the ring-up of a readout resonator coupled to a transmon. These effects arise from the hybridization of the resonator and transmon states into joint resonator-transmon eigenstates. While ringing up the resonator from its ground state, the joint state remains largely confined to a single Jaynes-Cummings eigenstate ladder that corresponds to the initial transmon state. As pointed out in Refs. [76, 59, 99], this joint state can be approximated by a coherent state in the eigenbasis (recently named a dressed coherent state [99]). Here we refine this initial approximation and provide a more accurate model for the hybridized resonator-transmon state.

We numerically simulate the ring-up process for a resonator coupled to a transmon, then use this simulation to develop and verify our analytical model. We consider one of the dominant deviations from a dressed coherent state by showing that the ring-up process allows a small population to leak from an initial transmon state into neighboring eigenstate ladders. We find simple expressions that quantify this stray population ($\lesssim 10^{-4}$ for typical experimental parameters).

To simplify our analysis and isolate the hybridization effects of interest, we restrict our attention to a transmon (modeled as a seven-level nonlinear oscillator) coupled to a coherently pumped but non-leaking resonator (using the rotating wave approximation). The simplification of no resonator leakage may seem artificial, but it is still a reasonable approximation during the resonator ring-up and it is also relevant for at least two known protocols. First, the catch-disperse-release protocol [76] encodes qubit information into resonator states with minimal initial leakage, then rapidly releases the resonator field to a transmission line. Second, a recently proposed readout protocol [100] similarly encodes qubit information into bright and dark resonator states with minimal leakage, then rapidly distinguishes them destructively using Josephson photomultipliers [101].

4.2 Model

Following the circuit QED paradigm of measurement [39], we consider a transmon coupled to a detuned readout resonator. We do not simplify the transmon to a two-level qubit, but instead include the lowest seven energy levels confined by the cosine potential of the transmon. Though the transmon eigenstates may be written explicitly as Mathieu functions [56, 102], we have checked that a perturbative treatment of the transmon as an approximate oscillator with quartic arharmonicity [56] is sufficiently accurate for our purposes. We assume a transmon-resonator coupling of Jaynes-Cummings type [103], using the rotating wave approximation (RWA) for simplicity. We do not pump our system to very high photon numbers in order to avoid some unwanted effects [98].

4.2.1 Pumped resonator-transmon Hamiltonian

In our model the resonator Hamiltonian is

$$H_{\mathrm{r}} = \omega_{\mathrm{r}}\, a^{\dagger} a = \sum_{n,k} n\, \omega_{\mathrm{r}}\, |n,k\rangle \langle n,k| \,, \tag{4.1}$$

with $\hbar = 1$, bare resonator frequency ω_{r}, lowering (raising) operator a ($a^{\dagger}$) for the resonator mode satisfying $[a, a^{\dagger}] = 1$, and resonator index $n = 0, 1, \ldots$ for successive energy levels. For completeness we included the transmon index $k = 0, 1, \ldots, 6$ for the 7 lowest levels to emphasize the matrix representation in terms of the joint product states $|n, k\rangle \equiv |n\rangle_{\mathrm{r}} \otimes |k\rangle_{\mathrm{q}}$ for the bare energy states.

Similarly, the transmon Hamiltonian has the form

$$H_{\mathrm{q}} = \sum_{n,k} E_k \; |n, k\rangle \, \langle n, k| \, , \tag{4.2}$$

$$E_k = E_0 + \omega_{\mathrm{q}} k - \eta \, \frac{k(k-1)}{2}. \tag{4.3}$$

The dominant effect of the nonlinearity of the cosine potential for the transmon is the quartic anharmonicity $\eta \equiv \omega_{10} - \omega_{21} > 0$ of the upper level frequency spacings relative to the qubit frequency $\omega_{\mathrm{q}} \equiv \omega_{10}$, where each frequency $\omega_{k\ell} \equiv E_k - E_\ell$ denotes an energy difference. At this level of approximation, the transmon has the structure of a Duffing oscillator with a linearly accumulating anharmonicity $\omega_{(k+1)k} = \omega_{\mathrm{q}} - k\,\eta$. [This approximation is sometimes extended to an infinite number of levels, $H_{\mathrm{q}} = E_0 + \omega_{\mathrm{q}}\, b^\dagger b - (\eta/2)\, b^\dagger b (b^\dagger b - 1)$ [104], with an effective oscillator lowering (raising) operator b ($b^\dagger$) satisfying $[b, b^\dagger] = 1$, but we explicitly keep only the 7 lowest levels here.]

The excitation-preserving interaction (within RWA) is

$$H_{\mathrm{I}} = \sum_{n,k} g \, \sqrt{n(k+1)} \; |n-1, k+1\rangle \, \langle n, k| + \text{H.c.}, \tag{4.4}$$

where g is the coupling strength between levels $|0, 1\rangle$ and $|1, 0\rangle$. As in Ref. [56], we neglect the effects of the anharmonicity η in the coupling for simplicity. [Extending this coupling to an infinite number of transmon levels yields $H_I = g\,(ab^\dagger + a^\dagger b)$.]

Finally, the Hamiltonian for coherently pumping the resonator with a classical field $\varepsilon(t)\, e^{-i\omega_\mathrm{d} t}$ is (within RWA)

$$\begin{aligned} H_\mathrm{d} &= \varepsilon(t)\, e^{-i\omega_\mathrm{d} t}\, a^\dagger + \varepsilon^*(t)\, e^{i\omega_\mathrm{d} t}\, a \\ &= \varepsilon(t)\, e^{-i\omega_\mathrm{d} t} \sum_{n,k} \sqrt{n+1}\ |n+1,k\rangle\, \langle n,k| + \text{H.c.}, \end{aligned} \tag{4.5}$$

where $\varepsilon(t)$ is a complex envelope for the drive. Note that, in the previous chapter we use the notation $B(t)$ for $\epsilon(t)$ and ω for ω_d [see Eq. (3.1)].

Combining Eqs. (4.1)–(4.5) into the total Hamiltonian $H = H_\mathrm{r} + H_\mathrm{q} + H_\mathrm{I} + H_\mathrm{d}$, and rewriting it in the rotating frame of the drive frequency ω_d yields

$$\begin{aligned} H_\mathrm{rot} = \sum_{n,k} \Big\{ & [n\,(\omega_\mathrm{r} - \omega_\mathrm{d}) + (E_k - k\,\omega_\mathrm{d})]\, |n,k\rangle\, \langle n,k| \\ & + g\,\sqrt{n(k+1)}\ |n-1,k+1\rangle\, \langle n,k| + \text{H.c.} \\ & + \varepsilon(t)\, \sqrt{n+1}\ |n+1,k\rangle\, \langle n,k| + \text{H.c.} \Big\}. \end{aligned} \tag{4.6}$$

This simplified Hamiltonian will be sufficient in what follows to observe the dominant non-dispersive effects that affect the resonator ring-up. Note that we use the rotating frame in numerical simulations, but physics related to Jaynes-Cummings ladders of states is easier to understand in the lab frame, so we will often imply the lab frame for clarity in the discussions below.

4.2.2 Numerical simulation and diagonalization

For numerical simulation, the Hamiltonian in Eq. (4.6) is represented by a $7N \times 7N$ matrix using the bare energy basis $|n, k\rangle$, where $N = 200$–800 is the maximum number of simulated levels for the resonator. We choose experimentally relevant resonator and transmon parameters, which in most simulations are $\omega_{\mathrm{r}}/2\pi = 6\,\mathrm{GHz}$, $\omega_{\mathrm{q}}/2\pi = 5\,\mathrm{GHz}$, $\eta/2\pi = 200\,\mathrm{MHz}$, and $g/2\pi = 100\,\mathrm{MHz}$. For the drive, we change the frequency ω_{d} to be resonant with specific eigenstate transition frequencies of interest (detailed later) and use drive amplitudes typically in the range $\varepsilon/2\pi = 10$–60 MHz.

The hybridization of the joint eigenstates is significant when the number of photons n in the resonator is comparable to or larger than the so-called critical photon number [39, 95, 66],

$$n_c = \frac{(\omega_{\mathrm{r}} - \omega_{\mathrm{q}})^2}{4g^2}. \tag{4.7}$$

For the above parameters $n_c = 25$. This defines the scale at which we expect significant deviations from the ideal dispersive model.

We use the following numerical procedure for identifying the joint hybridized eigenstates $\overline{|n, k\rangle}$ of Eq. (4.6) without a drive—we will distinguish dressed (eigen) states (and operators) from bare states by an overline throughout. After setting $\varepsilon = 0$ to eliminate the drive, the matrix representation of Eq. (4.6) is numerically diagonalized to obtain an initially unsorted list of matched eigenenergy/eigenstate pairs $\{\overline{E}_{n,k}, \overline{|n,k\rangle}\}$ for the qubit-resonator system. The one-to-one correspondence between these pairs and the bare energy/state pairs $\{E_{n,k}, |n,k\rangle\}$ may be found by examining the structure of the RWA interaction Hamiltonian in Eq. (4.4): Since excitation number is preserved, there exist closed subspaces $\{|n,k\rangle : (n+k) = n_\Sigma\}$ with constant excitation number $n_\Sigma = 0, 1, \ldots$, which we name *RWA strips* [98]. Crucially, since energy levels repel during interaction and avoid crossing, the order of the eigenenergies within a strip is the same as for bare energies. Thus, for each strip with n_Σ excitations we first identify the eigenstates $\overline{|n,k\rangle}$ that lie within the span of that strip; next, we order the eigenenergies $\overline{E}_{n,k}$ to match the bare energies $E_{n,k}$, which uniquely identifies each hybridized eigenenergy/eigenstate pair. We then set the overall sign of each eigenstate such that it does not flip with changing n. After performing this identification, we construct a basis-change matrix

$$U \equiv \sum_{n,k} \overline{|n,k\rangle} \langle n,k| \tag{4.8}$$

to easily switch between representations numerically. Note that without proper identification (sorting) of the eigenstates, the numerical analysis at large photon numbers is practically impossible.

The eigenstates $\overline{|n,k\rangle}$ form the Jaynes-Cummings ladders of effective resonator levels that correspond to a fixed nominal qubit level k. For brevity we will call them *eigenladders* of dressed resonator Fock states. Each eigenladder behaves like a nonlinear resonator, with an n-dependent frequency

$$\omega_{\mathrm{r}}^{(k)}(n) = \overline{E}_{n+1,k} - \overline{E}_{n,k}. \tag{4.9}$$

Note that in this formula both sides are numerically calculated in the rotating frame; however, the equation in the lab frame is the same. Conversion to the lab frame involves adding the drive frequency: $\omega_{\mathrm{d}}+\omega_{\mathrm{r}}^{(k)}(n)$ for the resonator frequency and $(n+k)\,\omega_{\mathrm{d}} + \overline{E}_{n,k}$ for energy.

At large photon numbers, $n \gtrsim n_c$, each $\overline{|n,k\rangle}$ spans a significant fraction of all bare transmon levels. Nevertheless, as we will see, ringing up the resonator from its ground state with an initial transmon level k will primarily excite the states within the eigenladder corresponding to k. This behavior closely mimics that of the ideal dispersive case, where a pump excites the bare resonator states $|n\rangle_{\mathrm{r}}$ while keeping the transmon state $|k\rangle_{\mathrm{q}}$ unperturbed. However, we will also show that there are small but important dynamical differences between our RWA Jaynes-Cummings model and ideal dispersive coupling in the eigenbasis.

4.3 Dressed coherent state model

We now define an ideal coherent state in the eigenbasis [76, 59, 99] (a dressed coherent state) corresponding to a nominal transmon state k as

$$|\alpha\rangle_k = e^{-|\alpha|^2/2} \sum_n \frac{\alpha^n}{\sqrt{n!}} \overline{|n,k\rangle}, \tag{4.10}$$

so that the only difference from the standard coherent state of the resonator is that we use eigenstates instead of the bare states. Perhaps surprisingly given the eigenstate hybridization, such a dressed coherent state is practically unentangled even for $|\alpha|^2 \gg n_c$, in contrast to what one might initially guess [99]—see the appendix of [105].

A dressed coherent state is not an eigenstate of the bare lowering operator a of the resonator. Instead, it is an eigenstate of the *dressed* lowering operator [79, 59]

$$\overline{a} \equiv UaU^\dagger = \sum_{n,k} \sqrt{n+1}\ \overline{|n,k\rangle}\overline{\langle n+1,k|} \tag{4.11}$$

that removes a collective excitation within the same eigenladder. The parameter α is the expectation value of the dressed lowering operator, $\alpha = {}_k\langle\alpha|\,\overline{a}\,|\alpha\rangle_k$, which will be useful in what follows.

Note that for a dressed coherent state $|\alpha\rangle_k$, $|\alpha|^2$ is not exactly equal to the average number $\bar{n}$ of photons in the resonator. (Instead, $|\alpha|^2 = {}_k\langle\alpha|\,\overline{a}^\dagger\overline{a}\,|\alpha\rangle_k$ is the average dressed excitation number within eigenladder k.) However, the difference is very small and will be mostly neglected below, so that we will use $\bar{n} = |\alpha|^2$. In the cases when the difference may be important, we will specify the meaning of $\bar{n}$ explicitly.

4.3.1 Model inaccuracy contributions

During resonator ring-up, we expect the joint qubit-resonator state to approximate such a dressed coherent state, rather than a bare coherent state as is usually assumed with ideal dispersive coupling. As such, we quantify the fidelity of a numerically simulated state $|\psi\rangle$ compared to a dressed coherent state $|\alpha\rangle_k$ as the overlap

$$F = |\langle\psi|\,\alpha\rangle_k|^2, \tag{4.12}$$

where the parameter α is chosen to maximize the fidelity. In practice, we find that an initial guess of $\alpha = \langle\psi|\,\overline{a}\,|\psi\rangle$ is very close to the optimal α, producing nearly indistinguishable fidelity.

Note that we can expand a numerically calculated state $|\psi\rangle = \sum_{n,\ell} c_{n,\ell}\,\overline{|n,\ell\rangle}$ as

$$|\psi\rangle = \sqrt{1 - P_{\text{stray}}}\;|\psi\rangle_k + \sqrt{P_{\text{stray}}}\;|\psi\rangle_\perp\,, \tag{4.13}$$

splitting it into a part $|\psi\rangle_k \propto \sum_n c_{n,k}\,\overline{|n,k\rangle}$ within the “correct” eigenladder k, and a part $|\psi\rangle_\perp \propto \sum_{n,\ell\neq k} c_{n,\ell}\,\overline{|n,\ell\rangle}$ orthogonal to that eigenladder, where $P_{\text{stray}} = \sum_{n,\ell\neq k} |c_{n,\ell}|^2$ is the stray population that leaked out of the eigenladder k, and both $|\psi\rangle_k$ and $|\psi\rangle_\perp$ are normalized. As such, if we define the overlap fidelity within the correct eigenladder $F_{\text{c}} = |_k\langle\alpha|\,\psi\rangle_k|^2$, then we can write the total fidelity as $F = (1 - P_{\text{stray}})\,F_{\text{c}}$, and thus decompose the infidelity

$$1 - F = P_{\text{stray}} + (1 - P_{\text{stray}})(1 - F_{\text{c}}) \tag{4.14}$$

into two distinct sources: (i) the stray population P_{stray} outside the correct eigen-

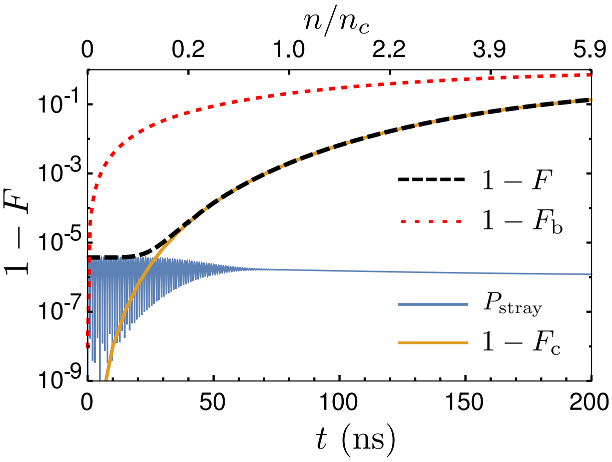

Figure 4.1: Infidelity of coherent-state approximations during resonator ring-up. The infidelity $1-F_\mathrm{b}$ of a bare coherent state (dotted red line) is compared with the infidelity $1-F$ of a dressed coherent state (dashed black line). The latter displays two distinct effects: at short time (and small photon number $\bar{n}$) the dominant effect is the leakage of a stray population P_stray (blue line) out of the correct eigenladder; however, at longer time (and larger $\bar{n}$) the infidelity $1-F_\mathrm{c}$ of the renormalized state within the correct eigenladder (solid orange line) significantly increases during evolution. Here the system, with parameters $\omega_\mathrm{r}/2\pi = 6\,\mathrm{GHz}$, $\omega_\mathrm{q}/2\pi = 5\,\mathrm{GHz}$, $\eta/2\pi = 200\mathrm{MHz}$, $g/2\pi = 100\,\mathrm{MHz}$, is resonantly pumped from its ground state $|0,0\rangle$ with a constant drive envelope $\varepsilon/2\pi = 10\,\mathrm{MHz}$.

ladder, and (ii) the infidelity $1-F_\mathrm{c}$ compared with a coherent state within the correct eigenladder.

To test the infidelity of the dressed coherent state model, we numerically simulate the resonator ring-up with a (sudden) constant drive amplitude $\varepsilon/2\pi = 10$ MHz, and then calculate the infidelity according to Eq. (4.14) as a function of time, yielding the results presented in Fig. 4.1. First, we confirm that the infidelity $1-F$ for a dressed coherent state (black dashed line) is typically orders of magnitude better than the infidelity $1-F_\mathrm{b}$ for a bare coherent state (red dotted line); as expected, $1-F_\mathrm{b}$ becomes very significant at $n \gtrsim n_c$. Second, we can clearly separate the effects of the stray population leakage P_stray (solid blue line) from the infidelity $1 - F_{\mathrm{c}}$ of the renormalized state within the correct eigenladder (solid orange line). At short times, the dominant effect is a small ($\sim 10^{-5}$) stray population leakage that rapidly oscillates and then stays approximately constant. (For clarity we do not show oscillations for the black dashed line, showing only the maxima.) However, at longer times the contribution $1 - F_{\mathrm{c}}$ becomes the dominant source of infidelity (eventually reaching $\sim 10^{-1}$). Below, we quantify these two sources of infidelity in more detail.

4.3.2 Infidelity from stray population

We now focus on the cause of the stray population outside the correct eigenladder. Figure 4.2 shows numerical results for different choices of initial state and drive amplitude, produced in a manner similar to Fig. 4.1, but focusing on shorter times and lower photon numbers, where the stray population is the dominant source of infidelity. Initially, the stray population rapidly oscillates from zero around a steady-state value, then the oscillations damp, after which the stray population continues to slowly decay on a longer time scale. We now provide a phenomenological model that describes this behavior.

A dressed coherent state would naturally be produced by a dressed displacement Hamiltonian of the form $\varepsilon^{*}\overline{a} + \varepsilon\overline{a}^{\dagger}$, as opposed to the bare displacement Hamiltonian $\varepsilon^{*}a + \varepsilon a^{\dagger}$ of the drive that appears in Eq. (4.6). This mismatch between bare and dressed states in the drive is the source of the stray population that leaks out of the correct eigenladder during ring-up. To show this mismatch in a simple way, we first focus on the ring-up from an initial ground state $|0,0\rangle = \overline{|0,0\rangle}$.

In this case the dominant leakage occurs to the eigenladder $\overline{|n,1\rangle}$, with negligible second-order leakage to the other eigenladders. [As discussed later, the following derivation may be readily generalized to other initial states, such as $\overline{|0,1\rangle}$ in Figs. 4.2(c)-(d).]

Focusing only on the coupling between eigenladders $\overline{|n,0\rangle}$ and $\overline{|n,1\rangle}$, for $n \ll n_c$ we can write [79, 59]

$$a \approx \bar{a} - \frac{g}{\Delta}\,\overline{\sigma}_{-}, \;\; \Delta = \omega_{\rm r} - \omega_{\rm q}, \;\; \overline{\sigma}_{-} = \sum_{n} \overline{|n,0\rangle}\overline{\langle n,1|}, \tag{4.15}$$

where $\overline{\sigma}_{-}$ is the qubit lowering operator in the eigenbasis. It is natural to guess that at $n \gtrsim n_c$ the resonator-qubit detuning Δ should change because of the ac Stark shift, and therefore Eq. (4.15) can be replaced with approximation

$$a \approx \bar{a} - \sum_{n} \frac{g}{\Delta_n}\,\overline{|n,0\rangle}\overline{\langle n,1|}, \;\; \Delta_n = \overline{E}_{n+1,0} - \overline{E}_{n,1}, \tag{4.16}$$

where Δ_n is the qubit-resonator detuning with account of the ac Stark shift, $\omega_{\rm q}(n) = \overline{E}_{n,1} - \overline{E}_{n,0}$ (see Appendix of [61]). We did not prove Eq. (4.16) analytically, but we checked numerically that this approximation works well, at least for our range of parameters. Additionally approximating $\Delta_n \approx \Delta_{\bar{n}}$ for a dressed coherent state with $\bar{n} = |\alpha|^2$, from Eq. (4.16) we obtain

$$a \approx \bar{a} - \frac{g}{\Delta_{\bar{n}}}\,\overline{\sigma}_{-}. \tag{4.17}$$

(For non-integer $\bar{n}$, we can use the nearest integer or the more precise method of averaging Δ_n over the state.) Note that for a constant resonant drive, the average number of photons increases as $\bar{n}(t) \approx |\varepsilon t|^2$, before the changing resonator frequency (4.9) starts affecting the resonance.

Thus, the drive term in the Hamiltonian can be approximately expanded in the eigenbasis as

$$\varepsilon^* a + \varepsilon a^\dagger \approx (\varepsilon^* \bar{a} + \varepsilon \bar{a}^\dagger) - \frac{g}{\Delta_{\bar{n}}} \left(\varepsilon^* \overline{\sigma}_- + \varepsilon \overline{\sigma}_+ \right), \tag{4.18}$$

where $\overline{\sigma}_+ = (\overline{\sigma}_-)^\dagger$. The first term of this effective drive produces dressed coherent states, while the second term couples the lowest two eigenladders to cause leakage.

The coupling essentially "copies" the dressed coherent state from the correct eigenladder $\overline{|n, 0\rangle}$ to the neighboring eigenladder. The resulting copy has a relatively small magnitude because $g/\Delta_{\bar{n}} \ll 1$ and also because the two eigenladders have a significant frequency shift due to differing energies. Thus, we assume approximately the same dressed coherent state $\alpha(t)$ in both eigenladders and use the joint state of the form $|\psi\rangle \approx |\alpha(t)\rangle_0 + c(t)\ |\alpha(t)\rangle_1$, where the small amplitude $c(t)$ quantifies the leakage to the $\overline{|n, 1\rangle}$ eigenladder, so that the stray population is $P_{\text{stray}} = |c|^2 \ll 1$. In this case we can approximately write $c = \langle\psi|\, \overline{\sigma}_- \,|\psi\rangle$, and thus find the evolution $\dot{c} = \langle\psi|\ i\, [H_{\text{rot}},\, \overline{\sigma}_-]\ |\psi\rangle$, which simplifies to

$$\dot{c} \approx i\, \frac{\varepsilon g}{\Delta_{\bar{n}}} + i\Omega_{\bar{n}}\, c, \tag{4.19}$$

where $\Omega_{\bar{n}} = \Delta_{\bar{n}} + \omega_{\text{d}} - \omega_{\text{r}}$ is the oscillation frequency (note that $\Omega_{\bar{n}} = \Delta_{\bar{n}}$ for a resonant drive). The steady state for this evolution (assuming a slowly changing

$\bar{n}$), $\dot{c}_{\text{s.s.}} = 0$, corresponds to the steady-state leakage population

$$P_{\text{s.s.}} = |c_{\text{s.s.}}|^2 = \left|\frac{\varepsilon g}{\Omega_{\bar{n}}\Delta_{\bar{n}}}\right|^2 . \tag{4.20}$$

For a drive that is suddenly turned on, as in Fig. 4.2(a), the stray population will oscillate to reach a maximum

$$P_{\max} = |2c_{\text{s.s.}}(0)|^2 = 4P_{\text{s.s.}}(0) = 4\left|\frac{\varepsilon g}{\Omega_0\Delta}\right|^2 , \tag{4.21}$$

which is close to the numerical value for $P_{\max}$ in Fig. 4.2(a). As discussed below, the oscillations eventually dephase, so we would expect the value $P_{\text{stray}} = P_{\max}/2$ after that. However, by the time it occurs, $P_{\text{s.s.}}$ in Eq. (4.20), shown by the dashed black line in Fig. 4.2(a), significantly decreases because $\bar{n}$ is already large. As a result, we expect the value $P_{\text{stray}} = P_{\text{s.s.}}(0) + P_{\text{s.s.}}(t)$ after decay of the oscillations. (Here the first term comes from continuing dephased oscillations while the second term comes from the moving center of oscillations on the complex plane of c.) This formula is also close to the numerical result in Fig. 4.2(a).

Figures 4.3(a–d) show in more detail that the functional form of Eq. (4.21) agrees well with the numerically obtained maximum stray populations $P_{\max}$ in the case of a sudden drive. In contrast, when the drive $\varepsilon(t)$ is adiabatically increased from zero, then the stray population closely follows the time-dependent steady state $P_{\text{s.s.}}$ of Eq. (4.20), as shown in Fig. 4.2(b). Our analysis based on Eq. (4.19) predicts that in the diabatic case of a sudden drive, the oscillation frequency $\Omega_{\bar{n}}$

should increase when $\bar{n}$ increases. This is checked in Fig. 4.3(e); agreement with numerical results is again very good.

Now let us discuss the decay of oscillations seen in Fig. 4.2(a). Numerical results show that the oscillations decay only for a resonant drive (for a strongly off-resonant drive, $\bar{n} \ll 1$ and oscillations do not decay). Therefore, we assume a resonant drive, so that $\bar{n}(t) \approx |\varepsilon t|^2$. Let us now take into account the spread in photon number $\bar{n} \pm \sqrt{\bar{n}}$, which produces a corresponding spread in oscillation frequency $\Omega_n = \Delta_n$ in Eq. (4.19) that dephases the oscillations. At sufficiently low photon number (up to several n_c), we can use the approximation

$$\Delta_n \approx \Delta - 2\chi n, \;\; \chi \approx -\frac{\omega_{\rm r}}{\omega_{\rm q}} \frac{g^2\eta}{\Delta(\Delta+\eta)}, \tag{4.22}$$

which produces the spread of oscillation frequency in Eq. (4.19) with the standard deviation $\delta\Omega \simeq 2\chi\sqrt{\bar{n}} \approx 2\chi|\varepsilon|t$. This implies that the corresponding accumulated phase difference after a time t is $\delta\varphi = \int_0^t \delta\Omega\, dt' \approx \chi|\varepsilon|t^2$. Assuming that a phase accumulation of $|\delta\varphi| \simeq 1$ indicates a significant level of dephasing, this estimate yields an oscillation decay time

$$t_{\rm decay} \simeq |\chi\varepsilon|^{-1/2}, \tag{4.23}$$

with an unknown prefactor on the order of 1. This estimate crudely agrees with the oscillation decay in Fig. 4.2(a). For a more detailed analysis we checked the numerical dependence of the decay time on ε and χ in Figs. 4.3(f) and 4.3(g). The agreement is quite good using a prefactor of 1.23 in Eq. (4.23), when the decay time is defined numerically as decay of the probability oscillations [as in Fig. 4.2(a)] to 1/3 of initial amplitude. Note that this derivation predicts a crudely Gaussian envelope of oscillation decay for $\sqrt{P_{\rm stray}(t)}$, and this prediction also agrees with the numerical results (though not quite well because of the change of the oscillation center $c_{\rm s.s.}$ over time).

Simple modifications of the above derivation are sufficient to describe the stray populations when starting from a different initial state. As an example, let us consider an initially excited qubit state $\overline{|0,1\rangle}$. In this case there will be two neighboring eigenladders that interact: the ground eigenladder $\overline{|n,0\rangle}$, and the second excited eigenladder $\overline{|n,2\rangle}$. Stray population that leaks to the ground eigenladder will oscillate precisely as before between the ground and excited eigenladders, reproducing Eqs. (4.20), (4.21), and (4.23); this equivalence due to symmetry is emphasized in Fig. 4.2(c). In contrast, the stray population leaking to the second excited eigenladder $\overline{|n,2\rangle}$ oscillates between excited and second-excited eigenladders, so behaves somewhat differently. We modify our derivation starting from Eq. (4.18) to include only the interaction between the eigenladders $\overline{|n,1\rangle}$ and $\overline{|n,2\rangle}$, which yields the following parameter replacements: $g \to \sqrt{2}\,g$, $\Delta_n \to \overline{E}_{n+1,1} - \overline{E}_{n,2}$, $\Delta \to \Delta + \eta$, $\Omega_0 \to \Omega_0 + \eta$, and $2\chi \to 2\chi' = \omega_{\rm r}^{(2)}(0) - \omega_{\rm r}^{(1)}(0)$. Thus, the equivalents of Eqs. (4.20) and (4.23) at low n are

$$P'_{\rm s.s.} = \left| \frac{\sqrt{2}\,\varepsilon g}{(\Delta + \eta - 2\chi'\bar{n})(\Omega_0 + \eta - 2\chi'\bar{n})} \right|^2, \tag{4.24}$$

$$t'_{\rm decay} \simeq |\chi'\varepsilon|^{-1/2}. \tag{4.25}$$

These equations agree with the numerical results shown in Fig. 4.2(d) and Fig. 4.3(h,i).

Our analysis shows that the stray population of a “wrong” eigenladder considered in this section should be quite small for typical experimental parameters. The case of an adiabatically increased drive is more experimentally relevant, so let us use Eq. (4.20) and crudely estimate the effect as $P_{\mathrm{stray}} \sim (\varepsilon g/\Delta^2)^2$. Then for $g/2\pi \simeq 100$ MHz, $\Delta/2\pi \simeq 1$ GHz, and $\varepsilon/2\pi \simeq 50$ MHz (such drive pumps ~ 10 photons within first 10 ns), we obtain $P_{\mathrm{stray}} \sim 3 \times 10^{-5}$. Even if $\Delta/2\pi$ is decreased to 500 MHz in this estimate and $\varepsilon/2\pi$ is increased to 100 MHz (40 photons within first 10 ns), the resulting value $P_{\mathrm{stray}} \sim 2 \times 10^{-3}$ still remains quite small. Therefore, this should not significantly affect the qubit measurement error, at least for present-day experiments.

4.4 Summary

We have analyzed the ring-up of a readout resonator coupled to a transmon qubit. The bare bases of the transmon and resonator hybridize into a joint eigenbasis that is organized into natural eigenladders associated with each nominal transmon state. As was pointed out previously, ringing up the resonator from its ground state using a coherent pump approximately creates a coherent state in this eigenbasis (i.e., a dressed coherent state) that is confined to the eigenladder corresponding to the initial transmon state. We analyzed one main deviation from this first approximation and developed a more accurate dynamical model for the ring-up process.

Through numerical simulation, we demonstrated that the ring-up evolution deviates from the dressed coherent state model. The initial transmon population may leak into other ("incorrect") eigenladders that correspond to different initial transmon states. We analyzed this deviation and developed analytical models to quantify the effects.

The stray population that leaks outside the correct eigenladder arises from the mismatch between the coherent pump (in the bare basis) and the hybridized resonator (in the eigenbasis). We found that this mismatch creates interesting dynamics over a relatively short timescale after the pump is applied, and were able to describe the resulting damped oscillations between neighboring eigenladders quantitatively. The most important result is that for typical experimental parameters the occupation of incorrect eigenladders remains small ($\lesssim 10^{-4}$); therefore, this effect should not significantly contribute to the qubit measurement error in present-day experiments. Note, however, that our analysis focuses solely on the population leakage caused by the pump itself during the ring-up process; as such, it neglects other important effects that contribute to the total leakage to incorrect eigenladders in practice, such as qubit energy relaxation, the Purcell effect, interactions with defects, dressed dephasing, and non-RWA effects.

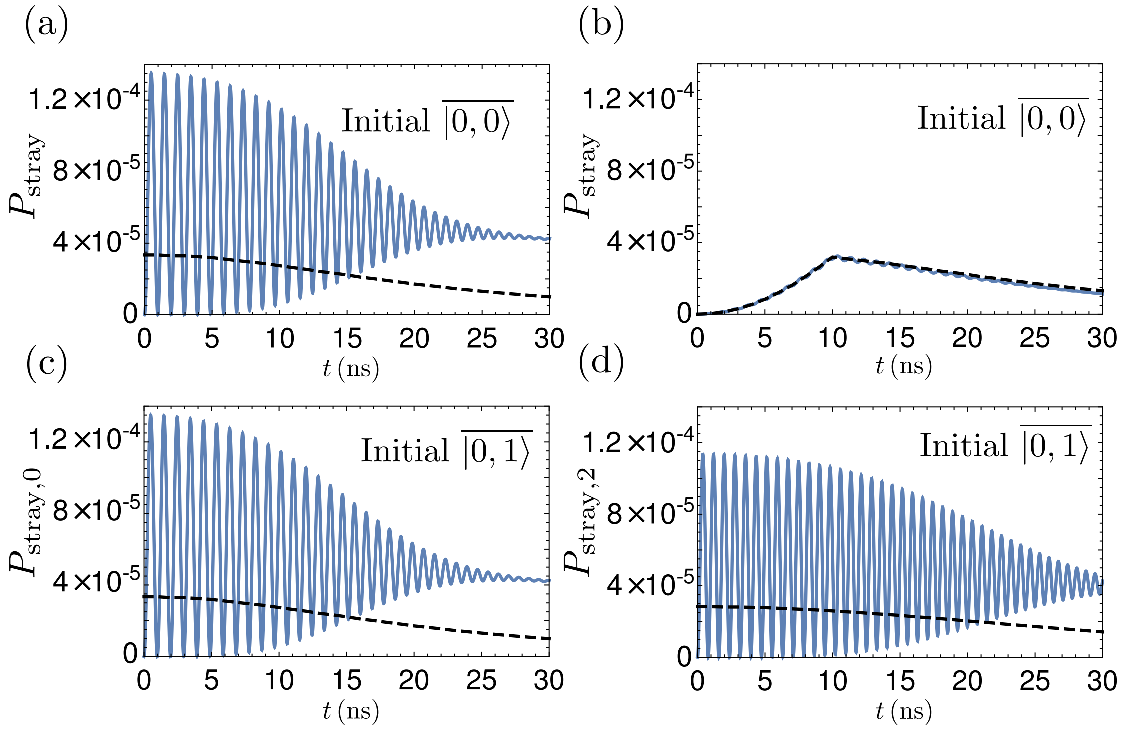

Figure 4.2: Blue lines: numerically calculated stray population P_{stray} as a function of time t; dashed black lines: steady-state value $P_{\mathrm{s.s.}}$, calculated via Eq. (4.20). (a) Leaked population in the excited eigenladder $\overline{|n,1\rangle}$ for sudden driving with $\varepsilon/2\pi = 60\,\mathrm{MHz}$ from initial ground state $|0,0\rangle$. The oscillations reach an initial maximum of $P_{\max} \approx 4P_{\mathrm{s.s.}}(0)$, then dephase to about $P_{\mathrm{s.s.}}(t) + P_{\mathrm{s.s.}}(0)$, with decreasing $P_{\mathrm{s.s.}}(t)$ because of increasing average photon number $\bar{n}$. (b) The same for adiabatic drive $\varepsilon(t)$, linearly increasing for first 10 ns to the same constant value of 60 MHz. The stray population follows the steady state, which increases for 10 ns because of increasing $\varepsilon(t)$. (c) Sudden driving with $\varepsilon/2\pi = 60\,\mathrm{MHz}$ from an initial excited qubit state $\overline{|0,1\rangle}$, showing population $P_{\mathrm{stray},0}$ leaked to the ground-state eigenladder $\overline{|n,0\rangle}$. This case is fully symmetric with (a) since it involves the same pair of transmon levels. (d) The same driving as in (c), but showing leaked population $P_{\mathrm{stray},2}$ of the second-excited eigenladder $\overline{|n,2\rangle}$. The behavior is similar to (c), but involves the next pair of transmon levels. For all panels $\omega_{\mathrm{r}}/2\pi = 6\,\mathrm{GHz}$, $\omega_{\mathrm{q}}/2\pi = 5\,\mathrm{GHz}$, $\eta/2\pi = 250\mathrm{MHz}$, $g/2\pi = 100\,\mathrm{MHz}$, and ω_{d} is on resonance with the resonator frequency, corresponding to each initial state.

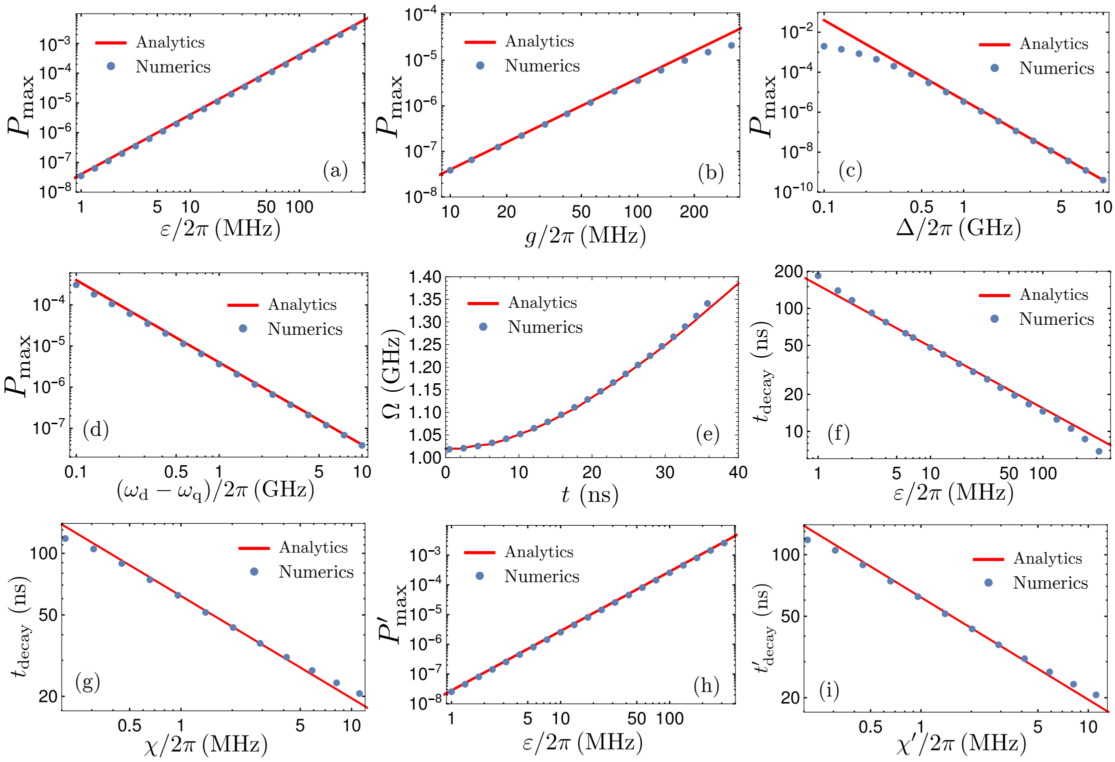

Figure 4.3: Model validation for stray population P_{stray} in the neighboring eigenladder, using a sudden resonant [off-resonant in (d)] drive and starting with $|0,0\rangle$ (a-g) or $|0,1\rangle$ (h,i). Panels (a–d): Testing of Eq. (4.21) for the maximum stray population $P_{\max}$ against numerical results, by varying (a) the drive amplitude ε, (b) coupling g, (c) resonator-qubit detuning Δ, and (d) drive frequency ω_{d}. (e): Testing that the time-dependent oscillation frequency evolves as $\Omega_{\bar{n}} = \Delta_{\bar{n}}$ given by Eq. (4.16). (f,g): Testing of Eq. (4.23) for the decay time t_{decay} of the eigenladder oscillations [as in Fig. 4.2(a)], using a prefactor of 1.23 for decay to 1/3 amplitude. (h,i): Similar to panels (a,g), but for the leakage to the second excited eigenladder $|n,2\rangle$ starting from the excited state $|0,1\rangle$; in this case Eqs. (4.21) and (4.23) need the following replacements: $g \mapsto \sqrt{2}\,g$, $\Delta \mapsto \Delta+\eta$, $\Omega_0 \mapsto \Omega_0+\eta$, $\chi \mapsto \chi' = \omega_{\mathrm{r}}^{(2)} - \omega_{\mathrm{r}}^{(1)}$. In all panels blue dots show numerical results, while red lines are calculated analytically. We use the following parameters: $\omega_{\mathrm{r}}/2\pi = 6\,\mathrm{GHz}$, $\omega_{\mathrm{q}}/2\pi = 5\,\mathrm{GHz}$, $\eta/2\pi = 200\,\mathrm{MHz}$, $g/2\pi = 100\,\mathrm{MHz}$, $\varepsilon/2\pi = 10\,\mathrm{MHz}$, except for parameters, which are varied, and in (g) $\varepsilon/2\pi = 50\,\mathrm{MHz}$ and in (h,i) $\eta/2\pi = 300\,\mathrm{MHz}$.

Chapter 5

Testing the Robustness of Quantum State Transfer

Present realizations of superconducting qubits are restricted to one chip inside a dilution refrigerator. While this is sufficient for the implementation of only a few qubits, future developments and upward scaling will require interconnects between several chips of superconducting qubits. The realization of quantum networks with many nodes and the transfer of quantum states from site to site therefore rely on a high-fidelity quantum state transfer protocol.

The use of photons traveling in optical fibers is the standard method of sharing quantum information across a significant length, with photons able to travel a long distance before decohering. These "flying qubit" could be used for many purposes within quantum communication. But the advantages that optics can provide through relatively-coherent photons can be misleading. Among other difficulties, the photons must be captured without being destroyed in order for quantum information to be transferred in this way.

Flying qubits need not be restricted to optical photons and optical waveguides. It may be useful instead to use microwave photons that travel through superconducting waveguides to achieve the transfer of quantum states. In this chapter, we analyze the transfer of a quantum state between two resonators connected by a superconducting transmission line. Nearly perfect state-transfer efficiency can be achieved by using adjustable couplers and destructive interference to cancel the back-reflection into the transmission line at the receiving coupler.

We show that the transfer protocol is robust to parameter variations affecting the transmission amplitudes of the couplers. We also show that the effects of Gaussian filtering, pulse-shape noise, and multiple reflections on the transfer efficiency are insignificant. However, the transfer protocol is very sensitive to frequency mismatch between the two resonators. Moreover, the tunable coupler we considered produces time-varying frequency detuning caused by the changing coupling. This detuning requires an active frequency compensation with an accuracy better than 90% to yield the transfer efficiency above 99%.

The chapter is organized in the following way. In Sec. 5.1 we stage the problem with appropriate background. In Sec. 5.2 we discuss the ideal state transfer protocol, its mathematical model, and the relation between classical transfer efficiency (which is mostly used throughout this chapter) and quantum state/process fidelity. In Sec. 5.3 we analyze the decrease of the transfer efficiency due to deviations from the design values of various parameters that define the transmission amplitudes of the couplers. We also study the effects of pulse-shape warping, Gaussian filtering, noise, and dissipative losses. In Sec. 5.4 we analyze the effect of multiple reflections of the back-reflected field on the transfer efficiency. The effect of frequency mismatch between the two resonators is discussed in Sec. 5.5. Finally, we summarize the main results of this chapter in Sec. 5.6.

It should be noted that the two appendices that appear in this dissertation also relate to this work. Appendix A is devoted to the quantum theory of a beam splitter, which is used to relate the efficiency of a classical state transfer to the fidelity of a quantum state transfer. In Appendix B we discuss the theory of the tunable coupler of Refs. [106, 107] and find the frequency detuning caused by the coupling variation.

5.1 Introduction

The realization of quantum networks composed of many nodes requires high-fidelity protocols that transfer quantum states from site to site by using “flying qubits” [42, 14]. The standard idea of the state transfer between two nodes of a quantum network [108] assumes that the state of a qubit is first encoded onto a photonic state at the emitting end, after which the photon leaks out and propagates through a transmission line to the receiving end, where its state is transferred onto the second qubit. The importance of quantum state transfer has stimulated significant research activity in optical realizations of such protocols, e.g., [109, 110, 111], including trapping of photon states in atomic ensembles [112, 113, 114, 115]. Recent experimental demonstrations include the transfer of an atomic state between two distant nodes [116] and the transfer between an ion and a photon [117].

An important idea for state transfer in the microwave domain is to use tunable couplers between the quantum oscillators and the transmission line [118, 119] (the idea is in general similar to the idea proposed in Ref. [108] for an optical system). In particular, this strategy is natural for superconducting qubits, for which a variety of tunable couplers have been demonstrated experimentally [120, 121, 122, 123, 124, 106, 125, 107, 126, 127, 128] (these couplers are important for many applications, e.g., [53, 63, 76, 129]). Although there has been rapid progress in superconducting qubit technology, e.g. [87, 88, 130, 131, 132, 133, 134, 135, 136], most of the experiments so far are limited to a single chip or a single resonator in a dilution refrigerator (an exception is [137]). Implementing the quantum state transfer between remote superconducting qubits, resonators, or even different refrigerators using "flying" microwave qubits propagating through lossless superconducting waveguides would significantly extend the capability of the technology (eventually permitting distributed quantum computing and quantum communications over extended distances using quantum repeaters).

The essential ingredients of the transfer protocol proposed in Ref. [119] have already been demonstrated experimentally. The emission of a proper (exponentially increasing) waveform of a quantum signal has been demonstrated in Ref. [125], while the capture of such a waveform with 99.4% efficiency has been demonstrated in Ref. [107]. The combination of these two procedures in one experiment would demonstrate a complete quantum state transfer (more precisely, the complete first half of the procedure of Ref. [119]). Note that Refs. [125] and [107] used different tunable couplers: a “tunable mirror” [106] between the resonator and the transmission line in Ref. [107] and a tunable coupling between the qubit and the resonator [124] (which then rapidly decays into the transmission line) in Ref. [125]. However, this difference is insignificant for the transfer protocol of Ref. [119]. Another promising way to produce shaped photons is to use a modulated microwave drive to couple the superconducting qubit with the resonator [138, 139] (see also Refs. [140, 141] for implementation of optical techniques for shaped photons).

In this chapter, we extend the theoretical analysis of the state transfer protocol proposed in Ref. [119], focusing on its robustness against various imperfections. In our protocol a quantum state is transferred from the emitting resonator to the receiving resonator through a transmission line (the state transfer using tunable coupling directly between the qubit and the transmission line has also been considered in Ref. [119], but we do not discuss it here). The procedure essentially relies on the cancellation of back-reflection into the transmission line via destructive interference at the receiving end, which is achieved by modulation of the tunable couplers between the resonators and the transmission line. (Note that the protocol is often discussed in terms of a “time reversal”, following the terminology of Ref. [108]; however, we think that discussion in terms of a destructive interference is more appropriate.) In Ref. [119], it was shown that nearly perfect transfer efficiency can be achieved if identical resonators and proper time-varying transmission amplitudes of the two couplers are used. However, in obtaining this high-efficiency state transfer, only ideal design parameters were assumed. Also, various experimentally relevant effects, including multiple reflections and frequency mismatch between the two resonators, were not analyzed quantitatively.

We study in detail (mostly numerically) the effect of various imperfections that affect the transmission amplitudes of the couplers. In the simulations we focus on two values for the design efficiency: 0.99 and 0.999. The value of 0.99 crudely corresponds to the current state of the art for the two-qubit quantum gate fidelities [87] and threshold of some quantum codes [78]; we believe that the state transfer with 0.99 efficiency may already be interesting for practical purposes, while the value of 0.999 would be the next natural milestone for the experimental quantum state transfer. We find that the transfer protocol is surprisingly robust to parameter variations, with a typical decrease in the efficiency of less than 1% for a 5% variation of the design parameters (the scaling is typically quadratic, so half of the variation produces a quarter of the effect). We also study the effect of Gaussian filtering of the signals and find that it is practically negligible. The addition of noise to the ideal waveforms produces only a minor decrease in the transfer efficiency. Numerical analysis of multiple reflections also shows that the corresponding effect is not significant and can increase the inefficiency by at most a factor of two. The analysis of the effect of dissipative losses is quite simple and, as expected, shows that a high-efficiency state transfer requires a low-loss transmission line and resonators with energy relaxation times much longer than duration of the procedure.

A major concern, however, is the effect of frequency mismatch between the two resonators, since the destructive interference is very sensitive to the frequency detuning. We consider two models: a constant-in-time detuning and a time-dependent detuning due to changing coupling. For the latter model we use the theory of the coupler realized in Refs. [106, 107]; the frequency variation due to the coupling modulation has been observed experimentally [106]. Our results show that a high-efficiency state transfer is impossible without an active compensation of the frequency change; the accuracy of this compensation should be at least within the 90%-95% range.

Although we assume that the state transfer is performed between two superconducting resonators, using the tunable couplers of Refs. [106, 107], our analysis can also be applied to other setups, for example, schemes based on tunable couplers between the qubits and the transmission line or based on the tunable couplers between the qubits and the resonators [124, 125, 138, 139], which are then strongly coupled with the transmission line. Note that the frequency change compensation is done routinely in the coupler of Refs. [124, 125], thus giving a natural way to solve the problem of frequency mismatch. Similarly, the phase is naturally tunable in the coupler of Refs. [138, 139].

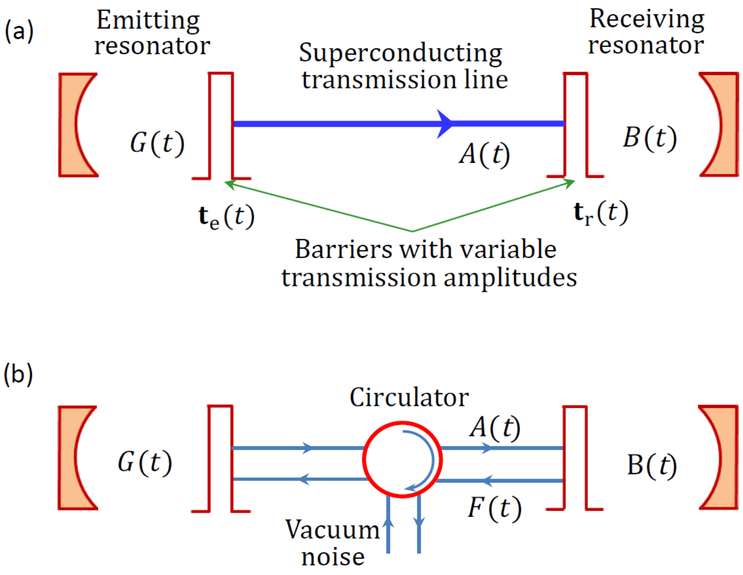

Figure 5.1: (a) The state transfer setup. An initial microwave field amplitude $G(0)$ is transferred from the emitting resonator to the receiving resonator via a transmission line. This is done using variable couplers for both resonators, characterized by (effective) transmission amplitudes $\mathbf{t}_{\mathrm{e}}(t)$ and $\mathbf{t}_{\mathrm{r}}(t)$, and corresponding leakage rates $\kappa_{\mathrm{e}}(t)$ and $\kappa_{\mathrm{r}}(t)$. Almost perfect transfer can be achieved when the back-reflection of the propagating field $A(t)$ is cancelled by arranging its destructive interference with the leaking part of the field $B(t)$ in the receiving resonator. (b) A variant of the setup that includes a circulator, which prevents multiple reflections of the small back-reflected field $F(t)$.

5.2 Model and transfer protocol

5.2.1 Model

We consider the system illustrated in Fig. 5.1(a). A quantum state is being transferred from the emitting (left) resonator into the initially empty receiving (right) resonator via the transmission line. This is done by using time-varying couplings ("tunable mirrors") between the resonators and the transmission line. The (effective) transmission amplitudes $\mathbf{t}_{\mathrm{e}}$ and $\mathbf{t}_{\mathrm{r}}$ for the emitting and receiving resonator couplers, respectively, as a function of time t are illustrated in Fig. 5.2. As discussed later, the main idea is to almost cancel the back-reflection into the

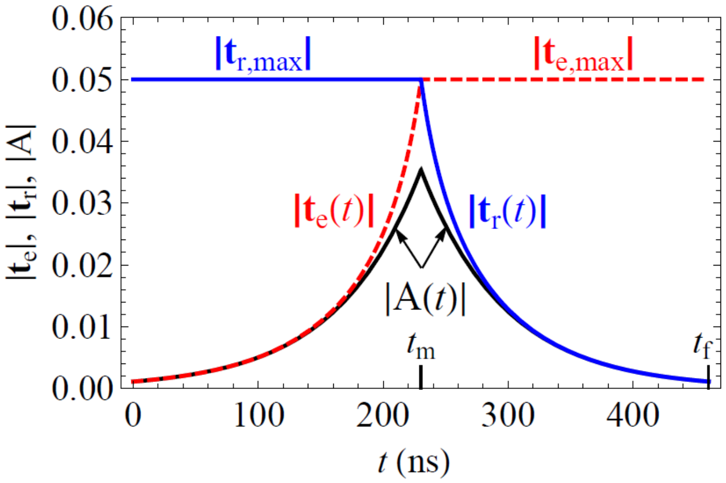

Figure 5.2: Time dependence ("pulse shapes") of the absolute values of transmission amplitudes $\mathbf{t}_\mathrm{e}(t)$ for the emitting coupler (red dashed curve) and $\mathbf{t}_\mathrm{r}(t)$ for the receiving coupler (blue solid curve). The amplitude $\mathbf{t}_\mathrm{e}(t)$ is kept constant at the maximum level $\mathbf{t}_\mathrm{e,max}$ after the mid-time t_m, while $\mathbf{t}_\mathrm{r}(t)$ is kept at the maximum $\mathbf{t}_\mathrm{r,max}$ during the first part of the procedure, $t \leq t_\mathrm{m}$. The propagating field $A(t)$ first increases exponentially and then decreases exponentially (black solid curve). In simulations we typically use $|\mathbf{t}_\mathrm{e,max}| = |\mathbf{t}_\mathrm{r,max}| = 0.05$ for quarter-wavelength 6 GHz resonators ($\tau_\mathrm{e} = \tau_\mathrm{r} = 33$ ns); then the transfer efficiency $\eta = 0.999$ requires the procedure duration of $t_\mathrm{f} = 460$ ns.

transmission line from the receiving resonator by using destructive interference. Then the field leaking from the emitting resonator is almost fully absorbed into the receiving resonator. Ideally, we want the two resonators to have equal frequencies, $\omega_\mathrm{e} = \omega_\mathrm{r}$; however, in the formalism we will also consider slightly unequal resonator frequencies $\omega_\mathrm{e}(t)$ and $\omega_\mathrm{r}(t)$. We assume large quality factors Q for both resonators by assuming $|\mathbf{t}_\mathrm{e}(t)| \ll 1$ and $|\mathbf{t}_\mathrm{r}(t)| \ll 1$ (the maximum value is crudely $|\mathbf{t}_\mathrm{e(r),max}| \sim 0.05$, leading to $Q_\mathrm{min} \sim 10^3$ – see later), so that we can use the single-mode approximation. For simplicity, we assume a dispersionless transmission line.

We will mostly analyze a classical field transfer between the two resonators, with a straightforward relation to the quantum case, discussed later. The notations $G(t)$ and $B(t)$ correspond to the field amplitudes in the emitting and receiving resonators [see Fig. 5.1(a)], while $A(t)$ describes the propagating field in the transmission line. However, in contrast to the notations of Ref. [119], here we use dimensionless G and B, normalizing the field amplitudes [142, 143] in such a way that for classical (coherent) fields, $|G|^2$ and $|B|^2$ are equal to the average number of photons in the resonators. Similarly, the normalization of A is chosen so that $|A|^2$ is the number of propagating photons per second. Such normalizations for resonators are more appropriate for the analysis of quantum information. Also, with this normalization, the amplitudes will not change with adiabatically-changing resonator frequency, in contrast to the usual field amplitudes.

In most of the analysis we assume (unless mentioned otherwise) that the transmission line is either long or contains a circulator [Fig. 5.1(b)], so that we can neglect the multiple reflections of the small back-propagating field $F(t)$ (the effect of multiple reflections will be considered in Sec. IV). We also assume that there is no classical noise entering the emitting resonator from the circulator (only vacuum noise).

With these assumptions and normalizations, the time dynamics of the classical field amplitudes is described in the rotating frame by the equations

$$\dot{G} = -i\Delta\omega_{\rm e} G - \frac{1}{2}\left(\kappa_{\rm e} + T_{1,\rm e}^{-1}\right) G, \tag{5.1}$$

$$\dot{B} = -i\Delta\omega_{\rm r} B - \frac{1}{2}\left(\kappa_{\rm r} + T_{1,\rm r}^{-1}\right) B + \frac{\mathbf{t}_{\rm r}}{|\mathbf{t}_{\rm r}|}\sqrt{\kappa_{\rm r}}\, A, \tag{5.2}$$

$$A = \sqrt{\eta_{\rm tl}}\, \frac{\mathbf{t}_{\rm e}}{|\mathbf{t}_{\rm e}|}\sqrt{\kappa_{\rm e}}\, G, \tag{5.3}$$

where $\Delta\omega_{\rm e} = \omega_{\rm e} - \omega_0$ and $\Delta\omega_{\rm r} = \omega_{\rm r} - \omega_0$ are small detunings (possibly changing slowly with time) from the (arbitrary) rotating frame frequency $\omega_0(t)$, the decay rates $\kappa_{\rm e}$ and $\kappa_{\rm r}$ are due to leakage into the transmission line, while additional losses are described by the energy relaxation times $T_{1,{\rm e}}$ and $T_{1,{\rm r}}$ in the resonators and imperfect transfer efficiency $\eta_{\rm tl}$ of the transmission line. Note that A has the dimension of $1/\sqrt{\rm s}$ in contrast to the dimensionless G and B, so that the factors $\sqrt{\kappa_{\rm e(r)}}$ restore the proper dimension. The leakage rates are

$$\kappa_{\rm e}(t) = \frac{|\tilde{\mathbf{t}}_{\rm e}^{\rm in}|^2}{\tau_{\rm rt,e}} \frac{R_{\rm e}}{R_{\rm tl}} = \frac{|\mathbf{t}_{\rm e}|^2}{\tau_{\rm rt,e}}, \;\; \kappa_{\rm r}(t) = \frac{|\tilde{\mathbf{t}}_{\rm r}^{\rm in}|^2}{\tau_{\rm rt,r}} \frac{R_{\rm r}}{R_{\rm tl}} = \frac{|\mathbf{t}_{\rm r}|^2}{\tau_{\rm rt,r}}, \tag{5.4}$$

where $\tilde{\mathbf{t}}_{\rm e}^{\rm in}$ and $\tilde{\mathbf{t}}_{\rm r}^{\rm in}$ are the transmission amplitudes of the couplers (for a wave incident from inside of the resonators), $\tau_{\rm rt,e}$ and $\tau_{\rm rt,r}$ are the round-trip times in the resonators, $R_{\rm e}$, $R_{\rm r}$, and $R_{\rm tl}$ are the wave impedances of the resonators and the transmission line, while $\mathbf{t}_{\rm e} = \tilde{\mathbf{t}}_{\rm e}^{\rm in}\sqrt{R_{\rm e}/R_{\rm tl}}$ and $\mathbf{t}_{\rm r} = \tilde{\mathbf{t}}_{\rm r}^{\rm in}\sqrt{R_{\rm r}/R_{\rm tl}}$ are the effective transmission amplitudes. Note that the transmission amplitudes $\tilde{\mathbf{t}}$ depend on the wave direction (from inside or outside of a resonator), while the effective transmission amplitudes $\mathbf{t}$ do not. For convenience we will be working with the effective transmission amplitudes $\mathbf{t}_{\rm e}$ and $\mathbf{t}_{\rm r}$, so that we do not need to worry about possibly unequal wave impedances. For quarter-wavelength resonators $\tau_{\rm rt,e} \approx \pi/\omega_{\rm e} \approx \pi/\omega_0$ and $\tau_{\rm rt,r} \approx \pi/\omega_{\rm r} \approx \pi/\omega_0$, so the quality factors are

$$Q_{\rm e(r)} = \frac{\omega_{\rm e(r)}}{\kappa_{\rm e(r)}} \approx \frac{\pi}{|\mathbf{t}_{\rm e(r)}|^2}. \tag{5.5}$$

Note that the phase factors $\mathbf{t}_{\rm r}/|\mathbf{t}_{\rm r}|$ and $\mathbf{t}_{\rm e}/|\mathbf{t}_{\rm e}|$ in Eqs. (5.2) and (5.3) may change in time because of changing coupling [119, 106] (as discussed later in Sec. 5.5.2 and Appendix B); this is why these somewhat unusual factors cannot be neglected. Strictly speaking, the last term in Eq. (5.2) should also be multiplied by $\sqrt{\omega_{\rm e}/\omega_{\rm r}}$; this is because of different normalizations, related to different photon energies $\hbar\omega_{\rm e}$ and $\hbar\omega_{\rm r}$ in the resonators. However, we neglect this correction, assuming a relatively small detuning. Note that the effective propagation time along the transmission line is zero in Eqs. (5.1)–(5.3) since we use appropriately shifted clocks (here the assumption of a dispersionless transmission line is necessary); however, the physical propagation time will be important in the analysis of multiple reflections in Sec. 5.4. Also note that to keep Eqs. (5.1)–(5.3) reasonably simple, we defined the phases of B and G to be somewhat different from the actual phases of the standing waves in the resonators (see discussion in Sec. 5.2.3.

Even though in Eqs. (5.1)–(5.3) we use normalized fields G, B, and A, which imply discussion in terms of the photon number, below we will often use the energy terminology and invoke the arguments of the energy conservation instead of the photon number conservation. At least in the case without detuning the two pictures are fully equivalent, but the energy language is more intuitive, and thus preferable. This is why in the following we will use the energy and photon number terminology interchangeably.

5.2.2 Efficiency and fidelity

We will characterize performance of the protocol via the transfer efficiency η, which is defined as the ratio between the energy of the field (converted into the photon number) in the receiving resonator at the end of the procedure, $t = t_{\rm f}$, and the energy (photon number) at the initial time, $t = 0$, in the emitting resonator:

$$\eta = \frac{|B(t_{\rm f})|^2}{|G(0)|^2}. \tag{5.6}$$

We emphasize that in this definition we assume that only the emitting resonator has initially a non-zero field.

As we discuss in this section, the classical efficiency η is sufficient to characterize the quantum transfer as well, so that the quantum state and process fidelities derived below are directly related to η (this requires assumption of vacuum everywhere except the initial state of the emitting resonator). The idea of the conversion between the classical and quantum transfers is based on the linearity of the process, and thus can be analyzed in essentially the same way as the quantum optical theory of beam splitters, discussed in Appendix A.

Let us focus on the case with the circulator [Fig. 1(b)] in the absence of dissipative losses ($T_{1,\rm e}^{-1} = T_{1,\rm r}^{-1} = 0$, $\eta_{\rm tl} = 1$). In general, there is a linear input-output relation between the fields at $t = 0$ and the fields at $t = t_{\rm f}$. This relation is the same for the classical fields and the corresponding quantum operators in the Heisenberg picture ([144, 118]), so for simplicity we discuss the classical fields. The relevant fields at $t = 0$ are $G(0)$, $B(0)$, and the (infinite number of) temporal modes propagating towards the emitting resonator through the circulator; these modes can be described as time-dependent field $V(t)$, where t corresponds to the time, at which the field arrives to the emitting resonator. Note that $B(0)$ and

$V(t)$ are assumed to be zero in our protocol; however, we need to take them into account explicitly, because in the quantum language they would correspond to operators, representing vacuum noise (with the standard commutation relations). The fields at the final time $t = t_\mathrm{f}$ are $B(t_\mathrm{f})$, $G(t_\mathrm{f})$, and the collection of the outgoing back-reflected fields $F(t)$ for $0 \le t \le t_\mathrm{f}$ [see Fig. 1(b)]. Note that normalization of the propagating fields $V(t)$ and $F(t)$ is similar to the normalization of $A(t)$.

The input-output relation $\{G(0), B(0), V(t)|_{0\le t\le t_\mathrm{f}}\} \mapsto \{G(t_\mathrm{f}), B(t_\mathrm{f}), F(t)|_{0\le t\le t_\mathrm{f}}\}$ is linear and unitary, physically because of the conservation of the number of photons (energy). In particular,

$$B(t_\mathrm{f}) = \sqrt{\eta}\, e^{i\varphi_\mathrm{f}} G(0) + w_B B(0) + \int_0^{t_\mathrm{f}} w_V(t) V(t)\, dt, \tag{5.7}$$

where η is obviously given by Eq. (5.6), φ_f is the phase shift between $B(t_\mathrm{f})$ and $G(0)$, while w_B and $w_V(t)$ are some weight factors in this general linear relation. These weight factors can be calculated by augmenting Eqs. (5.1)–(5.3) to include $V(t)$ and $F(t)$, but we do not really need them to find the quantum transfer fidelity if $B(0)$ and $V(t)$ correspond to vacuum. Note that the unitarity of the input-output transformation requires the relation

$$\eta + |w_B|^2 + \int_0^{t_\mathrm{f}} |w_V(t)|^2\, dt = 1 \tag{5.8}$$

(sum of squared absolute values of elements in a row of a unitary matrix equals one), where we neglected the slight change in the normalization (discussed above) in the case of time-varying detuning.

This picture of the input-output relations can in principle be extended to include non-zero $T_{1,\mathrm{e(r)}}^{-1}$ and/or $\eta_{\mathrm{tl}} \neq 1$; for that we would need to introduce additional noise sources, which create additional terms in Eqs. (5.7) and (5.8) similar to the terms from the noise V. Also, if we consider the case without the circulator, the structure of these equations remains similar, but the role of $V(t)$ is played by the temporal modes of the initial field propagating in the transmission line from the receiving to the emitting resonator (since clocks are shifted along the transmission line, there is formally no field "stored" in the transmission line, which propagates from the emitting to the receiving resonator).

Using the framework of the linear input-output relation, Eq. (5.7) derived for classical fields can also be used to describe the quantum case. This can be done using the standard quantum theory of beam splitters [143] (see Appendix A), by viewing Eq. (5.7) as the result of mixing the fields $G(0)$, $B(0)$, and an infinite number of fields (temporal modes) $V(t)$ with beam splitters to produce the proper linear combination. Importantly, if $B(0)$ corresponds to vacuum and $V(t)$ also corresponds to vacuum, then we can assume only one beam splitter with the proper transfer amplitude $\sqrt{\eta}\, e^{i\varphi_{\mathrm{f}}}$ for $G(0) \to B(t_{\mathrm{f}})$; this is because a linear combination of several vacua is still the vacuum. Equivalently, the resulting quantum state in the receiving resonator is equal to the initial quantum state of the emitting resonator, subjected to the phase shift φ_{f} and leakage (into vacuum) described by the (classical) efficiency η. The same remains correct in the presence of nonzero relaxation rates $T_{1,\mathrm{e}}^{-1}$ and $T_{1,\mathrm{r}}^{-1}$ and imperfect η_{tl} if these processes occur at zero effective temperature (involving only vacuum noise).

As shown in Appendix A, if the initial state in the emitting resonator is $|\psi_{\rm in}\rangle = \sum_n \alpha_n |n\rangle$ in the Fock space ($\sum_n |\alpha_n|^2 = 1$), then the final state of the receiving resonator is represented by the density matrix, which can be obtained from the state $|\psi_{\rm fin}\rangle = \sum_{n,k} \alpha_{n+k} \sqrt{(n+k)!/n!k!}\, \eta^{n/2}(1-\eta)^{k/2} e^{i(n+k)\varphi_{\rm f}} |n\rangle |k\rangle_{\rm a}$ by tracing over the ancillary state $|k\rangle_{\rm a}$ (this ancilla corresponds to the second outgoing arm of the beam splitter). This gives the density matrix

$$\rho_{\rm fin} = \sum_{j,n,m} \alpha_{n+j}\alpha^*_{m+j} \sqrt{(n+j)!(m+j)!} (j!\sqrt{n!m!})^{-1} \eta^{(n+m)/2} (1-\eta)^j e^{i(n-m)\varphi_{\rm f}}) |n\rangle\langle m|$$

The state fidelity (overlap with the initial state) is then

$$F_{\rm st} = \sum_{j,n,m} \frac{\sqrt{(n+j)!(m+j)!}}{j!\sqrt{n!m!}}\, \alpha^*_n \alpha_m \alpha_{n+j} \alpha^*_{m+j} \\ \times \eta^{(n+m)/2} (1-\eta)^j e^{i(n-m)\varphi_{\rm f}}. \tag{5.9}$$

Note that the phase shift $\varphi_{\rm f}$ can easily be corrected in an experiment (this correction is needed anyway for resonators, which are significantly separated in space), and then the factor $e^{i(n-m)\varphi_{\rm f}}$ in Eq. (5.9) can be removed.

The discussed quantum theory (at zero temperature, i.e., with only vacuum noise) becomes very simple if we transfer a qubit state $|\psi_{\rm in}\rangle = \alpha|0\rangle + \beta|1\rangle$. Then the resulting state is

$$|\psi_{\rm fin}\rangle = \alpha|0\rangle|0\rangle_{\rm a} + \beta e^{i\varphi_{\rm f}} (\sqrt{\eta}\, |1\rangle|0\rangle_{\rm a} + \sqrt{1-\eta}\, |0\rangle|1\rangle_{\rm a}), \tag{5.10}$$

where the ancillary states $|1\rangle_{\rm a}$ and $|0\rangle_{\rm a}$ indicate whether a photon was lost to the environment or not. After tracing $|\psi_{\rm fin}\rangle\langle\psi_{\rm fin}|$ over the ancilla we obtain density matrix

$$\rho_{\rm fin} = \begin{pmatrix} \eta|\beta|^2 & \sqrt{\eta}\, e^{i\varphi_{\rm f}}\alpha^*\beta \\ \sqrt{\eta}\, e^{-i\varphi_{\rm f}}\alpha\beta^* & |\alpha|^2+|\beta|^2(1-\eta) \end{pmatrix}. \tag{5.11}$$

Note that since a qubit state contains at most one excitation, the essential dynamics occurs only in the single-photon subspace. Therefore, it is fully equivalent to the dynamics of classical fields (with field amplitudes replaced by probability amplitudes). Thus, Eq. (5.10) can be written directly, without using the quantum beam splitter approach, which is necessary only for multi-photon states.

In quantum computing the qubit state transfer (quantum channel) is usually characterized by the quantum process fidelity F_χ or by the average state fidelity $\overline{F}_{\rm st}$, which are related as [145, 146] $1-F_\chi = (1-\overline{F}_{\rm st})\times 3/2$. In order to calculate F_χ, we calculate state fidelity $F_{\rm st}$ (overlap with initial state) and then average it over the Bloch sphere. Neglecting the phase $\varphi_{\rm f}$, which can be easily corrected in an experiment, from Eq. (5.11) we find $F_{\rm st} = |\alpha|^4+\eta|\beta|^4+|\alpha\beta|^2(1-\eta+2\sqrt{\eta})$, which also follows from Eq. (5.9). To average this fidelity over the Bloch sphere of initial states, it is sufficient [145] (see also [147]) to average it over only six states: $|0\rangle$, $|1\rangle$, $(|0\rangle\pm|1\rangle)/\sqrt{2}$, and $(|0\rangle\pm i|1\rangle)/\sqrt{2}$. This gives $\overline{F}_{\rm st} = (3+\eta+2\sqrt{\eta})/6$, which can be converted into the process fidelity

$$F_\chi = \frac{1}{4}(1+\sqrt{\eta})^2. \tag{5.12}$$

This equation gives the relation between the classical energy transfer efficiency η which we use in this chapter and the process fidelity F_χ used in quantum computing. Note the relation $1-F_\chi \approx (1-\eta)/2$ when $\eta \approx 1$. Also note that a non-vacuum noise contribution (due to finite temperature) always decreases F_χ (see Appendix A). If the phase shift $\varphi_{\rm f}$ is included in the definition of fidelity (assuming that $\varphi_{\rm f}$ is not corrected), then Eq. (5.12) becomes $F_\chi = (1+\eta+2\sqrt{\eta}\cos\varphi_{\rm f})/4$.

Thus, in this section we have shown that the state and the process fidelities of the quantum state transfer are determined by the classical efficiency η and experimentally correctable phase shift $\varphi_{\rm f}$. This is why in the rest of this chapter we analyze the efficiency η of essentially a classical state transfer.

5.2.3 Transfer procedure

Now let us describe the transfer protocol, following Ref. [119] (this will be the second protocol out of two slightly different procedures considered in Ref. [119]). Recall that we consider normalized classical field amplitudes. The main idea of achieving nearly perfect transfer is to use time-dependent transmission amplitudes $\mathbf{t}_{\rm e}$ and $\mathbf{t}_{\rm r}$ to arrange destructive interference between the field A reflected from the receiving resonator and the part of field B leaking through the coupler (see Fig. 5.1). Thus, we want the total back-reflected field $F(t)$ to nearly vanish: $F(t) \approx 0$, where

$$F = \frac{\mathbf{r}_{\rm r}^{\rm out}}{|\mathbf{r}_{\rm r}|}\,A + \frac{\mathbf{t}_{\rm r}}{|\mathbf{t}_{\rm r}|}\,\sqrt{\kappa_{\rm r}}\,\frac{|\mathbf{r}_{\rm r}|}{\mathbf{r}_{\rm r}^{\rm in}}\,B, \tag{5.13}$$

$\mathbf{r}_{\rm r}^{\rm out}$ and $\mathbf{r}_{\rm r}^{\rm in}$ are the coupler reflection amplitudes from the outside and inside of the receiving resonator, and $|\mathbf{r}_{\rm r}| = |\mathbf{r}_{\rm r}^{\rm in}| = |\mathbf{r}_{\rm r}^{\rm out}|$. Note that the (effective) scattering matrix of the receiving resonator coupler is $\begin{pmatrix} \mathbf{r}_\mathrm{r}^\mathrm{out} & \mathbf{t}_\mathrm{r} \\ \mathbf{t}_\mathrm{r} & \mathbf{r}_\mathrm{r}^\mathrm{in} \end{pmatrix}$, when looking from the transmission line. The formula (5.13) looks somewhat unusual for two reasons. First, in the single-mode formalism of Eqs. (5.1)–(5.3), the reflection amplitude in Eq. (5.13) must be treated as having the absolute value of 1; this is why we have the pure phase factor $\mathbf{r}_\mathrm{r}^\mathrm{out}/|\mathbf{r}_\mathrm{r}|$. This is rather counterintuitive and physically stems from the single-mode approximation, which neglects the time delay due to the round-trip propagation in a resonator. It is easy to show that if the actual amplitude $\mathbf{r}_\mathrm{r}^\mathrm{out}$ were used for the reflection $A \to F$, then solution of Eqs. (5.2) and (5.13) would lead to the energy non-conservation on the order of $|\mathbf{t}|^2$. Second, in our definition the phase of the field B corresponds to the standing wave component (near the coupler) propagating away from the coupler [see Eq. (5.2)], so the wave incident to the coupler is $B\,|\mathbf{r}_\mathrm{r}|/\mathbf{r}_\mathrm{r}^\mathrm{in}$, thus explaining the phase factor in the last term of Eq. (5.13). Actually, a better way would be to define B using the phase of the standing wave in the resonator; this would replace the last term in Eq. (5.2) with $(\mathbf{t}_\mathrm{r}/|\mathbf{t}_\mathrm{r}|)\sqrt{\kappa_\mathrm{r}}\,A\sqrt{|\mathbf{r}_\mathrm{r}|/\mathbf{r}_\mathrm{r}^\mathrm{in}}$ and replace the last term in Eq. (5.13) with $(\mathbf{t}_\mathrm{r}/|\mathbf{t}_\mathrm{r}|)\sqrt{\kappa_\mathrm{r}}\sqrt{|\mathbf{r}_\mathrm{r}|/\mathbf{r}_\mathrm{r}^\mathrm{in}}\,B$. However, we do not use this better definition to keep a simpler form of Eq. (5.2).

Using the fact that $\mathbf{t}_\mathrm{r}^2/\mathbf{r}_\mathrm{r}^\mathrm{in}\mathbf{r}_\mathrm{r}^\mathrm{out}$ is necessarily real and negative [since $\mathbf{r}_\mathrm{r}^\mathrm{out} = -(\mathbf{r}_\mathrm{r}^\mathrm{in})^*\mathbf{t}_\mathrm{r}/\mathbf{t}_\mathrm{r}^*$ from unitarity], we can rewrite Eq. (5.13) as

$$F = \frac{\mathbf{r}_\mathrm{r}^\mathrm{out}}{|\mathbf{r}_\mathrm{r}|}\left(A - \frac{\mathbf{t}_\mathrm{r}^*}{|\mathbf{t}_\mathrm{r}|}\sqrt{\kappa_\mathrm{r}}\,B\right). \tag{5.14}$$

This form shows that if the phases of $\mathbf{t}_\mathrm{r}$ and A do not change in time and there is no detuning, then the two terms in Eq. (5.14) have the same phase [because $\arg(B) = \arg(\mathbf{t}_\mathrm{r}A)$ from Eq. (5.2)]. Therefore, for the desired cancellation of the terms we need only the cancellation of absolute values, i.e., a *one-parameter condition*.

For a non-zero field B, the exact back-reflection cancellation can be achieved by varying in time the emitting coupling $\mathbf{t}_\mathrm{e}$ [118], which determines A in Eq. (5.13) or by varying the receiving coupling $\mathbf{t}_\mathrm{r}$ or by varying both of them with an appropriate ratio [119]. At the very beginning of the procedure the exact cancellation is impossible because $B(0) = 0$, so there are two ways to arrange an almost perfect state transfer. First, we can allow for some loss during a start-up time t_s intended to create a sufficient field B, and then maintain the exact cancellation of the back-reflection at $t > t_\mathrm{s}$. Second, we can have a slightly imperfect cancellation during the whole procedure. Both methods were considered in Ref. [119]; in this chapter we discuss only the second method, which can be easily understood via an elegant “pretend” construction explained later.

Motivated by a simpler experimental realization, we divide our protocol into two parts [119] (see Fig. 5.2). During the first part of the procedure, we keep the receiving coupler fixed at its maximum value $\mathbf{t}_\mathrm{r,max}$, while varying the emitting coupler to produce a specific form of $A(t)$ for an almost perfect cancellation. During the second part, we do the opposite: we fix the emitting coupler at its maximum value $\mathbf{t}_\mathrm{e,max}$ and vary the receiving coupler. The durations of the two parts are approximately equal.

The maximum available couplings between the resonators and transmission line determine the timescales $\tau_{\rm e}$ and $\tau_{\rm r}$ of the transfer procedure, which we define as the inverse of the maximum leakage rates,

$$\tau_{\rm e(r)} = \frac{1}{\kappa_{\rm e(r),max}}, \;\; \kappa_{\rm e(r),max} = \frac{|\mathbf{t}_{\rm e(r),max}|^2}{\tau_{\rm rt,e(r)}}. \tag{5.15}$$

The time $\tau_{\rm r}$ affects the buildup of the field in the receiving resonator, while $\tau_{\rm e}$ determines the fastest depopulation of the emitting resonator; we will call both $\tau_{\rm e}$ and $\tau_{\rm r}$ the buildup/leakage times.

Now let us discuss a particular construction [119] of the procedure for nearly-perfect state transfer, assuming that the complex phases of $\mathbf{t}_{\rm e}$ and $\mathbf{t}_{\rm r}$ are constant in time, there is no detuning, $\omega_{\rm e} = \omega_{\rm r} = \omega_0$, and there is no dissipative loss, $T_{1,{\rm e}}^{-1} = T_{1,{\rm r}}^{-1} = 0$, $\eta_{\rm tl} = 1$. (For the experimental coupler discussed in Appendix B, $\mathbf{t}_{\rm e}$ and $\mathbf{t}_{\rm r}$ are mostly imaginary, but also have a significant real component.) As mentioned above, during the first part of the procedure, the receiving resonator is maximally coupled, $\mathbf{t}_{\rm r}(t) = \mathbf{t}_{\rm r,max}$, with this value being determined by experimental limitations. Then a complete cancellation of the back-reflection, $F = 0$, would be possible if $A(t) = A_0 \exp(t/2\tau_{\rm r})$ and $B(t) = B_0 \exp(t/2\tau_{\rm r})$ with $B_0 = \sqrt{\tau_{\rm r}}\, A_0 \mathbf{t}_{\rm r,max}/|\mathbf{t}_{\rm r,max}|$. This is simple to see from Eqs. (5.2) and (5.14), and even simpler to see using the time reversal symmetry: the absence of the back-reflection will then correspond to a leaking resonator without an incident field. This is why in the reversed-time picture $B \propto \exp(-t/2\tau_{\rm r})$, and therefore in the forward-time picture $B \propto \exp(t/2\tau_{\rm r})$; the same argument applies to A.

Thus, we wish to generate an exponentially increasing transmitted field

$$A(t) = A_0 \exp(t/2\tau_{\rm r}), \ \ 0 \le t \le t_{\rm m}, \tag{5.16}$$

during the first half of the procedure (until the mid-time $t_{\rm m}$) by increasing the emitting coupling $\mathbf{t}_{\rm e}(t)$. This would provide the perfect cancellation of reflection if $B(0) = B_0$ (as in the above example), while in the actual case when $B(0) = 0$ we can still use the waveform (5.16), just "pretending" that $B(0) = B_0$. It is easy to see that this provides an almost perfect cancellation. Let us view the initially empty resonator as a linear combination: $B(0) = B_0 - B_0$. Then due to linearity of the evolution, the part B_0 will lead to perfect cancellation as in the above example, while the part $-B_0$ will leak through the coupler and will be lost. If $-B_0$ is fully lost during a sufficiently long procedure, then the corresponding contribution to the inefficiency (mostly from the initial part of the procedure) is $1 - \eta_{\rm r} = |B_0/G(0)|^2$. In particular, for a symmetric procedure ($\tau_{\rm e} = \tau_{\rm r} = \tau$, $t_{\rm m} = t_{\rm f}/2$) approximately one half of the energy will be transmitted during the first half of the procedure, $|B(t_{\rm m})|^2 \approx |G(0)|^2/2$; then $|B_0|^2 \approx \exp(-t_{\rm m}/\tau)\, |G(0)|^2/2$, and therefore the inefficiency contribution is $1 - \eta_{\rm r} \approx \exp(-t_{\rm m}/\tau)/2$. As we see, the *inefficiency decreases exponentially* with the procedure duration.

At time $t_{\rm m}$ the increasing emitting coupling $\mathbf{t}_{\rm e}$ reaches its maximum value $\mathbf{t}_{\rm e,max}$ (determined by experimental limitations), and after that we can continue cancellation of the back-reflection (5.14) by decreasing the receiving coupling $\mathbf{t}_{\rm r}(t)$, while keeping emitting coupling at $\mathbf{t}_{\rm e,max}$. Then the transmitted field $A(t)$ will become exponentially decreasing,

$$A(t) = A_0 \exp(t_\mathrm{m}/2\tau_\mathrm{r}) \exp[-(t-t_\mathrm{m})/2\tau_\mathrm{e}], \;\; t_\mathrm{m} \le t \le t_\mathrm{f}, \tag{5.17}$$

and $\mathbf{t}_\mathrm{r}$ should be varied correspondingly, so that $\kappa_\mathrm{r}(t) = |A(t)|^2/|B(t)|^2$. As mentioned above, the phase conditions for the destructive interference are satisfied automatically in the absence of detuning and for fixed complex phases of $\mathbf{t}_\mathrm{e}(t)$ and $\mathbf{t}_\mathrm{r}(t)$. The procedure is stopped at time t_f, after which $\mathbf{t}_\mathrm{r}(t) = 0$, so that the receiving resonator field $B(t_\mathrm{f})$ no longer changes. When the procedure is stopped at time t_f, there is still some field $G(t_\mathrm{f})$ remaining in the emitting resonator. This leads to the inefficiency contribution $1 - \eta_\mathrm{e} = |G(t_\mathrm{f})/G(0)|^2$. Again assuming a symmetric procedure ($\tau_\mathrm{e} = \tau_\mathrm{r} = \tau$, $t_\mathrm{f} = 2t_\mathrm{m}$), we can use $|B(t_\mathrm{m})|^2 \approx |B(0)|^2/2$; then $|B(t_\mathrm{f})|^2 \approx \exp(-t_\mathrm{m}/\tau)|B(0)|^2/2$ and therefore $1-\eta_\mathrm{e} = \exp(-t_\mathrm{m}/\tau)/2$. Combining the two (equal) contributions to the inefficiency, we obtain [119]

$$1 - \eta \approx \exp(-t_\mathrm{f}/2\tau). \tag{5.18}$$

The numerical accuracy of this formula is very high when $t_\mathrm{f} \gtrsim 10\tau$.

Now let us derive the time dependence of the couplings $\mathbf{t}_\mathrm{e}(t)$ and $\mathbf{t}_\mathrm{r}(t)$ needed for this almost perfect state transfer (we assume that τ_e and τ_r can in general be different). Again, the idea of the construction is to arrange *exact cancelation of the back-reflection if there were an initial field* B_0 *in the receiving resonator* (with proper phase). In this hypothetical "pretend" scenario the evolution of the receiving resonator field $\tilde{B}(t)$ is slightly different from $B(t)$ in the actual case

$[B(0) = 0,\ \tilde{B}(0) = B_0]$, while the fields $G(t)$ and $A(t)$ do not change. Thus, we consider the easy-to-analyze ideal "pretend" scenario $\tilde{B}(t)$ and then relate it to the actual evolution $B(t)$. Note that the transmitted field $A(t)$ is given by Eqs. (5.16) and (5.17): it is exponentially increasing until $t_{\rm m}$ and exponentially decreasing after $t_{\rm m}$. Also note that our procedure does not involve optimization: the only parameter, which can be varied, is the duration of the procedure, which is determined by the desired efficiency (the only formal optimization will be a symmetric choice of $t_{\rm m}$).

In the first part of the procedure, $t \leq t_{\rm m}$, the receiving coupling is at its maximum, $\mathbf{t}_{\rm r}(t) = \mathbf{t}_{\rm r,max}$, and the emitting coupling can be found as $\mathbf{t}_{\rm e}(t) = \mathbf{t}_{\rm e,max}\sqrt{\tau_{\rm e}}\,|A/G|$ (recall that phase conditions are fixed). Here $A(t)$ is given by Eq. (5.16) and $|G(t)|$ can be found from energy conservation in the "pretend" scenario: $|G(t)|^2 + |B_0 \exp(t/2\tau_{\rm r})|^2 = |G(0)|^2 + |B_0|^2$. Using the relation $|B_0/A_0| = \sqrt{\tau_{\rm r}}$, we find

$$\mathbf{t}_{\rm e}(t) = \mathbf{t}_{\rm e,max}\sqrt{\frac{\tau_{\rm e}}{\tau_{\rm r}}}\,\frac{\exp(t/2\tau_{\rm r})}{\sqrt{|G(0)/B_0|^2 + 1 - \exp(t/\tau_{\rm r})}}. \tag{5.19}$$

Here $|B_0|$ is an arbitrary parameter (related to an arbitrary $|A_0|$), which affects the efficiency and duration of the procedure. The corresponding $G(t)$ and $B(t)$ evolutions are

$$G(t) = G(0)\sqrt{1 - |B_0/G(0)|^2[\exp(t/\tau_{\rm r}) - 1]}, \tag{5.20}$$

$$B(t) = B_0[\exp(t/2\tau_{\rm r}) - \exp(-t/2\tau_{\rm r})]. \tag{5.21}$$

Note that in the "pretend" scenario $\tilde{B}(t) = B_0 \exp(t/2\tau_{\rm r})$, while actually $B(t) =$

$\tilde{B}(t) - B_0 \exp(-t/2\tau_{\rm r})$, where the second term describes the decay of the compensating initial field $-B_0$. The phase of B_0 is determined by the phases of the transmission amplitudes, $\arg(B_0) = \arg[\mathbf{t}_{\rm e,max}\mathbf{t}_{\rm r,max}G(0)]$.

Since $|B_0|$ is related to the mid-time $t_{\rm m}$ via the condition $\mathbf{t}_{\rm e}(t_{\rm m}) = \mathbf{t}_{\rm e,max}$, it is convenient to rewrite Eq. (5.19) in terms of $t_{\rm m}$. Thus, the resonator couplings during the first part of the procedure should be [119]

$$\mathbf{t}_{\rm e}(t) = \frac{\mathbf{t}_{\rm e,max}\sqrt{\tau_{\rm e}/\tau_{\rm r}}}{\sqrt{(1+\tau_{\rm e}/\tau_{\rm r})\exp[(t_{\rm m}-t)/\tau_{\rm r}] - 1}}, \tag{5.22}$$

$$\mathbf{t}_{\rm r}(t) = \mathbf{t}_{\rm r,max}, \quad 0 \le t \le t_{\rm m}. \tag{5.23}$$

Note that the increase of $\mathbf{t}_{\rm e}(t)$ is slightly faster than exponential.

To derive the required $\mathbf{t}_{\rm r}(t)$ during the second part of the procedure, $t \ge t_{\rm m}$, we can use the time reversal of the "pretend" scenario. It will then describe a perfect field absorption by the emitting resonator; therefore, $\mathbf{t}_{\rm r}(t)$ in the reversed (and shifted) time should obey the same Eq. (5.19), but with exchanged indices (e↔r) and $|G(0)/B_0|$ replaced with $|\tilde{B}(t_{\rm f})/G(t_{\rm f})|$. Then by using the condition $\mathbf{t}_{\rm r}(t_{\rm m}) = \mathbf{t}_{\rm r,max}$ we immediately derive the formula similar to Eq. (5.22),

$$\mathbf{t}_{\rm r}(t) = \frac{\mathbf{t}_{\rm r,max}\sqrt{\tau_{\rm r}/\tau_{\rm e}}}{\sqrt{(1+\tau_{\rm r}/\tau_{\rm e})\exp[(t-t_{\rm m})/\tau_{\rm e}] - 1}}, \tag{5.24}$$

$$\mathbf{t}_{\rm e}(t) = \mathbf{t}_{\rm e,max}, \quad t_{\rm m} \le t \le t_{\rm f}. \tag{5.25}$$

It is also easy to derive Eq. (5.24) as $\mathbf{t}_{\rm r}(t) = \mathbf{t}_{\rm r,max}\sqrt{\tau_{\rm r}}\,|A/\tilde{B}|$, with $A(t)$ given by Eq. (5.17) and $|\tilde{B}(t)|^2 = |G(0)|^2 + |B_0|^2 - |G(t)|^2$ given by the energy conservation, where $|G(t)| = \sqrt{\tau_{\rm e}}\,|A(t)|$.

The contribution to the inefficiency due to imperfect reflection (mostly during the initial part of the procedure) is $1-\eta_{\rm r} \approx |B_0/G(0)|^2$ since the reflected field is the leaking initial field $-B_0$ and it is almost fully leaked during the procedure. Comparing Eqs. (5.19) and (5.22), we find $|B_0/G(0)|^2 \approx \exp(-t_{\rm m}/\tau_{\rm r})\,\tau_{\rm r}/(\tau_{\rm e}+\tau_{\rm r})$ assuming $\exp(-t_{\rm m}/\tau_{\rm r}) \ll 1$. The contribution to the inefficiency due to the untransmitted field left in the emitting resonator at the end of procedure is $1-\eta_{\rm e} = |G(t_{\rm f})/G(0)|^2 = (\tau_{\rm e}/\tau_{\rm r})\,|B_0/G(0)|^2 \exp(t_{\rm m}/\tau_{\rm r})\exp[-(t_{\rm f}-t_{\rm m})/\tau_{\rm e}]$, where we used relation $|G(t_{\rm f})|^2 = \tau_{\rm e}|A(t_{\rm f})|^2$. Using the above formula for $|B_0/G(0)|^2$ we obtain $1-\eta_{\rm e} \approx \exp[-(t_{\rm f}-t_{\rm m})/\tau_{\rm e}]\,\tau_{\rm e}/(\tau_{\rm e}+\tau_{\rm r})$. Combining both contributions to the inefficiency we find [119]

$$1-\eta \approx \frac{\tau_{\rm r}\exp(-t_{\rm m}/\tau_{\rm r}) + \tau_{\rm e}\exp[-(t_{\rm f}-t_{\rm m})/\tau_{\rm r}]}{\tau_{\rm e}+\tau_{\rm r}}. \tag{5.26}$$

Minimization of this inefficiency over $t_{\rm m}$ for a fixed total duration $t_{\rm f}$ gives the condition

$$t_{\rm m}/\tau_{\rm r} = (t_{\rm f}-t_{\rm m})/\tau_{\rm e} \tag{5.27}$$

and the final result for the inefficiency [119],

$$1-\eta \approx \exp\left(-\frac{t_{\rm f}}{\tau_{\rm e}+\tau_{\rm r}}\right), \tag{5.28}$$

which generalizes Eq. (5.18).

The required ON/OFF ratios for the couplers can be found from Eqs. (5.22) and (5.24),

$$\frac{\mathbf{t}_{\rm e,max}}{\mathbf{t}_{\rm e}(0)} \approx \sqrt{\frac{\tau_{\rm e}+\tau_{\rm r}}{\tau_{\rm e}} \exp\left(\frac{t_{\rm m}}{\tau_{\rm r}}\right)}, \tag{5.29}$$

$$\frac{\mathbf{t}_{\rm r,max}}{\mathbf{t}_{\rm r}(t_{\rm f})} \approx \sqrt{\frac{\tau_{\rm e}+\tau_{\rm r}}{\tau_{\rm r}} \exp\left(\frac{t_{\rm f}-t_{\rm m}}{\tau_{\rm r}}\right)}, \tag{5.30}$$

which in the optimized case corresponding to Eq. (5.28) become

$$\frac{\mathbf{t}_{\rm e,max}}{\mathbf{t}_{\rm e}(0)} \approx \sqrt{\frac{1+\tau_{\rm r}/\tau_{\rm e}}{1-\eta}}, \;\; \frac{\mathbf{t}_{\rm r,max}}{\mathbf{t}_{\rm r}(t_{\rm f})} \approx \sqrt{\frac{1+\tau_{\rm e}/\tau_{\rm r}}{1-\eta}}. \tag{5.31}$$

Note that using two tunable couplers is crucial for our protocol. If only one tunable coupler is used as in Ref. [118], then the procedure becomes much longer and requires a much larger ON/OFF ratio. Assuming a fixed receiving coupling, we can still use Eqs. (5.19)–(5.21) for the analysis and obtain the following result. If the coupling of the emitting resonator is limited by a maximum value $\kappa_{\rm max}$ of the leakage rate, then the shortest duration of the procedure with efficiency η is $t_{\rm f} = LN/[\kappa_{\rm max}(1-\eta)]$, where $LN \approx \ln \frac{e\ln[(e/(1-\eta)]}{1-\eta}$. For typical values of η we get $LN \approx 3+\ln[1/(1-\eta)]$, and therefore the shortest duration for a procedure with one tunable coupler is $t_{\rm f} \approx (1-\eta)^{-1}\kappa_{\rm max}^{-1}\{3+\ln[1/(1-\eta)]\}$. This is more than a factor $(1-\eta)^{-1}/2$ longer than the duration $t_{\rm f} = 2\,\kappa_{\rm max}^{-1}\ln[1/(1-\eta)]$ of our procedure with two tunable couplers [see Eq. (5.18)]. The optimum (fixed) receiving coupling is $\kappa_{\rm r} = (1-\eta)\kappa_{\rm max}/(1+1/LN)$, which makes clear why the procedure is so long. The corresponding ON/OFF ratio for the emitting coupler is $\mathbf{t}_{\rm e,max}/\mathbf{t}_{\rm e}(0) = \sqrt{\kappa_{\rm max}/\kappa_{\rm min}} = (1-\eta)^{-1}\sqrt{LN/(1-2/LN)} \approx (1-\eta)^{-1}\sqrt{3+\ln[1/(1-\eta)]}$. This is more than a factor $(1-\eta)^{-1/2}$ larger than what is needed for our procedure [see Eq. (5.31)].

Note that we use the exponentially increasing and then exponentially decreasing transmitted field $A(t)$ [Eqs. (5.16) and (5.17)] because we wish to vary only one coupling in each half of the procedure and to minimize the duration of the procedure. In general, any "reasonable" shape $A(t)$ can be used in our procedure. Assuming for simplicity a real positive $A(t)$, we see that a "reasonable" $A(t)$ should satisfy the inequality $A^2(t) \leq \kappa_{\rm e,max}[|G(0)|^2 - \int_0^t A^2(t')\,dt']$, so that it can be produced by using $\kappa_{\rm e}(t) = A^2(t)/[|G(0)|^2 - \int_0^t A^2(t')\,dt']$ without exceeding the maximum emitting coupling $\kappa_{\rm e,max}$. We also assume that a "reasonable" $A(t)$ does not increase too fast, $dA(t)/dt \leq (\kappa_{\rm r,max}/2)A(t)$, or at least satisfies a weaker inequality $A(t) \leq \sqrt{\kappa_{\rm r,max}}\sqrt{\kappa_{\rm r,max}^{-1}A^2(0) + \int_0^t A^2(t')\,dt'}$. In this case we can apply the "pretend" method, which gives $\kappa_{\rm r}(t) = A^2(t)/[\kappa_{\rm r,max}^{-1}A^2(0) + \int_0^t A^2(t')\,dt']$, not exceeding the maximum receiving coupling $\kappa_{\rm r,max}$. This leads to the inefficiency contribution $1-\eta_{\rm e} = 1 - \int_0^{t_{\rm f}} A^2(t')\,dt'/|G(0)|^2$ due to the untransmitted field and inefficiency contribution $1-\eta_{\rm r} = \kappa_{\rm r,max}^{-1}A^2(0)/|G(0)|^2$ due to the back-reflection. We see that for high efficiency we need a small $A(t)$ at the beginning and at the end of the procedure. Even though we do not have a rigorous proof, it is intuitively obvious that our procedure considered in this section is optimal (or nearly optimal) for minimizing the duration of the protocol for a fixed efficiency and fixed maximum couplings (see also the proof of optimality for a similar, but single-sided procedure in Ref. [118]). We think that it is most natural to design an experiment exactly as described in this section [using Eqs. (5.16) and (5.17) and varying only one coupling at a time]; however, a minor or moderate time-dependent tuning of the other coupling (which is assumed to be fixed in our protocol) can be useful in experimental optimization of the procedure.

In this section, we considered the ideal transfer protocol, assuming that the transmission amplitudes are given exactly by Eqs. (5.22)–(5.25), and also assuming equal resonator frequencies, fixed phases of the transmission amplitudes, and absence of extra loss ($T_{1,\mathrm{e}}^{-1} = T_{1,\mathrm{r}}^{-1} = 0$, $\eta_{\mathrm{tl}} = 1$). In the following sections we will discuss the effect of various imperfections on the efficiency of the transfer protocol.

5.3 Imperfect pulse shapes

The high efficiency of the state transfer analyzed in the previous section relies on precise calibration and control of experimental parameters, so that the needed pulse shapes (5.22)–(5.25) for the transmission amplitudes $\mathbf{t}_{\mathrm{e}}(t)$ and $\mathbf{t}_{\mathrm{r}}(t)$ are accurately implemented. However, in a real experiment there will always be some imperfections in the pulse shapes. In this section we analyze the robustness of the transfer efficiency to the pulse shape imperfections, still assuming fixed phases and the absence of detuning and dissipative loss. In particular, we will vary several parameters used in the pulse shapes (5.22)–(5.25): the maximum transmission amplitudes $|\mathbf{t}_{\mathrm{e(r),max}}|$, the buildup/leakage times $\tau_{\mathrm{e(r)}}$, and the mid-time t_{m}. By varying these parameters we imitate imperfect experimental calibrations, so that the actual parameters of the pulse shapes are different from the designed ones. We also consider distortion ("warping") of the pulse shapes imitating a nonlinear transfer function between the control pulses and amplitudes $\mathbf{t}_{\rm e(r)}$. Imperfections due to Gaussian filtering of the pulse shapes, additional noise, and dissipative losses will also be discussed.

We analyze the effect of imperfections using numerical integration of the evolution equations (5.1)–(5.3). As the ideally designed procedure we choose Eqs. (5.22)–(5.25) with $|\mathbf{t}_{\rm e,max}| = |\mathbf{t}_{\rm r,max}| = 0.05$, assuming the quarter-wavelength resonators with frequency $\omega_{\rm e}/2\pi = \omega_{\rm r}/2\pi = 6$ GHz, so that the round-trip time is $\tau_{\rm rt,e} = \tau_{\rm rt,r} = \pi/\omega_{\rm e(r)} = 1/12$ ns and the buildup/leakage time is $\tau_{\rm e} = \tau_{\rm r} = \tau = 33.3$ ns. The duration of the procedure $t_{\rm f}$ is chosen from Eq. (5.28), using two design values of the efficiency: $\eta_{\rm d} = 0.99$ and $\eta_{\rm d} = 0.999$; the corresponding durations are $t_{\rm f} = 307.0$ ns and 460.5 ns. The time $t_{\rm m}$ is in the middle of the procedure: $t_{\rm m} = t_{\rm f}/2$. In the simulations we use $G(0) = 1$, $B(0) = 0$, and calculate the efficiency as $\eta = |B(t_{\rm f})/G(0)|^2$. Note that the values of $|\mathbf{t}_{\rm e(r),max}|$ and $\omega_{\rm e(r)}$ affect the duration of the procedure, but do not affect the results for the efficiency presented in this section (except for the filtering effect).

5.3.1 Variation of maximum transmission amplitudes $\mathbf{t}_{\rm e,max}$ and $\mathbf{t}_{\rm r,max}$

Let us assume that the transmission amplitudes are still described by the pulse shapes (5.22)–(5.25), but with slightly different parameters,

$$\mathbf{t}_{\rm e}^{\rm a}(t) = \frac{\mathbf{t}_{\rm e,max}^{\rm a}\sqrt{\tau_{\rm e}^{\rm a}/\tau_{\rm r}^{\rm a}}}{\sqrt{(1+\tau_{\rm e}^{\rm a}/\tau_{\rm r}^{\rm a})\exp[(t_{\rm m}^{\rm a,e}-t)/\tau_{\rm r}^{\rm a}]-1}}, \quad t \leq t_{\rm m}^{\rm a,e}, \tag{5.32}$$

$$\mathbf{t}_{\rm r}^{\rm a}(t) = \frac{\mathbf{t}_{\rm r,max}^{\rm a}\sqrt{\tau_{\rm r}^{\rm a}/\tau_{\rm e}^{\rm a}}}{\sqrt{(1+\tau_{\rm r}^{\rm a}/\tau_{\rm e}^{\rm a})\exp[(t-t_{\rm m}^{\rm a,r})/\tau_{\rm e}^{\rm a}]-1}}, \quad t \geq t_{\rm m}^{\rm a,r}, \tag{5.33}$$

so that the "actual" parameters $\mathbf{t}_{\rm e,max}^{\rm a}$, $\mathbf{t}_{\rm r,max}^{\rm a}$, $\tau_{\rm e}^{\rm a}$, $\tau_{\rm r}^{\rm a}$, $t_{\rm m}^{\rm a,e}$, and $t_{\rm m}^{\rm a,r}$ are somewhat different from their design values $\mathbf{t}_{\rm e,max}$, $\mathbf{t}_{\rm r,max}$, $\tau_{\rm e}$, $\tau_{\rm r}$, and $t_{\rm m}$. The transmission amplitudes are kept at their maxima $\mathbf{t}_{\rm e,max}^{\rm a}$ and $\mathbf{t}_{\rm r,max}^{\rm a}$ after/before the possibly different mid-times $t_{\rm m}^{\rm a,e}$ and $t_{\rm m}^{\rm a,r}$. We will analyze the effect of inaccurate parameters one by one.

First, we assume that only the maximum amplitudes are inaccurate, $\mathbf{t}_{\rm e,max}^{\rm a} = \mathbf{t}_{\rm e,max} + \delta\mathbf{t}_{\rm e,max}$ and $\mathbf{t}_{\rm r,max}^{\rm a} = \mathbf{t}_{\rm r,max} + \delta\mathbf{t}_{\rm r,max}$, while other parameters are equal to their design values. (We change only the absolute values of $\mathbf{t}_{\rm e,max}$ and $\mathbf{t}_{\rm r,max}$, because their phases affect only the correctable final phase $\varphi_{\rm f}$ but do not affect the efficiency η.) In Fig. 5.3 we show the numerically calculated inefficiency $1-\eta$ of the state transfer as a function of the variation in maximum transmission amplitude $\delta\mathbf{t}_{\rm max}/\mathbf{t}_{\rm max}$, with the solid lines corresponding to variation of only one maximum amplitude, $\delta\mathbf{t}_{\rm e,max}/\mathbf{t}_{\rm e,max}$ or $\delta\mathbf{t}_{\rm r,max}/\mathbf{t}_{\rm r,max}$ (the results are the same), and the dashed lines corresponding to variation of both of them, $\delta\mathbf{t}_{\rm e,max}/\mathbf{t}_{\rm e,max} =$

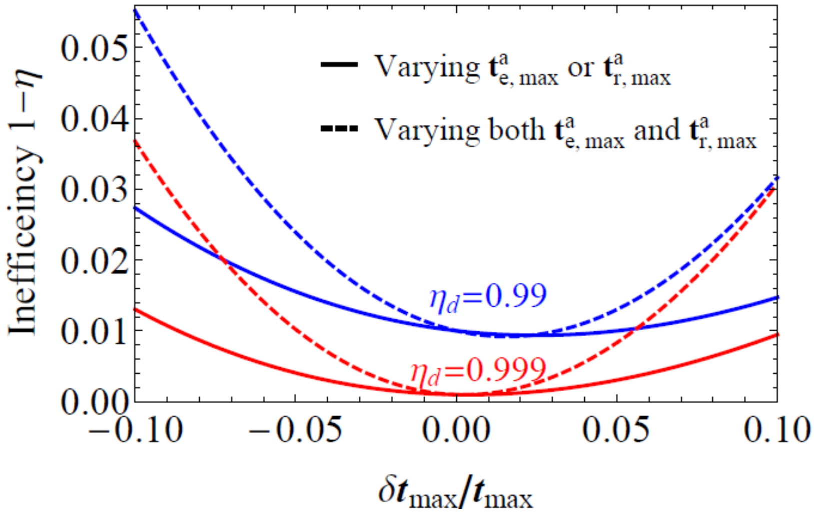

Figure 5.3: Inefficiency $1-\eta$ of the state transfer procedure as a function of relative variation of the maximum transmission amplitudes $\delta\mathbf{t}_{\rm max}/\mathbf{t}_{\rm max} = (\mathbf{t}^{\rm a}_{\rm e(r),max} - \mathbf{t}_{\rm e(r),max})/\mathbf{t}_{\rm e(r),max}$ for design efficiencies $\eta_{\rm d} = 0.99$ (blue curves) and 0.999 (red curves). The maximum transmission amplitudes $\mathbf{t}_{\rm e,max}$ and $\mathbf{t}_{\rm r,max}$ are either varied simultaneously (dashed curves) or one of them is kept at the design value (solid curves). The superscript "a" indicates an "actual" value, different from the design value.

$\delta\mathbf{t}_{\rm r,max}/\mathbf{t}_{\rm r,max}$. The blue (upper) lines are for the case of design efficiency $\eta_{\rm d} = 0.99$ and the red (lower) lines are for $\eta_{\rm d} = 0.999$.

We see that deviations of the actual maximum amplitudes $\mathbf{t}^{\rm a}_{\rm e,max}$ and $\mathbf{t}^{\rm a}_{\rm r,max}$ from their design values $\mathbf{t}_{\rm e,max}$ and $\mathbf{t}_{\rm r,max}$ increase the inefficiency of the state transfer [essentially because of the inconsistency between $\mathbf{t}^{\rm a}_{\rm e(r),max}$ and $\tau^{\rm a}_{\rm e(r)}$]. However, the effect is not very significant, with the additional inefficiency of less than 0.006 when one of the parameters deviates by ±5% and less than 0.02 when both of them deviate by ±5%. The curves in Fig. 5.3 are approximately parabolic, with a growing asymmetry for larger $1-\eta_{\rm d}$.

For the case $\eta_{\rm d} \approx 1$ the numerical results for the additional inefficiency $-\delta\eta = \eta_{\rm d} - \eta$ can be approximately fitted by the formula

$$-\delta\eta \approx \left(\frac{\delta \mathbf{t}_{\rm e,max}}{\mathbf{t}_{\rm e,max}}\right)^2 + \left(\frac{\delta \mathbf{t}_{\rm r,max}}{\mathbf{t}_{\rm r,max}}\right)^2 + 1.25 \frac{\delta \mathbf{t}_{\rm e,max}}{\mathbf{t}_{\rm e,max}} \frac{\delta \mathbf{t}_{\rm r,max}}{\mathbf{t}_{\rm r,max}}, \tag{5.34}$$

which we obtained by changing the maximum amplitudes symmetrically, anti-symmetrically, and separately. Note that in the ideal procedure we assumed $|\mathbf{t}_{\rm e,max}| = |\mathbf{t}_{\rm r,max}|$.

The main result here is that the state transfer is quite robust against the small variation of the transmission amplitudes. We expect that experimentally these parameters can be calibrated with accuracy of a few per cent or better; the related inefficiency of the transfer protocol is very small.

5.3.2 Variation of buildup/leakage times $\tau_{\rm e}$ and $\tau_{\rm r}$

Now let us assume that in Eqs. (5.32) and (5.33) only the buildup/leakage time parameters are slightly inaccurate, $\tau_{\rm e}^{\rm a} = \tau + \delta\tau_{\rm e}$ and $\tau_{\rm r}^{\rm a} = \tau + \delta\tau_{\rm r}$ (we assume that in the ideal procedure $\tau_{\rm e} = \tau_{\rm r} = \tau$), while other parameters are equal to their design values. The transfer inefficiency as a function of the relative deviations $\delta\tau_{\rm e(r)}/\tau$ is shown in Fig. 5.4 for the design efficiencies $\eta_{\rm d} = 0.99$ (blue lines) and 0.999 (red lines). For the solid lines only one of the buildup/leakage times is varied (the results coincide), while for the dashed lines both parameters are varied together, $\delta\tau_{\rm e} = \delta\tau_{\rm r}$. As we see, $\pm 5\%$ variation of one of the buidup/leakage times increases

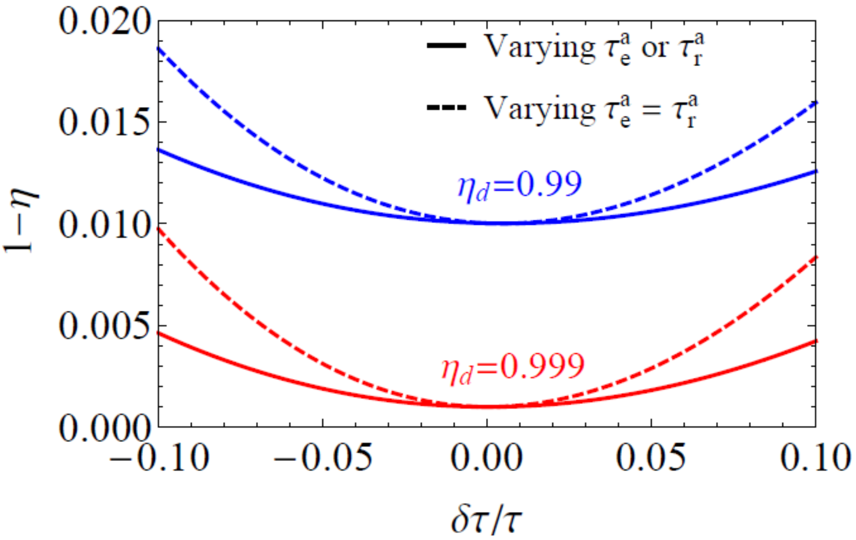

Figure 5.4: Dependence of the inefficiency $1 - \eta$ on relative variation of the buildup/leakage time $\delta\tau_{\mathrm{e(r)}}/\tau = (\tau^{\mathrm{a}}_{\mathrm{e(r)}} - \tau)/\tau$ for design efficiencies $\eta_{\mathrm{d}} = 0.99$ (blue curves) and 0.999 (red curves), assuming $\tau_{\mathrm{e}} = \tau_{\mathrm{r}} = \tau$. The buildup/leakage times $\tau^{\mathrm{a}}_{\mathrm{e}}$ and $\tau^{\mathrm{a}}_{\mathrm{r}}$ are varied either simultaneously (dashed curves) or one of them is kept at the design value (solid curves).

the inefficiency by less than 0.001, and by less than 0.0025 if both the times are varied by ±5%.

The approximately parabolic dependences shown in Fig. 5.4 can be numerically fitted by the formula for the additional inefficiency $-\delta\eta$,

$$-\delta\eta \approx 0.34 \left[\left(\frac{\delta\tau_{\mathrm{e}}}{\tau} \right)^2 + \left(\frac{\delta\tau_{\mathrm{r}}}{\tau} \right)^2 \right] + 0.12 \frac{\delta\tau_{\mathrm{e}}}{\tau} \frac{\delta\tau_{\mathrm{r}}}{\tau}, \tag{5.35}$$

which was again obtained by varying $\delta\tau_{\mathrm{e}}$ and $\delta\tau_{\mathrm{r}}$ symmetrically, antisymmetrically, and separately. Most importantly, we see that the transfer procedure is robust against small deviations of the buildup/leakage times. (In an experiment we expect not more than a few per cent inaccuracy for these parameters.)

5.3.3 Variation of mid-times $t_{\rm m}^{\rm a,e}$ and $t_{\rm m}^{\rm a,r}$

Ideally, the pulse shapes $\mathbf{t}_{\rm e}(t)$ and $\mathbf{t}_{\rm r}(t)$ should switch from increasing/decreasing parts to constants at the same time $t_{\rm m}$, exactly in the middle of the procedure. However, due to imperfectly calibrated delays in the lines delivering the signals to the couplers, this change may occur at slightly different actual times $t_{\rm m}^{\rm a,e}$ and $t_{\rm m}^{\rm a,r}$, which are also not necessarily exactly in the middle of the procedure. Let us assume that $\mathbf{t}_{\rm e}(t)$ and $\mathbf{t}_{\rm r}(t)$ are given by Eqs. (5.32) and (5.33) with slightly inaccurate times $t_{\rm m}^{\rm a,e}$ and $t_{\rm m}^{\rm a,r}$, while other parameters are equal to their design values.

Solid lines in Fig. 5.5 show the dependence of the transfer inefficiency $1-\eta$ on the shift of the mid-time $\delta t_{\rm m}^{\rm r} = t_{\rm m}^{\rm a,r} - t_{\rm m}$, which is normalized by the buildup/leakage time τ. Blue and red lines are for the design efficiencies $\eta_{\rm d} = 0.99$ and 0.999, respectively. The case when only $t_{\rm m}^{\rm a,e}$ is changed is similar to what is shown by the solid lines up to the mirror symmetry, $\delta t_{\rm m}^{\rm r} \leftrightarrow -\delta t_{\rm m}^{\rm e}$. The dashed lines show the case when both mid-times are shifted simultaneously, $t_{\rm m}^{\rm a,e} = t_{\rm m}^{\rm a,r}$.

We see that when $t_{\rm m}^{\rm a,e}$ and $t_{\rm m}^{\rm a,r}$ coincide, there is practically no effect of the shift. This is because in this case the change is only due to slightly unequal durations $t_{\rm m}^{\rm a}$ and $t_{\rm f} - t_{\rm m}^{\rm a}$. A non-zero time mismatch $t_{\rm m}^{\rm a,e} - t_{\rm m}^{\rm a,r}$ has a much more serious effect because the reflection cancellation (5.13) becomes significantly degraded in the middle of the procedure, where the propagating field is at its maximum.

The numerical fit to a quadratic dependence gives

$$-\delta\eta \approx 0.25 \left(\frac{\delta t_{\rm m}^{\rm a,e} - \delta t_{\rm m}^{\rm a,r}}{\tau} \right)^2 . \tag{5.36}$$

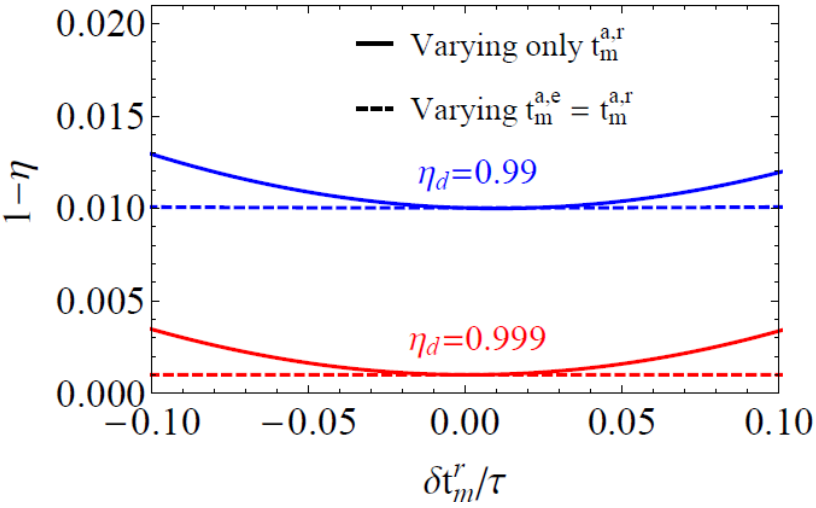

Figure 5.5: Inefficiency $1 - \eta$ as a function of the mid-time shift $\delta t_{\mathrm{m}}^{\mathrm{r}} = t_{\mathrm{m}}^{\mathrm{a,r}} - t_{\mathrm{m}}$ normalized by the buildup/leakage time τ. The mid-time $t_{\mathrm{m}}^{\mathrm{a,e}}$ is either varied equally (dashed curves) or kept constant (solid curves). The results for varying only $t_{\mathrm{m}}^{\mathrm{a,e}}$ are the same as the solid curves up to the sign change, $\delta t_{\mathrm{m}}^{\mathrm{r}} \leftrightarrow -\delta t_{\mathrm{m}}^{\mathrm{e}}$.

For $\tau = 33.3$ ns this means that $\sim$3 ns time mismatch leads to only 2×10^{-3} increase in inefficiency. Such robustness to the time mismatch is rather surprising. It can be qualitatively explained in the following way. The relative imperfection of the back-reflection cancellation (5.13) is approximately $(\delta t_{\mathrm{m}}^{\mathrm{a,e}} - \delta t_{\mathrm{m}}^{\mathrm{a,r}})/\tau$ in the middle of the procedure; however, the lost energy of the back-reflected field scales quadratically. Therefore, we can explain Eq. (5.36) up to a numerical factor. In an experiment we expect that the time mismatch can be made smaller than 1 ns; the corresponding inefficiency is almost negligible.

5.3.4 Pulse-shape warping

As another possible imperfection of the ideal time-dependences $\mathbf{t}_{\rm e}(t)$ and $\mathbf{t}_{\rm r}(t)$, we consider a nonlinear deformation ("warping") with the form

$$\mathbf{t}_j^{\rm a}(t) = \mathbf{t}_j(t)\left[1+\alpha_j\frac{\mathbf{t}_j(t)-\mathbf{t}_{j,\max}}{\mathbf{t}_{j,\max}}\right], \;\; j={\rm e},{\rm r}, \tag{5.37}$$

where $\alpha_{\rm e}$ and $\alpha_{\rm r}$ are the warping parameters, which determine the strength of the deformations. Note that this deformation does not affect maximum values $\mathbf{t}_{\rm e(r),max}$ and the values close to zero; it affects only intermediate values. The deformation imitates nonlinear (imperfectly compensated) conversion from experimental control signals into transmission amplitudes.

The inefficiency increase due to the warping of the transmission amplitude pulse shapes is illustrated in Fig. 5.6. Solid lines show the case when only $\alpha_{\rm e}$ or $\alpha_{\rm r}$ is non-zero (the results coincide), while the dashed lines show the case $\alpha_{\rm e}=\alpha_{\rm r}$. We see that for $\alpha_{\rm e}=\alpha_{\rm r}=0.05$ the inefficiency increases by $\sim 10^{-3}$ for both design efficiencies $\eta_{\rm d}=0.99$ and 0.999. Similar to the variation of other parameters, the inefficiency due to the warping effect has a quadratic dependence on the warping parameters $\alpha_{\rm e}$ and $\alpha_{\rm r}$. The numerical fitting for small $|\alpha_{\rm e(r)}|$ and $\eta\approx 1$ gives

$$-\delta\eta \approx 0.22(\alpha_{\rm e}^2+\alpha_{\rm r}^2)+0.12\alpha_{\rm e}\alpha_{\rm r}. \tag{5.38}$$

Again, this result shows that the state transfer is robust to distortion of the couplers' transmission amplitude pulse shapes. We do not expect that uncompen-

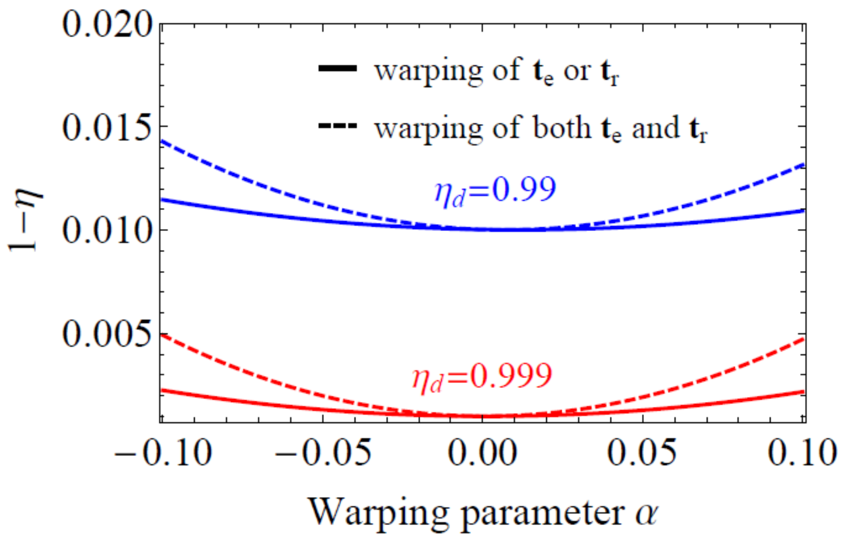

Figure 5.6: Dependence of the inefficiency $1-\eta$ on the warping parameters $\alpha_{\rm e}$ and $\alpha_{\rm r}$, introduced in Eq. (5.37) to describe the pulse shape distortion, for design efficiencies $\eta_{\rm d} = 0.99$ (blue curves) and 0.999 (red curves). The solid curves show the case when only one warping parameter is non-zero (the results coincide); the dashed curves are for the case $\alpha_{\rm e} = \alpha_{\rm r}$.

sated experimental nonlinearities will follow Eq. (5.37) exactly, since this equation only imitates a nonlinear conversion. However, very crudely, we would expect that $|\alpha_{\rm e(r)}| < 0.05$ is a realistic experimental estimate.

5.3.5 Smoothing by a Gaussian filter

In an actual experiment the designed pulse shapes for the transmission amplitudes of the tunable couplers given by Eqs. (5.22)–(5.25) will pass through a filter. Here we convolve the transmission amplitudes with a Gaussian function to simulate the experimental filtering, so the actual transmission amplitudes are

$$\mathbf{t}_j^{\rm a}(t) = \frac{1}{\sqrt{2\pi}\,\sigma} \int_{-\infty}^{\infty} e^{-(t-t')^2/2\sigma^2} \mathbf{t}_j(t')\, dt', \quad j = {\rm e}, {\rm r}, \tag{5.39}$$

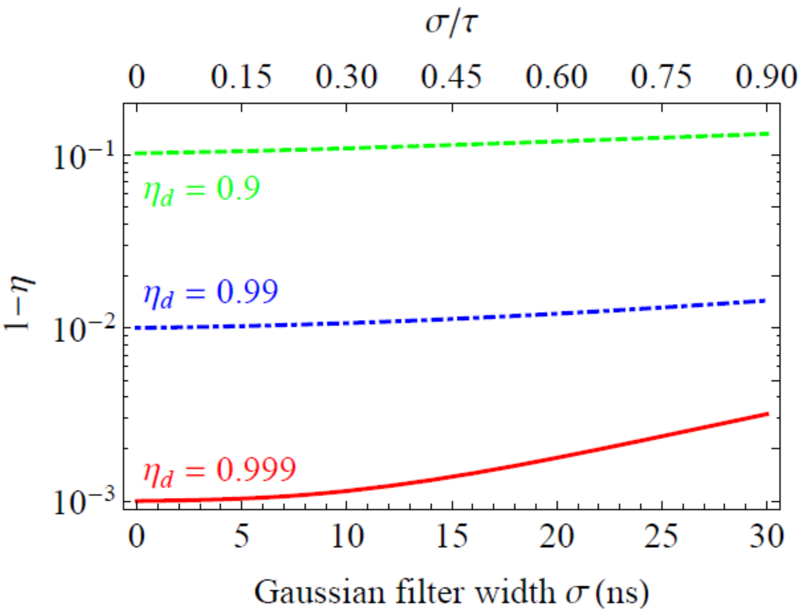

Figure 5.7: Inefficiency $1 - \eta$ as a function of the width of a Gaussian filter σ (in ns) for design efficiencies $\eta_{\rm d} = 0.9$ (green dashed curve), 0.99 (blue dot-dashed curve), and 0.999 (red solid curve). We use $\tau = 33.3\,$ns, as in Fig. 5.2. The upper horizontal axis shows the normalized value σ/τ.

where σ is the time-width of the Gaussian filter. The filtering smooths out the kinks at the middle of the procedure and slightly lowers the initial and final values of $\mathbf{t}_{\rm e}$ and $\mathbf{t}_{\rm r}$. The change in transmission amplitudes translates into a decrease in the state transfer efficiency. Note that the smoothing reduces the energy loss at the beginning and end of the procedure, but causes an increased energy loss at the middle of the procedure, thus increasing the procedure inefficiency overall.

The procedure inefficiency with the effect of the Gaussian filtering of transmission amplitudes is shown in Fig. 5.7 for the design efficiencies $\eta_{\rm d} = 0.9$, 0.99, and 0.999. Rather surprisingly, the effect is very small, so that filtering with $\sigma = 10$ ns does not produce a noticeable increase of the inefficiency, and even with $\sigma = 30$ ns (which is close to the buildup/leakage time) the effect is still small. Such robustness to the filtering can be qualitatively understood in the same way as the robustness to the mismatch between the mid-times $\mathbf{t}_{\mathrm{e}}(t)$ and $\mathbf{t}_{\mathrm{r}}(t)$ discussed above. Note that experimentally [148] σ is on the order of 1 ns, so the effect of the filter on the efficiency should be negligible.

5.3.6 Noisy transmission amplitudes

In experiment the pulse shapes $\mathbf{t}_{\mathrm{e}}(t)$ and $\mathbf{t}_{\mathrm{r}}(t)$ may contain noise. We model this noise by replacing the designed pulse shapes $\mathbf{t}_{\mathrm{e}}(t)$ and $\mathbf{t}_{\mathrm{r}}(t)$ with "actual" shapes as

$$\mathbf{t}_j^{\mathrm{a}}(t) = \mathbf{t}_j(t)[1 + a\,\xi_j(t)], \;\; j = \mathrm{e},\, \mathrm{r}, \tag{5.40}$$

where a corresponds to the dimensionless noise amplitude and $\xi_{\mathrm{e}}(t)$ and $\xi_{\mathrm{r}}(t)$ are mutually uncorrelated random processes. We generate each $\xi(t)$ numerically in the following way. First, we choose a time step dt and generate $\xi(t)$ at discrete time moments $t = n\,dt$ (with integer n) as Gaussian-distributed random numbers with zero mean and unit standard deviation. After that we create a smooth function $\xi(t)$ passing through these points by polynomial interpolation. Since the noise contribution in Eq. (5.40) scales with the transmission amplitude $\mathbf{t}_j$, we call it a multiplicative noise. Besides that, we also use a model of an additive noise defined as

$$\mathbf{t}_j^{\mathrm{a}}(t) = \mathbf{t}_j(t) + a\,\mathbf{t}_{j,\max}\,\xi_j(t), \;\; j = \mathrm{e}, \mathrm{r}, \tag{5.41}$$

where the relative amplitude a is now compared with the maximum value $\mathbf{t}_{j,\max}$, while each $\xi(t)$ is generated in the same way. Note that for sufficiently small dt

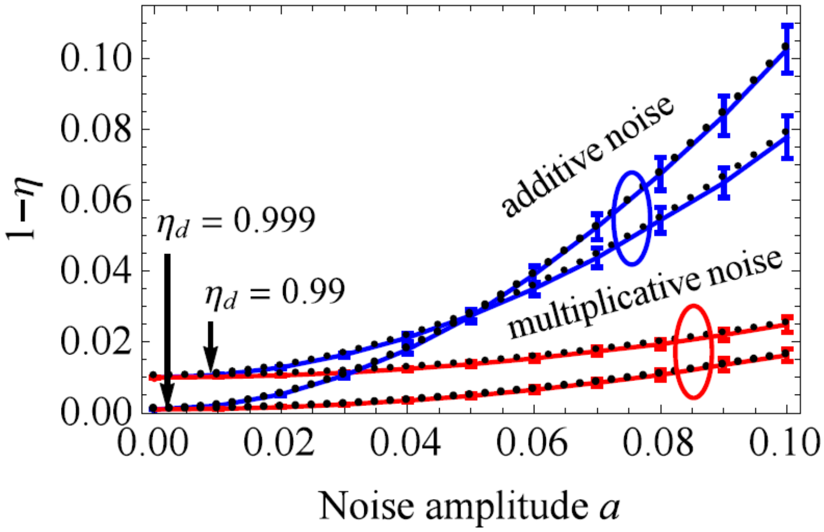

Figure 5.8: Solid lines: inefficiency $1 - \eta$ averaged over 100 random noise realizations, as a function of the dimensionless noise amplitude a, for the multiplicative noise (red lines, bottom), Eq. (5.40), and the additive noise (blue lines, top), Eq. (5.41); both with $\overline{\xi^2} = 0.78$. The error bars show the standard deviation for some values of a. The results are shown for $\eta_{\rm d} = 0.99$ and 0.999. In the simulation we used the time step $dt = 1\,{\rm ns}$ and parameters of the procedure in Fig. 5.2 ($\tau = 33.3\,{\rm ns}$). Black dotted lines (practically coinciding with the solid lines) are calculated by replacing the noise with the effective increase of the leakage rates $\kappa_{\rm e(r)}$ (see text).

the noise $\xi(t)$ is practically white at low frequency; its variance $\overline{\xi^2}$ does not depend on dt, and therefore the low frequency spectral density is proportional to dt (the effective cutoff frequency scales as dt^{-1}). Also note that the variance $\overline{\xi^2}$ somewhat depends on the method of interpolation used to generate $\xi(t)$. For the default interpolation method in Mathematica, which we used (polynomial interpolation of order three), $\overline{\xi^2} \approx 0.78$.

The numerical results for the transfer inefficiency $1-\eta$ in the presence of noise are shown in Fig. 5.8 as a function of the dimensionless amplitude a. We used the time step $dt = 1$ ns and design efficiencies $\eta_{\rm d} = 0.99$ and $\eta_{\rm d} = 0.999$. The results are averaged over 100 random realizations; we show the average values by the solid lines and also show the standard deviations at some values of a. Red lines correspond to the multiplicative noise, while blue lines correspond to the additive noise. As expected, the additive noise leads to larger inefficiency than the multiplicative noise with the same amplitude, because of larger noise at the non-constant part of the pulse shape.

It is somewhat surprising that, as we checked numerically, the average results shown in Fig. 5.8 by the solid lines practically do not depend on the choice of the time step dt, as long as $dt \ll \tau_{\rm e(r)}$ (even though in our simulations dt affects the noise spectral density). The error bars, however, scale with dt as $\sqrt{dt}$. This behavior can be understood in the following way. In the evolution equations (5.1)–(5.3), the noise in $\mathbf{t}_{\rm e}(t)$ and $\mathbf{t}_{\rm r}(t)$ affects the leakage rates $\kappa_{\rm e} \propto |\mathbf{t}_{\rm e}|^2$ and $\kappa_{\rm r} \propto |\mathbf{t}_{\rm r}|^2$ of the two resonators, and also affects the transfer term $\sqrt{\kappa_{\rm e}\kappa_{\rm r}}\, A \propto |\mathbf{t}_{\rm e}\mathbf{t}_{\rm r}|$. On average the transfer term does not change (because the noises of $\mathbf{t}_{\rm e}(t)$ and $\mathbf{t}_{\rm r}(t)$ are uncorrelated); however, the average values of $|\mathbf{t}_{\rm e}|^2$ and $|\mathbf{t}_{\rm r}|^2$ change as $\langle|\mathbf{t}^{\rm a}_{\rm e(r)}|^2\rangle = |\mathbf{t}_{\rm e(r)}|^2(1+a^2\,\overline{\xi^2})$ for the model of Eq. (5.40) and as $\langle|\mathbf{t}^{\rm a}_{\rm e(r)}|^2\rangle = |\mathbf{t}_{\rm e(r)}|^2 + a^2\,|\mathbf{t}_{\rm e(r),max}|^2\,\overline{\xi^2}$ for the model of Eq. (5.41). Therefore, on average we expect dependence on $a^2\,\overline{\xi^2}$ (a second-order effect), but no dependence on dt, as long as it is sufficiently small. In contrast, the error bars in Fig. 5.8 should depend on dt because the transfer term $\sqrt{\kappa_{\rm e}\kappa_{\rm r}}\, A$ fluctuates linearly in ξ. Since the low-frequency spectral density of $\xi(t)$ scales as dt, the typical fluctuation should scale as $\sqrt{dt}$, thus explaining such dependence for the error bars in Fig. 5.8. Simply speaking, for a wide-bandwith noise the average value of $1-\eta$ depends on the overall r.m.s. value of the noise, while the fluctuations of $1-\eta$ (from run to run) depend on the spectral density of the noise at relatively low frequencies ($\lesssim \tau^{-1}$). Note that the noise can increase or decrease the inefficiency compared to its average value; however, it always increases the inefficiency in comparison with the case without noise (as we see from Fig. 5.8, even if we increase *dt* from 1 ns to about the buildup/leakage time of 33.3 ns, the error bars, increased by the factor $\sqrt{33.3}$, are still significantly less than the increase of inefficiency compared with the design value).

We have checked this explanation of the noise effect on the average inefficiency by replacing the fluctuating evolution equations (5.1)–(5.3) with non-fluctuating equations, in which the transfer term $\sqrt{\kappa_{\rm e}\kappa_{\rm r}}\,A$ does not change, while the leakage rates $\kappa_{\rm e}$ and $\kappa_{\rm r}$ are multiplied either by $1+a^2\,\overline{\xi^2}$ (for multiplicative noise) or by $1+a^2\,\overline{\xi^2}(\mathbf{t}_{\rm e(r),max}/\mathbf{t}_{\rm e(r)})^2$ for the additive noise. The results are shown in Fig. 5.8 by the dotted lines; we see that they almost coincide with the solid lines, thus confirming our explanation. We have also used several interpolation methods, which give somewhat different $\overline{\xi^2}$, and checked that the direct simulation with fluctuations and use of the non-fluctuating equations still give the same results.

As can be seen from Fig. 5.8, the average inefficiency depends approximately quadratically on the noise amplitude a for both additive and multiplicative noise. The additional inefficiency $-\delta\eta$ can be fitted numerically as

$$-\delta\eta \approx c_{\rm n} a^2\,\overline{\xi^2}, \tag{5.42}$$

where $c_\mathrm{n} \approx 2$ for the multiplicative noise and $c_\mathrm{n} \approx 2 \ln \frac{1}{1-\eta_\mathrm{d}}$ for the additive noise. Note that for the additive noise c_n increases with decreasing design inefficiency $1-\eta_\mathrm{d}$, so the blue lines in Fig. 5.8 intersect. This is because a smaller $1-\eta_\mathrm{d}$ requires a longer procedure duration t_f, causing more loss due to additional leakage of the resonators caused by fluctuating $\mathbf{t}_{\mathrm{e(r)}}$.

The value of c_n for the additive noise can be derived analytically in the following way. As discussed above, the noise essentially increases the resonator leakages, $\kappa^\mathrm{a}_{\mathrm{e(r)}}(t) = \kappa_{\mathrm{e(r)}}(t) + a^2\,\overline{\xi^2}/\tau$, without increasing the transferred field; therefore, it is equivalent to the effect of energy relaxation with $T_1 = \tau/(a^2\,\overline{\xi^2})$. Consequently (see below), the efficiency decreases as $\eta = \eta_\mathrm{d} \exp(-t_\mathrm{f}/T_1) = \eta_\mathrm{d} \exp(-2a^2\,\overline{\xi^2} \ln \frac{1}{1-\eta_\mathrm{d}})$ [see Eq. (5.18) for t_f], and the linear expansion of the exponent in this formula reproduces Eq. (5.42) with $c_\mathrm{n} = 2 \ln \frac{1}{1-\eta_\mathrm{d}}$.

The value of c_n for the multiplicative noise can be derived in a somewhat similar way. Now $\kappa^\mathrm{a}_\mathrm{e}(t) = \kappa_\mathrm{e}(t)(1 + a^2\,\overline{\xi^2})$, so the additional leakage of the emitting resonator consumes the fraction $a^2\,\overline{\xi^2}$ of the transmitted energy. Using the time-reversal picture, we see that an analogous increase of the receiving resonator leakage, $\kappa^\mathrm{a}_\mathrm{r}(t) = \kappa_\mathrm{r}(t)(1+a^2\,\overline{\xi^2})$, emits (back-reflects) into the transmission line the fraction $a^2\,\overline{\xi^2}$ of the final energy $|B(t_\mathrm{f})|^2$. Combining these two losses, we obtain $\eta = \eta_\mathrm{d}(1 - 2a^2\,\overline{\xi^2})$, which for $\eta_\mathrm{d} \approx 1$ reproduces Eq. (5.42) with $c_\mathrm{n} = 2$.

Overall, the efficiency decrease due to the multiplicative noise is not strong; for example, to keep $-\delta\eta < 0.01$ we need the relative r.m.s. fluctuations of $\mathbf{t}_{\mathrm{e(r)}}$ to be less than 7%. The (additive) fixed-amplitude fluctuations of $\mathbf{t}_{\mathrm{e(r)}}$ can be more problematic, because the inability to keep $\mathbf{t}_{\mathrm{e(r)}}$ near zero at the initial or final stage of the procedure leads to loss during most of the (relatively long) procedure. For example, for $\eta_{\rm d} = 0.99$ and $-\delta\eta < 0.01$, we need the r.m.s. fluctuations of $\mathbf{t}_{\rm e(r)}$ to be less than 3% of $\mathbf{t}_{\rm e(r),max}$.

5.3.7 Effect of dissipation

For completeness let us discuss here the effect of dissipation by assuming imperfect transfer through the transmission line, $\eta_{\rm tl} \neq 1$, and finite energy relaxation times $T_{1,\rm e}$ and $T_{1,\rm r}$ in the evolution equations (5.1)–(5.3), while the pulse shapes $\mathbf{t}_{\rm e}(t)$ and $\mathbf{t}_{\rm r}(t)$ are assumed to be ideal.

The effect of imperfect $\eta_{\rm tl}$ is easy to analyze, since the transmitted (classical) field is simply multiplied by $\sqrt{\eta_{\rm tl}}$. Therefore, the transfer procedure efficiency is simply multiplied by $\eta_{\rm tl}$, so that $\eta = \eta_{\rm tl}\eta_{\rm d}$. (Recall that we neglect multiple reflections.)

The effect of energy relaxation in the resonators is also very simple if $T_{1,\rm r} = T_{1,\rm e} = T_1$. Then the (classical) field decays equally everywhere, and therefore, after the procedure duration $t_{\rm f}$, the energy acquires the factor $\exp(-t_{\rm f}/T_1)$, so that $\eta = \eta_{\rm d}\exp(-t_{\rm f}/T_1)$. The analysis of the case when $T_{1,\rm r} \neq T_{1,\rm e}$ is not so obvious. We have analyzed this case numerically and found that the two resonators bring the factors $\exp(-t_{\rm f}/2T_{1,\rm e})$ and $\exp(-t_{\rm f}/2T_{1,\rm r})$, respectively.

Combining the effects of dissipation in the resonators and transmission line, and assuming everything else is ideal, we obtain

$$\eta = \eta_{\rm d}\eta_{\rm tl}\exp(-t_{\rm f}/2T_{1,\rm e})\exp(-t_{\rm f}/2T_{1,\rm r}). \tag{5.43}$$

5.4 Multiple reflections

So far we have not considered multiple reflections of the field that is back-reflected from the receiving end, by assuming either a very long transmission line or the presence of a circulator [see Fig. 5.1(b)]. If there is no circulator and the transmission line is not very long (as for the state transfer between two on-chip superconducting resonators), then the back-reflected field bounces back and forth between the couplers and thus affects the efficiency of the state transfer. To describe these multiple reflections, we modify the field equations (5.1)–(5.3) by including the back-propagating field $F(t)$ into the dynamics, for simplicity assuming in this section $\Delta\omega_{\rm r} = \Delta\omega_{\rm e} = 0$, $\eta_{\rm tl} = 1$, and $T^{-1}_{1,{\rm e(r)}} = 0$:

$$\dot{G}(t) = -\frac{\kappa_{\rm e}}{2}G(t) + \frac{\mathbf{t}_{\rm e}}{|\mathbf{t}_{\rm e}|}\frac{|\mathbf{r}_{\rm e}|}{\mathbf{r}^{\rm in}_{\rm e}}\sqrt{\kappa_{\rm e}}\, e^{i\varphi}F(t-t_{\rm d}), \tag{5.44}$$

$$\dot{B}(t) = -\frac{\kappa_{\rm r}}{2}B(t) + \frac{\mathbf{t}_{\rm r}}{|\mathbf{t}_{\rm r}|}\sqrt{\kappa_{\rm r}}A(t), \tag{5.45}$$

$$A(t) = \frac{\mathbf{t}_{\rm e}}{|\mathbf{t}_{\rm e}|}\sqrt{\kappa_{\rm e}}G(t) + \frac{\mathbf{r}^{\rm out}_{\rm e}}{|\mathbf{r}_{\rm e}|}e^{i\varphi}F(t-t_{\rm d}). \tag{5.46}$$

Here $t_{\rm d}$ is the round-trip delay time ($t_{\rm d} = 2l_{\rm tl}/v$, where $l_{\rm tl}$ is the transmission line length and v is the effective speed of light), $\varphi = \omega_{\rm e(r)}t_{\rm d}$ is the corresponding phase acquired in the round trip, $F(t)$ is given by Eq. (5.14), $\mathbf{r}^{\rm out}_{\rm e}$ is the reflection amplitude of the emitting resonator coupler from the transmission line side, and $\mathbf{r}^{\rm in}_{\rm e}$ is the same from the resonator side. Note that we use shifted clocks, so the propagation is formally infinitely fast in the forward direction and has velocity $v/2$ in the reverse direction; then the round-trip delay $t_{\rm d}$ and phase shift φ are accumulated in the back-propagation only; the field $F(t)$ is defined at the receiving resonator, and it comes to the emitting resonator as $e^{i\varphi}F(t-t_{\rm d})$. Also note that even though φ is proportional to $t_{\rm d}$, it is better to treat φ as an independent parameter, because the time-delay effects are determined by the ratio $t_{\rm d}/\tau$, which has a very different scale from $\varphi = (t_{\rm d}/\tau)\,\omega_{\rm e(r)}\tau$, since $\omega_{\rm e(r)}\tau \sim 10^3$.

There is some asymmetry between Eqs. (5.44) and (5.45) and also between Eqs. (5.46) and (5.13), which involves factors $\mathbf{r}_{\rm e(r)}^{\rm in}$. This is because in order to keep a simple form of the evolution equations (5.1)–(5.3), we essentially defined G as the field propagating towards the transmission line, while B propagates away from the transmission line. In this section we still assume that the phases of the transmission and reflection amplitudes ($\mathbf{t}_{\rm e(r)}$ and $\mathbf{r}_{\rm e(r)}^{\rm in(out)}$) do not change with time. For the tunable couplers of Refs. [106, 107] (see Appendix B) the transmission amplitudes $\mathbf{t}_{\rm e(r)}$ are mostly imaginary, the reflection amplitudes $\mathbf{r}_{\rm e(r)}^{\rm in}$ are close to -1, and $\mathbf{r}_{\rm e(r)}^{\rm out}$ are somewhat close to -1 (recall that $\mathbf{t}_{\rm e}^2/\mathbf{r}_{\rm e}^{\rm in}\mathbf{r}_{\rm e}^{\rm out}$ and $\mathbf{t}_{\rm r}^2/\mathbf{r}_{\rm r}^{\rm in}\mathbf{r}_{\rm r}^{\rm out}$ must be real and negative from unitarity). In simulations it is easier to redefine the phases of the fields in the resonators and transmission line, so that $\mathbf{t}_{\rm e}$ and $\mathbf{t}_{\rm r}$ are treated as real and positive numbers, $\mathbf{r}_{\rm e}^{\rm in}$ and $\mathbf{r}_{\rm r}^{\rm in}$ are also real and positive (close to 1), while $\mathbf{r}_{\rm e}^{\rm out}$ and $\mathbf{r}_{\rm r}^{\rm out}$ are real and negative (close to -1). In this case Eqs. (5.14) and (5.46) become $F = \sqrt{\kappa_{\rm r}}\,B - A$ and $A(t) = \sqrt{\kappa_{\rm e}}\,G(t) - e^{-i\varphi}F(t-t_{\rm d})$.

As an example of the dynamics with multiple reflections, in Fig. 5.9 we show the absolute value of the reflected field $F(t-t_{\rm d})$ (at the emitting resonator) for the procedure shown in Fig. 5.2 ($\eta_{\rm d} = 0.999$, $t_{\rm f} = 460$ ns) for the round-trip delays $t_{\rm d} = t_{\rm f}/2$ (blue dashed curve) and $t_{\rm d} = t_{\rm f}/5$ (red solid curve), assuming $\varphi = \pi/8$. The kinks represent the successive reflections of the field emitted at

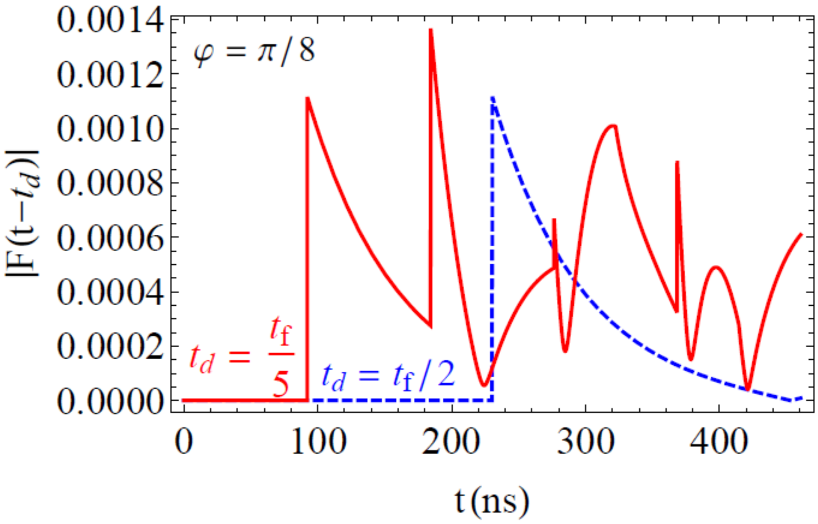

Figure 5.9: Illustration of the back-reflected field $|F(t - t_{\rm d})|$ reaching the emitting resonator at time t, for the round-trip delay time $t_{\rm d} = t_{\rm f}/2$ (blue dashed curve) and $t_{\rm d} = t_{\rm f}/5$ (red solid curve), assuming the round-trip phase shift $\varphi = \pi/8$. The kinks represent multiple reflections of the field emitted at $t = 0$. We assumed parameters of Fig. 5.2 ($\eta_{\rm d} = 0.999$, $\tau = 33.3$ ns, $t_{\rm f} = 460$ ns).

$t = 0$. Note that depending on the phase shift φ, the resulting contribution of the reflected field into $B(t_{\rm f})$ can either increase or decrease $|B(t_{\rm f})|^2$, thus either decreasing or increasing the transfer efficiency η (recall that the efficiency η is defined disregarding the resulting phase $\varphi_{\rm f}$, because it can be easily corrected in an experiment). The effect of multiple reflections should vanish if $t_{\rm d} \geq t_{\rm f}$, i.e. when the transmission line is sufficiently long.

Figure 5.10 shows the numerically calculated inefficiency $1-\eta$ of the state transfer as a function of the round-trip delay time $t_{\rm d}$, normalized by the buildup/leakage time $\tau_{\rm e} = \tau_{\rm r} = \tau$. Different curves represent different values of the phase φ. The design efficiency is $\eta_{\rm d} = 0.999$. (In the simulations we also used $\omega_0/2\pi = 6$ GHz, and $\mathbf{t}_{\rm e,max} = \mathbf{t}_{\rm r,max} = 0.05$; however, the presented results do not depend on these parameters). We see that the inefficiency shows an oscillatory behavior as a function of the delay time, but it is always within the range $0 \leq 1-\eta \leq 2(1-\eta_{\rm d})$. This important fact was proved in Ref. [119] in the following way. In the case with the circulator, the losses are $1-\eta_{\rm d} = l_G^{\rm circ} + l_F^{\rm circ}$, where $l_G^{\rm circ} = |G^{\rm circ}(t_{\rm f})|^2$ is due to the untransmitted field [we assume here $G(0)=1$] and $l_F^{\rm circ}$ is the dimensionless energy carried away by the reflected field $F^{\rm circ}(t)$. In the case without circulator, we can simply add the multiple reflections of the field $F^{\rm circ}(t)$ to the evolution with the circulator. At the final time $t_{\rm f}$ the field $F^{\rm circ}(t)$ will linearly contribute to $B(t_{\rm f})$, $G(t_{\rm f})$, and the field within the transmission line [$F(t)$ for $t_{\rm f} - t_{\rm d} \leq t \leq t_{\rm f}$]. In the worst-case scenario the whole energy $l_F^{\rm circ}$ is added in-phase to the untransmitted field $G^{\rm circ}(t_{\rm f})$, resulting in $1-\eta = (\sqrt{l_G^{\rm circ}} + \sqrt{l_F^{\rm circ}})^2$. Since $(\sqrt{l_G^{\rm circ}} + \sqrt{l_F^{\rm circ}})^2 \leq 2(l_G^{\rm circ} + l_F^{\rm circ})$ always, we obtain the upper bound for the inefficiency, $1-\eta \leq 2(1-\eta_{\rm d})$. The lower bound $1-\eta \geq 0$ is obvious. Figure 5.10 shows that both bounds can be reached (at least approximately) with multiple reflections at certain values of $t_{\rm d}/\tau$ and φ (this fact is not obvious and is even somewhat surprising).

The dependence $\eta(t_{\rm d})$ shown in Fig. 5.10 is quite complicated and depends on the phase φ. We show only phases $0 \leq \varphi \leq \pi$, while for $\pi \leq \varphi \leq 2\pi$ the results can be obtained from the symmetry $\eta(t_{\rm d}, \varphi) = \eta(t_{\rm d}, 2\pi - \varphi)$. As we see from Fig. 5.10, the oscillations of $\eta(t_{\rm d})$ generally decrease in amplitude when $t_{\rm d}/\tau \to 0$, so that we expect a saturation of the dependence at $t_{\rm d}/\tau \to 0$. The exception is the case $\varphi = 0$, when the oscillation amplitude does not significantly decrease at small $t_{\rm d}/\tau$ (numerical simulations become increasingly more difficult at smaller $t_{\rm d}/\tau$).

This can be understood as due to the fact that for $\varphi = 0$ the transmission line is a resonator, which is resonant with the frequency $\omega_{\mathrm{e}} = \omega_{\mathrm{r}}$ of the resonators.

Note that for an experiment with on-chip state transfer between superconducting resonators, the round-trip delay time t_{d} is comparable to $\omega_{\mathrm{e(r)}}^{-1}$ and therefore much smaller than τ, $t_{\mathrm{d}}/\tau \sim 10^{-2}$. This regime is outside of the range accessible to our direct simulation method, which works well only when $t_{\mathrm{d}}/\tau \gtrsim 10^{-1}$. Nevertheless, we expect that the results presented in Fig. 5.10(b) can be approximately used in this case as well, because of the apparent saturation of $\eta(t_{\mathrm{d}})$ at $t_{\mathrm{d}} \to 0$, except when the phase φ is close to zero.

The most important result of this section is that multiple reflections cannot increase the inefficiency $1 - \eta$ by more than twice compared with the design inefficiency $1 - \eta_{\mathrm{d}}$ (as obtained analytically and confirmed numerically).

5.5 Mismatch of the resonator frequencies

The main idea of the state transfer protocol analyzed here is to use destructive interference to suppress the back-reflection into the transmission line, thus providing a high-efficiency transfer. This is why it is crucial that the emitting and receiving resonators have almost the same frequency. Therefore, a mismatch between the two resonator frequencies should strongly decrease the transfer efficiency. In this section we analyze the effect of the frequency mismatch using two models. First, we assume a constant-in-time mismatch. Second, we consider the time-dependent detuning of the resonator frequencies due to the changing transmission amplitudes of the couplers, which lead to a changing complex phase of the reflection amplitudes (see Appendix B) and thus to the resonator frequency change.

5.5.1 Constant in time frequency mismatch

We first consider the case when the two resonator frequencies are slightly different, $\Delta\omega \equiv \omega_{\rm e} - \omega_{\rm r} \neq 0$, and they do not change in time. Everything else is assumed to be ideal. It is easy to understand the effect of detuning by using the evolution equations (5.1)–(5.3) and choosing $\omega_0 = \omega_r$, so that $\Delta\omega_{\rm e} = \Delta\omega$ and $\Delta\omega_{\rm r} = 0$. Then, compared with the case $\Delta\omega = 0$, the emitting resonator field $G(t)$ acquires the phase factor $e^{-i\Delta\omega t}$; the same phase factor is acquired by the transmitted field $A(t)$ in Eq. (5.2), and this changing phase destroys the perfect phase synchronization between $A(t)$ and $B(t)$ that is needed to cancel the back-reflection.

The numerically calculated inefficiency $1-\eta$ is shown in Fig. 5.11 as a function of the detuning $\Delta\omega$, normalized by the inverse buildup/leakage time τ^{-1} (we assumed $\tau_{\rm e} = \tau_{\rm r} = \tau$). We show the lines for the design inefficiencies $\eta_{\rm d} = 0.9$, 0.99, and 0.999. The results do not depend on $\omega_{\rm r}$ and $|\mathbf{t}_{\rm e(r),max}|$. However, to express $\Delta\omega/2\pi$ in MHz on the upper horizontal axis, we use a particular example of $\omega_{\rm r}/2\pi = 6$ GHz and $|\mathbf{t}_{\rm e(r),max}| = 0.05$, for which $\tau = 33.3$ ns (as in Fig. 5.2).

For small $|\Delta\omega\,\tau|$ and $\eta_{\rm d} \approx 1$, the additional inefficiency due to frequency mismatch can be fitted as

$$-\,\delta\eta \approx c_{\rm fm}\,(\Delta\omega\,\tau)^2, \;\; c_{\rm fm}\approx 2. \tag{5.47}$$

For smaller $\eta_{\rm d}$ the coefficient $c_{\rm fm}$ decreases, so that $c_{\rm fm} \approx 1.94$ for $\eta_{\rm d} = 0.999$, $c_{\rm fm} \approx 1.68$ for $\eta_{\rm d} = 0.99$, and $c_{\rm fm} \approx 0.81$ for $\eta_{\rm d} = 0.9$.

It is interesting that the value $c_{\rm fm} = 2$ for $\eta_{\rm d} \approx 1$ exactly coincides with the estimate derived in Ref. [119], which we rederive here. Comparing the case $\Delta\omega \neq 0$ with the ideal case $\Delta\omega = 0$, we can think that $A(t)$ acquires the extra phase factor $e^{-i\Delta\omega(t-t_{\rm m})}$, where $t_{\rm m}$ is the mid-time of the procedure (see Fig. 5.2); the overall factor $e^{i\Delta\omega t_{\rm m}}$ is not important, affecting only the final phase $\varphi_{\rm f}$. Then we can think that at $t = t_{\rm m}$ we still have an almost perfect cancellation of the back-reflection, $F(t_{\rm m}) \approx 0$; however, at $t \neq t_{\rm m}$ the extra phase causes the back-reflected wave $|F(t)| \approx |A(t)(e^{-i\Delta\omega(t-t_{\rm m})} - 1)|$. Now using $|A(t)| = |A(t_{\rm m})|e^{-|t-t_{\rm m}|/2\tau}$ and assuming $|\Delta\omega|\tau \ll 1$ (so that we can expand the exponent in the relevant time range), we find $|F(t)| \approx |A(t_{\rm m})|\, e^{-|t-t_{\rm m}|/2\tau}|\Delta\omega(t-t_{\rm m})|$. Finally integrating the loss, $\int |F(t)|^2 dt$, and normalizing it by the transferred "energy" $\int |A(t_{\rm m})|^2 e^{-|t-t_{\rm m}|/\tau} dt$, we obtain the added inefficiency $-\delta\eta \approx 2\,(\Delta\omega\,\tau)^2$.

Using this derivation, it is easy to understand why the coefficient $c_{\rm fm}$ in Eq. (5.47) decreases with decreasing $\eta_{\rm d}$. This occurs because the integration of $|F(t)|^2$ is limited by the range $0 < t < t_{\rm f} = -2\tau \ln(1-\eta_{\rm d})$, which becomes shorter for smaller $\eta_{\rm d}$. Thus we can estimate $c_{\rm fm}$ as $c_{\rm fm} \approx \int_0^{-\ln(1-\eta_{\rm d})} x^2 e^{-x} dx = 2 - (1-\eta_{\rm d})[2 - 2\ln(1-\eta_{\rm d}) + \ln^2(1-\eta_{\rm d})]$, which fits the numerical results very well.

As expected, even small detuning significantly decreases the transfer efficiency. For example, to keep the added inefficiency under 1%, $-\delta\eta < 0.01$, we need the detuning to be less than 0.4 MHz in the above example ($\tau = 33.3$ ns), which is not very easy to achieve in an experiment.

5.5.2 Time-dependent detuning due to changing coupling

In an actual experimental coupler, the parameters are interrelated, and a change of the coupling strength by varying $|\mathbf{t}|$ may lead to a change of other parameters. In particular, for the coupler realized experimentally in Refs. [106, 107], the change of $|\mathbf{t}|$ causes a small change of the complex phases of the transmission and reflection amplitudes $\mathbf{t}$ and $\mathbf{r}^{\rm in(out)}$. The phase change of $\mathbf{r}^{\rm in}$ (from the resonator side) causes a change of the resonator frequency. Thus, changing the coupling causes the frequency detuning, as was observed experimentally [106]. Since the frequency mismatch between the two resonators strongly decreases the efficiency of the state transfer, this is a serious problem for the protocol discussed in this chapter. Here we analyze this effect quantitatively and discuss with which accuracy the detuning should be compensated (e.g. by another tunable element) to preserve the high-efficiency transfer.

Physically, the resonator frequency changes because the varying coupling changes the boundary condition at the end of the coplanar waveguide resonator (see Fig. B.1 in Appendix B). Note that a somewhat similar frequency change due to changing coupling with a transmission line was studied in Ref. [149].

As discussed in Appendix B, if we use the tunable couplers of Ref. [106, 107], then the transmission and refection amplitudes $\mathbf{t}_j$ and $\mathbf{r}_j^{\rm in(out)}$ for the two resonators

$(j = \mathrm{e}, \mathrm{r})$ are given by the formulas

$$\mathbf{t}_j = -i\frac{2\omega_j M_j}{1+b_j}\sqrt{\frac{R_j}{R_{\rm tl}}}\left(\frac{1}{R_j} + \frac{-ib_j}{\omega_j L_{e,j}}\right)\frac{1}{1 - i\omega_j L_{2,j}/R_{\rm tl}}, \tag{5.48}$$

$$\mathbf{r}_j^{\rm in} = -\frac{1-b_j}{1+b_j}, \;\; \mathbf{r}_j^{\rm out} = -(\mathbf{r}_j^{\rm in})^* \frac{\mathbf{t}_j}{\mathbf{t}_j^*}, \tag{5.49}$$

where

$$b_j = \frac{i\omega L_{1,j}/R_j}{\dfrac{L_{1,j}}{L_{e,j}} + \left[1 - \dfrac{i\omega_j M_j^2}{R_{\rm tl} L_{1,j}(1 + i\omega_j L_{2,j}/R_{\rm tl})}\right]^{-1}}, \tag{5.50}$$

M_j is the effective mutual inductance in jth coupler (the main tunable parameter controlled by magnetic flux in the SQUID loop), R_j and $R_{\rm tl}$ are the wave impedances of the resonators and the transmission line, ω_j are the resonator frequencies, and $L_{1,j}$, $L_{2,j}$, and $L_{e,j}$ are the effective inductances used to describe the coupler (see details in Appendix B). Note that Eqs. (5.48) and (5.50) are slightly different from the equations in the Supplementary Information of Ref. [106] and the derivation in Appendix B: the difference is that the imaginary unit i is replaced with $-i$ to conform with the chosen rotating frame definition $e^{-i\omega t}$ in Eqs. (5.1) and (5.2).

For the typical experimental parameters, $|b_j| \ll 1$, so that $\mathbf{r}_j^{\rm in} \approx -1$, while $\mathbf{t}_j$ is mostly imaginary. Note that $\omega_{\rm e} \approx \omega_{\rm r} \approx \omega_0$, so in Eqs. (5.48) and (5.50) we can replace ω_j with ω_0. Also note that there is no coupling, $\mathbf{t}_j = 0$, when $M_j = 0$, and the coupling changes sign when M_j crosses zero.

Tuning M_j, we control $|\mathbf{t}_j|$. However, the complex phase of $\mathbf{t}_j$ slightly changes with changing M_j because b_j in Eq. (5.48) depends on M_j and also $L_{1,j}$ and $L_{2,j}$

depend on M_j – see Appendix B. Changing the phase of $\mathbf{t}_j$ leads to the phase mismatch in the state transfer protocol, degrading its efficiency. However, this is a relatively minor effect, while a much more serious effect is the dependence of the complex phase of $\mathbf{r}_j^{\rm in}$ on M_j via its dependence on b_j in Eq. (5.49), leading to the resonator frequency change.

For the rotating frame $e^{-i\omega t}$ and quarter-wavelength resonator (which we assume here) the change $\delta(\arg \mathbf{r}_j^{\rm in})$ of the phase of $\mathbf{r}_j^{\rm in}$ changes the resonator frequency by

$$\delta\omega_j \approx -(\omega_0/\pi)\, \delta(\arg \mathbf{r}_j^{\rm in}), \tag{5.51}$$

where we used $\omega_j \approx \omega_0$. Assuming for simplicity that the resonators are exactly on resonance ($\omega_{\rm e} = \omega_{\rm r} = \omega_0$) when there is no coupling ($M_{\rm e} = M_{\rm r} = 0$), we can write the variable detunings to be used in the evolution equations (5.1) and (5.2) as

$$\Delta\omega_j = \omega_j - \omega_0 = -\frac{\omega_0}{\pi}\left[\arg \mathbf{r}_j^{\rm in}(M_j) - \arg \mathbf{r}_j^{\rm in}(0)\right], \tag{5.52}$$

where $\mathbf{r}_j^{\rm in}(M_j)$ describes dependence on M_j. Since $|\mathbf{t}_j|$ also depends on M_j (linearly to first approximation), we have an implicit dependence $\Delta\omega_j(|\mathbf{t}_j|)$, which is linear for small $|\mathbf{t}_j|$ [see Eq. (B.17) in Appendix B] and becomes nonlinear for larger $|\mathbf{t}_j|$.

This dependence $\Delta\omega_{\rm e(r)}(|\mathbf{t}_{\rm e(r)}|)$ is shown in Fig. 5.12 by the solid line for the parameters of the coupler similar (though not equal) to the parameters of the experimental coupler [106]: $R_{\rm e(r)} = 80\,\Omega$, $R_{\rm tl} = 50\,\Omega$, $\omega_0/2\pi = 6\,$GHz, $L_{1,j} - M_j = L_{2,j} - M_j = 620\,$pH, and $L_{e,j} = 180\,$pH (see Appendix B). In particular, Fig.

5.12 shows that $|\mathbf{t}_{\mathrm{e(r)}}| = 0.05$ corresponds to the frequency change by -18.6 MHz, which is a very big change compared to what is tolerable for a high-efficiency state transfer (see Fig. 5.11). The same detuning normalized by $\kappa_{\mathrm{e(r)}} = |\mathbf{t}_{\mathrm{e(r)}}|^2\omega_{\mathrm{e(r)}}/\pi$ is shown in Fig. 5.13 by the dashed line.

The value of $M_{\mathrm{e(r)}}$ needed to produce a given $|\mathbf{t}_{\mathrm{e(r)}}|$ is shown in Fig. 5.12 by the dashed line. It is interesting that the dependence $M(|\mathbf{t}|)$ is significantly more nonlinear than the dependence $\Delta\omega(|\mathbf{t}|)$, indicating that the nonlinearities of $|\mathbf{t}(M)|$ and $\Delta\omega(M)$ in Eqs. (5.48) and (5.52) partially cancel each other (see Appendix B).

The solid line in Fig. 5.13 shows dependence of the phase $\arg[\mathbf{t}_{\mathrm{e(r)}}]$ on the absolute value $|\mathbf{t}_{\mathrm{e(r)}}|$. Even though the phase change looks significant, it produces a relatively minor decrease in the protocol inefficiency (as we will see later) because the loss is quadratic in the phase mismatch.

We numerically simulate the state transfer protocol, accounting for the frequency change of the resonators and phase change of $\mathbf{t}_{\mathrm{e(r)}}$ in the following way. First, we use the ideal pulse shapes $|\mathbf{t}_{\mathrm{e}}(t)|$ and $|\mathbf{t}_{\mathrm{r}}(t)|$ from Eqs. (5.22)–(5.25), assuming a symmetric setup ($\tau_{\mathrm{e}} = \tau_{\mathrm{r}}$). Then we calculate the corresponding dependences $M_{\mathrm{e}}(t)$ and $M_{\mathrm{r}}(t)$ using Eq. (5.48) and find $\mathbf{t}_{\mathrm{e}}(t)$ and $\mathbf{t}_{\mathrm{r}}(t)$ (now with time-dependent phases) using the same Eq. (5.48), and also find the detunings $\Delta\omega_{\mathrm{e}}(t)$ and $\Delta\omega_{\mathrm{r}}(t)$ using Eq. (5.52). After that we solve the evolution equations (5.1)–(5.3), neglecting multiple reflections. Note that we convert $|\mathbf{t}_j(t)|$ into $M_j(t)$ by first numerically calculating $|\mathbf{t}_j(M_j)|$ from Eq. (5.48), then fitting the inverse dependence $M_j(|\mathbf{t}_j|)$ with a polynomial of 40th order, and then using this polynomial for the conversion.

Figure 5.14 shows the numerically calculated inefficiency $1-\eta$ of the transfer protocol as a function of the maximum transmission amplitude $|\mathbf{t}_{\rm e,max}| = |\mathbf{t}_{\rm r,max}|$ for the above example of the coupler parameters and design efficiencies $\eta_{\rm d} = 0.99$ and 0.999. Besides showing the results for the usual protocol (red lines), we also show the results for the cases when the frequency detuning [Eq. (5.52)] is reduced by a factor of 10 (90% compensation, blue lines), 20 (95% compensation, green lines), 100 (99% compensation, magenta lines) and fully eliminated (100% compensation, black lines). Such compensation can be done experimentally by using another circuit element, affecting the resonator frequency, e.g., tuning the phase of the reflection amplitude at the other end of the resonator by a SQUID-controlled inductance.

We see that without compensation of the frequency detuning the state transfer protocol cannot provide a high efficiency: $\eta = 0.33$ for $|\mathbf{t}_{\rm max}| = 0.05$ and $\eta = 0.58$ for $|\mathbf{t}_{\rm max}| = 0.1$. However, with the detuning compensation the high efficiency may be restored. As we see from Fig. 5.14, the state transfer efficiency above 99% requires the detuning compensation at least within 90%–95% range (depending on $|\mathbf{t}_{\rm max}|$). Note that even with 100% compensation, the efficiency is less than in the ideal case. This is because of the changing phases of $\mathbf{t}_{\rm e}(t)$ and $\mathbf{t}_{\rm r}(t)$. However, this effect is minor in comparison with the effect of detuning.

It is interesting that the curves in Fig. 5.14 decrease with increasing $|\mathbf{t}_{\rm max}|$ when $|\mathbf{t}_{\rm max}|$ is not too large. This may seem counterintuitive, since larger $|\mathbf{t}|$ leads to larger detuning, and so we would naively expect larger inefficiency at larger $|\mathbf{t}_{\rm max}|$. The numerical result is opposite because the duration of the procedure decreases, scaling as $\tau \propto |\mathbf{t}_{\rm max}|^{-2}$. Therefore if the largest detuning scales linearly, $|\Delta\omega_{\rm max}| \propto |\mathbf{t}_{\rm max}|$, then the figure of merit $|\Delta\omega_{\rm max}\tau|$ scales as $|\mathbf{t}_{\rm max}|^{-1}$, thus explaining the decreasing part of the curves in Fig. 5.14. The upper horizontal axis in Fig. 5.14 shows $|\Delta\omega_{\rm max}\tau|$, which indeed decreases with increasing $|\mathbf{t}_{\rm max}|$ (see also the dashed line in Fig. 5.13).

More quantitatively, let us assume a linear detuning, $\Delta\omega_{\rm e(r)} = k\,|\mathbf{t}_{\rm e(r)}|$, where the coefficient k is given by Eq. (B.17) multiplied by the uncompensated fraction of the detuning. Assuming a small deviation from the ideal protocol, the transmitted wave is $|A(t)| = |A(t_m)|\,e^{-|\Delta t|/2\tau}$, where $\Delta t = t - t_{\rm m}$. At the mid-time $t_{\rm m}$ the resonator frequencies coincide, but at $t > t_{\rm m}$ the receiving resonator frequency changes so that $\Delta\omega = \omega_{\rm e} - \omega_{\rm r} = k(|\mathbf{t}_{\rm r}(t_{\rm m})| - |\mathbf{t}_{\rm r}(t)|)$. Using Eq. (5.24) we find $\Delta\omega = k\,|\mathbf{t}_{\rm max}|\,[1 - (2e^{\Delta t/\tau} - 1)^{-1/2}]$. The accumulated phase mismatch is then $\phi(t) = \int_{t_m}^{t} \Delta\omega(t')\,dt'$, which produces the reflected wave $|F| \approx |A\phi|$, assuming small ϕ. The inefficiency due to the reflected wave loss is then $1-\eta \approx \int_{t_m}^{\infty} |F(t)|^2\,dt / \int_{t_m}^{\infty} |A(t)|^2\,dt$ (note that due to symmetry the same relative loss is before and after $t_{\rm m}$). Therefore $1-\eta \approx \tau^{-1}k^2|\mathbf{t}_{\rm max}|^2 \int_0^{\infty}\{\int_0^{x}[1 - (2e^{\Delta t/\tau} - 1)^{-1/2}]\,d\Delta t\}^2 e^{-x/\tau}dx$, and calculating the integral numerically we obtain $1-\eta = 0.63\,k^2\tau^2|\mathbf{t}_{\rm max}|^2$ [the numerical value of the integral is somewhat smaller than 0.63 if we limit the outer integration by $-\tau \ln(1-\eta_{\rm d})$]. Finally using $\tau = \pi/\omega_0|\mathbf{t}_{\rm max}|^2$, we obtain $1-\eta \approx 0.6\,(k\pi/\omega_0|\mathbf{t}_{\rm max}|)^2$.

Numerical results in Fig. 5.14 reproduce the scaling $1-\eta \propto (k/|\mathbf{t}_{\rm max}|)^2$ for the significant part of the curves for $\eta_{\rm d} = 0.999$ (when plotted in log-log scale); however, the prefactor in the numerical fitting is somewhat different from what we obtained above: $1-\eta \approx 0.4\,(k\pi/\omega_0|\mathbf{t}_{\rm max}|)^2$. Note that at sufficiently large $|\mathbf{t}_{\rm max}|$ the green and red curves in Fig. 5.14 reach a minimum and then start to increase. This occurs because the inefficiency due to changing phase of $\mathbf{t}_{\rm e(r)}$ increases with increasing $|\mathbf{t}_{\rm max}|$, in contrast to the effect of frequency detuning.

Actually, our analysis of the transfer process in the case of complete compensation of detuning is not fully accurate. The reason is that in the evolution equations (5.1)–(5.3) we took into account the frequency change due to changing $\mathbf{r}^{\rm in}_{\rm e(r)}$, but we did not take into account another (very small) effect due to changing $\mathbf{r}^{\rm in}_{\rm e(r)}$. It is easy to understand the origin of this effect in the following way. There is a phase difference $\arg(\mathbf{r}^{\rm in}_{\rm r})$ between the field B propagating away from the transmission line and the similar field propagating towards the transmission line [see Eq. (5.13) and discussion below it]. Changing $\arg(\mathbf{r}^{\rm in}_{\rm r})$ alters this phase difference, thus affecting both fields and correspondingly leading to an extra term, neglected in Eq. (5.2). Similarly, changing $\arg(\mathbf{r}^{\rm in}_{\rm e})$ leads to an extra term in Eq. (5.1) for G. However, as can be seen from Fig. 5.12 and Eq. (5.51), the change of $\arg(\mathbf{r}^{\rm in}_{\rm e(r)})$ is less than 0.02 for $|\mathbf{t}_{\rm e(r)}|$ varying between 0 and 0.1, which is much less than the change of $\arg(\mathbf{t}_{\rm e(r)})$ in Fig. 5.13. Therefore, the neglected effect is much less than the effect due to changing $\arg(\mathbf{t}_{\rm e(r)})$, which by itself is almost negligible, as seen in Fig. 5.14. Note that the compensation for changing phases can be done experimentally in the same way as the compensation for the detuning, so that in principle the efficiency decrease analyzed in this section can be fully avoided.

Overall, we see that the detuning of the resonator frequencies due to a changing coupling is a serious problem for the state transfer protocol. A high-efficiency state transfer is possible only with additional experimental effort to compensate for this detuning. The required compensation accuracy is crudely within 90%–95% range. The use of a shorter protocol (by using a stronger coupling) helps to increase the efficiency. Note that the frequency compensation is done routinely for the tunable coupler of Refs. [124, 125]; similarly, the phase compensation can be naturally realized in the tunable coupler of Refs. [138, 139].

5.6 Summary

In this chapter, we have analyzed the robustness of the quantum state transfer protocol of Ref. [119] for the transfer between two superconducting resonators via a transmission line. The protocol is based on destructive interference, which cancels the back-reflection of the field into the transmission line at the receiving end (we believe this explanation is more natural than the terminology of time reversal, introduced in Ref. [108]). This is achieved by using tunable couplers for both resonators and properly designed time-dependences (pulse shapes) of the transmission amplitudes $\mathbf{t}_{\rm e}(t)$ and $\mathbf{t}_{\rm r}(t)$ for these couplers. Nearly-perfect transfer efficiency η can be achieved in the ideal case. We have focused on analyzing additional inefficiency due to deviations from the ideal case.

The ideal pulse shapes of the transmission amplitudes [Eqs. (5.22)–(5.25)] depend on several parameters; we have studied additional inefficiency due to deviations of these parameters from their design values. Below, we summarize our results by presenting the tolerable deviations for a fixed additional inefficiency of $-\delta\eta = 0.01$ (because of quadratic scaling, the tolerable inaccuracies for $-\delta\eta = 0.001$ are about 3.2 times smaller). For the relative deviations of the maximum transmission amplitudes $|\mathbf{t}_{\rm e,max}|$ and $|\mathbf{t}_{\rm r,max}|$, the tolerable ranges are $\pm 10\%$ if only one of them is changing and $\pm 5\%$ if both of them are changing simultaneously [see Fig. 5.3 and Eq. (5.34)]. For the relative deviations of the time scale parameters $\tau_{\rm e}$ and $\tau_{\rm r}$ describing the exponential increase/decrease of the transmitted field, the tolerable ranges are $\pm 17\%$ if only one of them is changing and $\pm 11\%$ if both of them are changing simultaneously [see Fig. 5.4 and Eq. (5.35)]. For the mismatch between the mid-times $t_{\rm m}$ of the procedure in the two couplers, the tolerable range is $\pm 0.2\tau \simeq \pm 6$ ns [see Fig. 5.5 and Eq. (5.36)]. For a nonlinear distortion described by warping parameters $\alpha_{\rm e}$ and $\alpha_{\rm r}$ [see Eq. (5.37)], the tolerable parameter range is ± 0.2 if the distortion affects only one coupler and ± 0.13 if the distortion affects both couplers. Our results show that smoothing of the pulse shapes by a Gaussian filter practically does not affect the inefficiency; even filtering with the width $\sigma \simeq \tau \simeq 30$ ns is still tolerable. When the pulse shapes are distorted by an additional (relatively high-frequency) noise, the tolerable range for the standard deviation of $|\mathbf{t}_{\rm e(r)}|$ is 7% of the instantaneous value and 3% of the maximum value [see Fig. 5.8 and Eq. (5.42)]. Overall, we see that the state transfer procedure is surprisingly robust to various distortions of the pulse shapes.

We have also analyzed the effect of multiple reflections and found that it can both increase or decrease the transfer efficiency. However, even in the worst case, this effect cannot increase the inefficiency $1-\eta$ by more than a factor of 2 (see Fig. 5.10). The energy dissipation in the transmission line or in the resonators can be a serious problem for the state transfer protocol. The description of the effect is simple [see Eq. (5.43)]; for a high-efficiency transfer we can tolerate only a weak dissipation $1-\eta_{\rm tl}$ in the transmission line, and we also need the procedure duration $t_{\rm f}$ to be much shorter than the energy relaxation time T_1. In particular, for $-\delta\eta = 0.01$ we need $\eta_{\rm tl} > 0.99$ and $T_1 > 100\, t_{\rm f}$.

The major problem in realizing the state transfer protocol is the frequency mismatch between the two resonators, since the destructive interference is very sensitive to the frequency mismatch. For a fixed detuning, the tolerable frequency mismatch $(\omega_{\rm e} - \omega_{\rm r})/2\pi$ for $-\delta\eta = 0.01$ is only $\pm 0.01/\tau \simeq \pm 0.4$ MHz [see Fig. 5.11 and Eq. (5.47)]; the tolerable range is a factor of $\sqrt{10}$ smaller for $-\delta\eta = 0.001$. An even more serious problem is the change of the resonator frequencies caused by changing couplings, which for the coupler of Ref. [106] is on the order of 20 MHz [see Fig. 5.12 and Eq. (B.17) in Appendix B]. Without active compensation for this frequency change, a high-efficiency state transfer is impossible. Our numerical results show (see Fig. 5.14) that to realize efficiency $\eta = 0.99$, the accuracy of the compensation should be at least 90% (i.e., the frequency change should be decreased by an order of magnitude). It is somewhat counterintuitive that a better efficiency can be obtained by using a higher maximum coupling, which increases the frequency mismatch but decreases duration of the procedure (see Fig. 5.14). Another effect that decreases the efficiency is the change of the phase of the transmission amplitude with changing coupling. However, this effect produces a relatively minor decrease of the efficiency (see Fig. 5.14).

In most of the chapter we have considered a classical state transfer, characterized by the (energy) efficiency η. However, all the results have direct relation to the transfer of a quantum state (see Appendix A). In particular, for a qubit state transfer, the quantum process fidelity F_χ is $F_\chi \approx 1-(1-\eta)/2$ for $\eta \approx 1$ [see Eq. (5.12)].

The quantum state transfer protocol analyzed here has already been partially realized experimentally. In particular, the realization of the proper (exponentially increasing) waveform for the quantum signal emitted from a qubit has been demonstrated in Ref. [125] (a reliable frequency compensation has also been demonstrated in that paper). The capture of such a waveform with 99.4% efficiency has been demonstrated in Ref. [107]. We hope that the full protocol that combines these two parts will be realized in the near future.

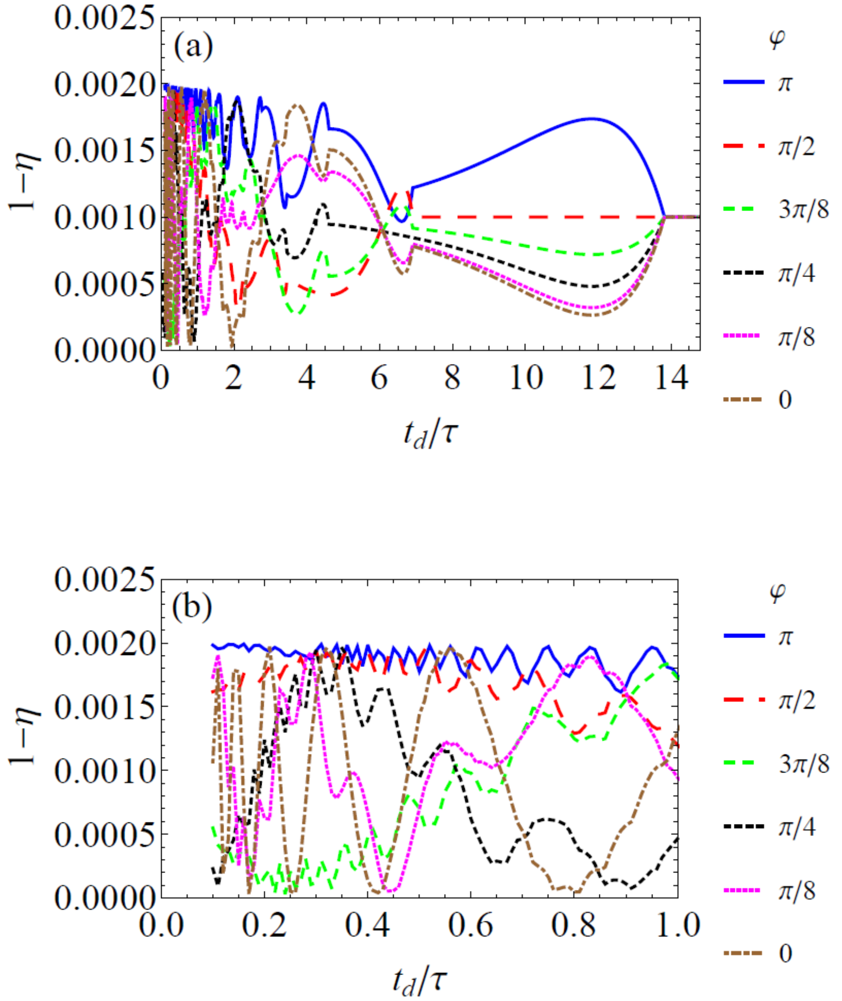

Figure 5.10: (a) Dependence of the inefficiency $1 - \eta$ on the normalized delay t_d/τ due to the round trip along the transmission line, for the design efficiency $\eta_\mathrm{d} = 0.999$ and several values of the phase shift φ accumulated in this round trip. The kinks at $t_\mathrm{d}/\tau = 13.8/n$ correspond to the integer number n of the round trips within the procedure time t_f. (b) The same as in (a) for a smaller range of t_d/τ (the results for $t_\mathrm{d}/\tau < 0.1$ were not calculated). Notice that the inefficiency accounting for multiple reflections does not exceed twice the design inefficiency, $1 - \eta \leq 2(1 - \eta_\mathrm{d})$.

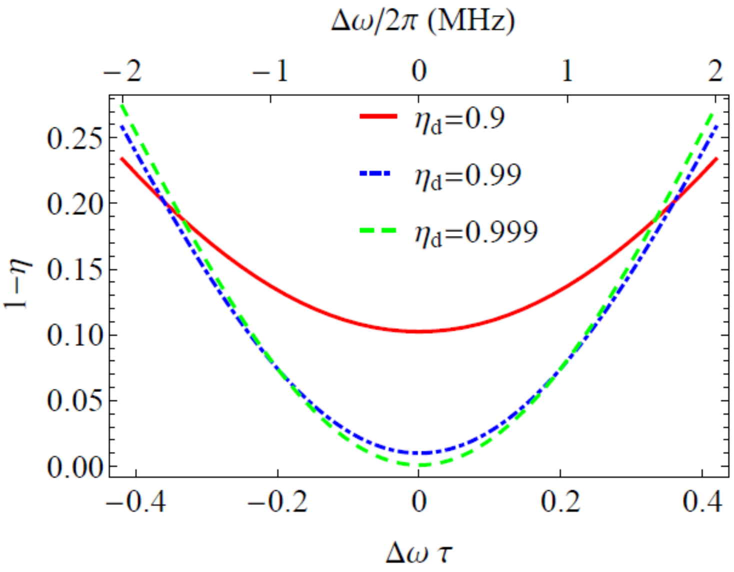

Figure 5.11: Inefficiency $1-\eta$ as a function of normalized detuning $\Delta\omega\,\tau$ (lower horizontal axis) for three design efficiencies, $\eta_\mathrm{d} = 0.9$, 0.99, and 0.999. The upper horizontal axis shows the unnormalized detuning $\Delta\omega/2\pi$ in MHz, using the values $\omega/2\pi = 6$ GHz and $|\mathbf{t}_{\mathrm{e,max}}| = |\mathbf{t}_{\mathrm{r,max}}| = 0.05$, so that $\tau = 33.3$ ns.

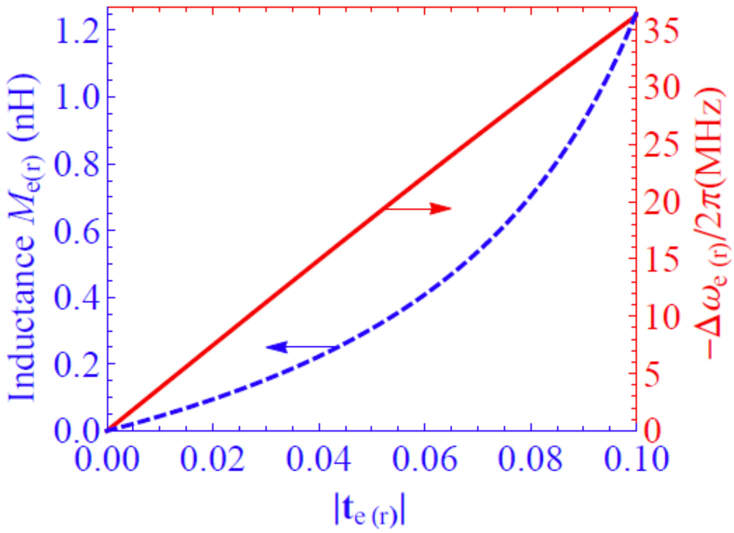

Figure 5.12: Red solid line: the resonator frequency detuning $-\Delta\omega_{\mathrm{e(r)}}/2\pi$ caused by changing $|\mathbf{t}_{\mathrm{e(r)}}|$ for a particular set of parameters of the coupler (see text). Blue dashed line: the corresponding value of the coupler mutual inductance $M_{\mathrm{e(r)}}$. The arrows indicate the corresponding vertical axes.

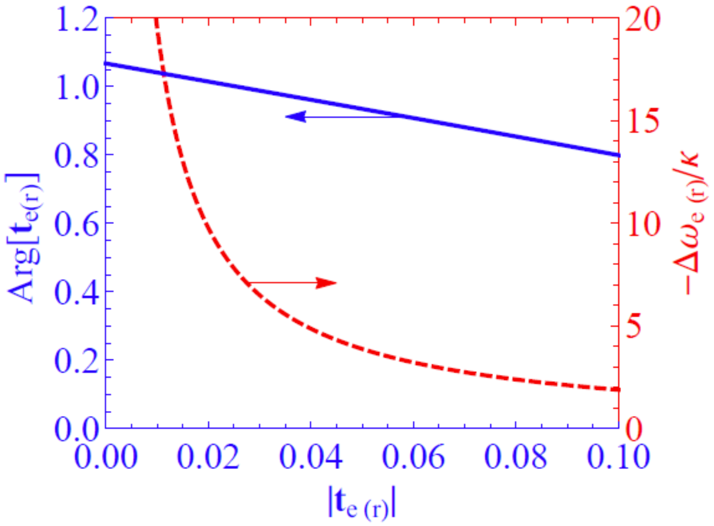

Figure 5.13: Solid line: the phase of the transmission amplitude, $\arg(\mathbf{t}_{\mathrm{e(r)}})$, as a function of its absolute value $|\mathbf{t}_{\mathrm{e(r)}}|$ for a particular set of coupler parameters (see text). Dashed line: the normalized detuning $-\Delta\omega_{\mathrm{e(r)}}/\kappa_{\mathrm{e(r)}} = -\pi\Delta\omega_{\mathrm{e(r)}}/\omega_{\mathrm{e(r)}}|\mathbf{t}_{\mathrm{e(r)}}|^2$.

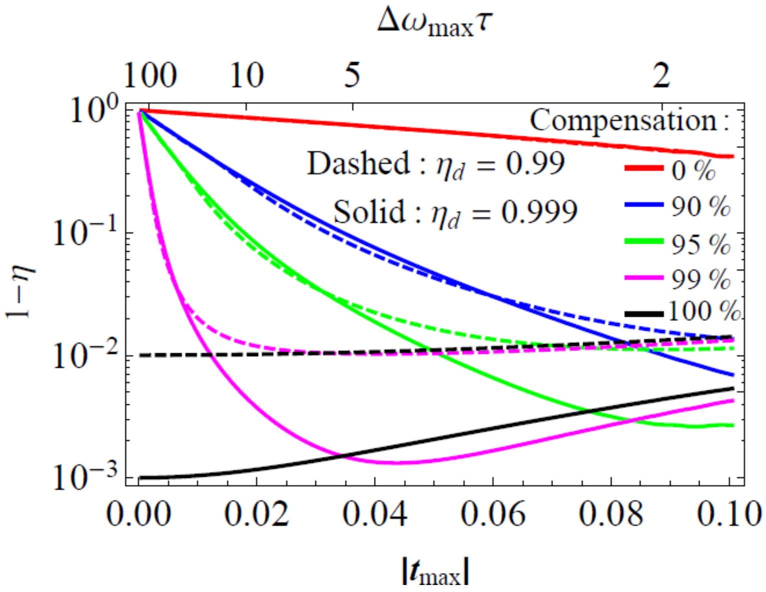

Figure 5.14: Inefficiency $1-\eta$ as a function of $|\mathbf{t}_{\mathrm{e,max}}| = |\mathbf{t}_{\mathrm{r,max}}|$ for the couplers with parameters described in the text. The solid lines are for the design efficiency $\eta_{\mathrm{d}} = 0.999$, while the dashed lines are for $\eta_{\mathrm{d}} = 0.99$. The red lines show the results without compensation of the frequency detuning $\Delta\omega_{\mathrm{e(r)}}(t)$ caused by changing $|\mathbf{t}_{\mathrm{e(r)}}(t)|$ and correspondingly changing $\arg(\mathbf{r}^{\mathrm{in}}_{\mathrm{e(t)}})$. The blue lines assume 90% compensation of this detuning, 95% compensation for the green lines, 99% compensation for the magenta lines, and full 100% compensation for the black lines. For the black lines the extra inefficiency is caused only by changing phases of $\mathbf{t}_{\mathrm{e(r)}}$. The upper horizontal axis shows the product $\Delta\omega_{\max}\tau$, corresponding to $|\mathbf{t}_{\max}|$.

Chapter 6

Conclusion

In this thesis, we studied theoretically the transmon-resonator system that is currently the most promising setup for superconducting qubits. We introduced dressed coherent states to describe the state that results from, for instance, applying a microwave drive to the resonator. In addition, we considered the transmon as a multi-level quantum system and analyzed the consequences of this model. On the practical side, we proposed a new measurement scheme which has the advantages of protecting the qubit from the Purcell effect, fast realization, and small measurement error. We also analyzed the performance of a protocol for quantum information transfer, which is a necessary feature of quantum networks.

In Chapter 1, we briefly outlined the field of quantum computing as a motivation for the present work. In Chapter 2, we discussed some aspects of superconducting qubits: Josephson junctions, transmon qubits, the Jaynes-Cummings model and dispersive readout of qubits in cQED setups, and the Purcell effect.

In Chapter 3, we proposed a novel measurement technique that utilizes the tunability of both the qubit frequency and the resonator coupling to the outgoing transmission line in order to isolate and protect the qubit from the Purcell effect. This fast and high-fidelity readout was accomplished by the controlled capture, dispersion, and release of microwave photons. We showed that, if the qubit frequency tuning is sufficiently adiabatic, readout is possible even in the strongly nonlinear dispersive regime. We also showed that the Jaynes-Cummings nonlinearity leads to self-developing field squeezing, which results in a significant reduction of the measurement error and may be useful as a tool to beat the standard quantum limit.

In Chapter 4, we generalized the dressed coherent states employed in Chapter 3 (where the qubit was assumed to be a two-level system) to also include higher energy levels of transmon qubits. Using these new dressed coherent states, we found that applying a microwave drive to the system leads to a stray population in the non-target qubit levels. We developed a qualitative and analytical understanding of such deviations and concluded that they were small and unnecessary to account for in experiments at present.

In Chapter 5, we examined the state-of-the-art protocol for the transfer of quantum states from one superconducting resonator to another along a transmission line. A number of parameter variations were considered to test the protocol under nonideal conditions, and the resulting inefficiencies were analyzed. We found that the protocol is surprisingly robust against all tested imperfections, except those involving frequency mismatch between the two resonators. A scheme to compensate for one source of frequency mismatch was proposed; without this compensation, any meaningful state transfer is impossible.

We hope that the novel ideas presented in this dissertation can advance the field of quantum computing based on superconducting circuits towards its ultimate goal: the realization of a quantum computer.

Bibliography

[1] M. A. Nielsen and I. L. Chuang, *Quantum Computation and Quantum Information.* Cambridge University Press, 2000.

[2] R. Feynman and P. W. Shor, “Simulating physics with computers,” *SIAM J. Comput.*, vol. 26, pp. 1484–1509, 1982.

[3] D. Deutsch, “Quantum theory, the church-turing principle and the universal quantum computer,” *Proc. R. Soc. A*, vol. 400, no. 1818, pp. 97–117, 1985.

[4] D. Deutsch and R. Jozsa, “Rapid solution of problems by quantum computation,” *Proc. R. Soc. A*, vol. 439, no. 1907, pp. 553–558, 1992.

[5] P. W. Shor, “Algorithms for quantum computation: discrete logarithms and factoring,” in *Proceedings, 35th Annual Symposium on Foundations of Computer Science*, pp. 124–134, 1994.

[6] C. Bennett, F. Bessette, G. Brassard, L. Salvail, and J. Smolin, “Experimental quantum cryptography,” *J. Cryptology*, vol. 5, pp. 3–28, 1992.

[7] L. K. Grover, “A fast quantum mechanical algorithm for database search,” *arXiv:quant-ph/9605043.*

[8] W. Heisenberg, *The physical principles of the quantum theory.* Dover Books on Physics and Chemistry, Dover Publications Incorporated, 1949.

[9] J. S. Bell, “On the einstein-podolsky-rosen paradox,” *Physics*, vol. 1, no. 3, pp. 195–200, 1964.

[10] A. N. Korotkov, “Nonideal quantum detectors in bayesian formalism,” *Phys. Rev. B*, vol. 67, p. 235408, Jun 2003.

[11] U. Fano, “Description of states in quantum mechanics by density matrix and operator techniques,” *Rev. Mod. Phys.*, vol. 29, pp. 74–93, Jan 1957.

[12] A. Barenco, C. H. Bennett, R. Cleve, D. P. DiVincenzo, N. Margolus, P. W. Shor, T. Sleator, J. A. Smolin, and H. Weinfurter, “Elementary gates for quantum computation,” *Phys. Rev. A*, vol. 52, pp. 3457–3467, Nov 1995.

[13] D. P. DiVincenzo, "Topics in quantum computers," in *Mesoscopic Electron Transport* (L. L. Sohn, L. P. Kouwenhoven, and G. Schon, eds.), vol. 345 of *NATO Advanced Study Institute, Series E: Applied Sciences*, Springer Netherlands, 1997.

[14] D. P. DiVincenzo, "The physical implementation of quantum computation," *Fortschr. Phys.*, vol. 48, no. 9-11, pp. 771–783, 2000.

[15] T. D. Ladd, F. Jelezko, R. Laflamme, Y. Nakamura, C. Monroe, and J. L. OBrien, "Quantum computers," *Nature*, vol. 464, no. 7285, pp. 45–53, 2010.

[16] D. G. Cory, A. F. Fahmy, and T. F. Havel, "Ensemble quantum computing by nmrspectroscopy," *Proc. Natl. Acad. Sci. U.S.A.*, vol. 94, no. 5, pp. 1634–1639, 1997.

[17] N. A. Gershenfeld and I. L. Chuang, "Bulk spin-resonance quantum computation," *Science*, vol. 275, no. 5298, pp. 350–356, 1997.

[18] D. G. Cory, M. D. Price, W. Maas, E. Knill, R. Laflamme, W. H. Zurek, T. F. Havel, and S. S. Somaroo, "Experimental quantum error correction," *Phys. Rev. Lett.*, vol. 81, pp. 2152–2155, Sep 1998.

[19] J. A. Jones and M. Mosca, "Implementation of a quantum algorithm on a nuclear magnetic resonance quantum computer," *J. Chem. Phys.*, vol. 109, no. 5, pp. 1648–1653, 1998.

[20] Y. S. Weinstein, M. A. Pravia, E. M. Fortunato, S. Lloyd, and D. G. Cory, "Implementation of the quantum fourier transform," *Phys. Rev. Lett.*, vol. 86, pp. 1889–1891, Feb 2001.

[21] L. M. Vandersypen, M. Steffen, G. Breyta, C. S. Yannoni, M. H. Sherwood, and I. L. Chuang, "Experimental realization of shor's quantum factoring algorithm using nuclear magnetic resonance," *Nature*, vol. 414, no. 6866, pp. 883–887, 2001.

[22] J. A. Jones, "Quantum computing and nuclear magnetic resonance," *PhysChemComm*, vol. 4, no. 11, pp. 49–56, 2001.

[23] C. Negrevergne, T. S. Mahesh, C. A. Ryan, M. Ditty, F. Cyr-Racine, W. Power, N. Boulant, T. Havel, D. G. Cory, and R. Laflamme, "Benchmarking quantum control methods on a 12-qubit system," *Phys. Rev. Lett.*, vol. 96, p. 170501, May 2006.

[24] C. Monroe and J. Kim, "Scaling the ion trap quantum processor," *Science*, vol. 339, no. 6124, pp. 1164–1169, 2013.

[25] D. J. Wineland, C. Monroe, W. M. Itano, D. Leibfried, B. E. King, and D. M. Meekhof, "Entangled states of trapped atomic ions," *J. Res. Natl. Inst. Stand. Technol.*, vol. 103, pp. 259–328, 1998.

[26] C. R. Monroe and D. J. Wineland, "Quantum computing with ions," *Sci. Am.*, vol. 299, no. 2, pp. 64–71, 2008.

[27] R. Blatt and D. Wineland, "Entangled states of trapped atomic ions," *Nature*, vol. 453, no. 7198, pp. 1008–1015, 2008.

[28] D. Leibfried, R. Blatt, C. Monroe, and D. Wineland, "Quantum dynamics of single trapped ions," *Rev. Mod. Phys.*, vol. 75, pp. 281–324, Mar 2003.

[29] J. Benhelm, G. Kirchmair, C. F. Roos, and R. Blatt, "Towards fault-tolerant quantum computing with trapped ions," *Nature Phys.*, vol. 4, no. 6, pp. 463–466, 2008.

[30] J. I. Cirac and P. Zoller, "Goals and opportunities in quantum simulation," *Nature Phys.*, vol. 8, no. 4, pp. 264–266, 2012.

[31] D. Kielpinski, C. Monroe, and D. J. Wineland, "Architecture for a large-scale ion-trap quantum computer," *Nature*, vol. 417, no. 6890, pp. 709–711, 2002.

[32] O. Morsch and M. Oberthaler, "Dynamics of bose-einstein condensates in optical lattices," *Rev. Mod. Phys.*, vol. 78, pp. 179–215, Feb 2006.

[33] J. L. OBrien, G. J. Pryde, A. G. White, T. C. Ralph, and D. Branning, "Demonstration of an all-optical quantum controlled-not gate," *Nature*, vol. 426, no. 6964, pp. 264–267, 2003.

[34] P. Grangier, B. Sanders, and J. Vuckovic, "Focus on single photons on demand," *New J. Phys.*, vol. 6, no. 1, 2004.

[35] A. J. Shields, "Semiconductor quantum light sources," *Nat. photon.*, vol. 1, no. 4, pp. 215–223, 2007.

[36] A. Migdall and J. Dowling, "Introduction to the journal of modern optics special issue on single-photon: Detectors, applications, and measurement methods," tech. rep., DTIC Document, 2004.

[37] R. H. Hadfield, "Single-photon detectors for optical quantum information applications," *Nat. Photon.*, vol. 3, no. 12, pp. 696–705, 2009.

[38] L.-M. Duan and H. J. Kimble, "Scalable photonic quantum computation through cavity-assisted interactions," *Phys. Rev. Lett.*, vol. 92, p. 127902, Mar 2004.

[39] A. Blais, R.-S. Huang, A. Wallraff, S. M. Girvin, and R. J. Schoelkopf, "Cavity quantum electrodynamics for superconducting electrical circuits: An architecture for quantum computation," *Phys. Rev. A*, vol. 69, p. 062320, Jun 2004.

[40] D. Loss and D. P. DiVincenzo, "Quantum computation with quantum dots," *Phys. Rev. A*, vol. 57, pp. 120–126, Jan 1998.

[41] D. D. Awschalom, L. C. Bassett, A. S. Dzurak, E. L. Hu, and J. R. Petta, "Quantum spintronics: engineering and manipulating atom-like spins in semiconductors," *Science*, vol. 339, no. 6124, pp. 1174–1179, 2013.

[42] H. Kimble, "The quantum internet," *Nature*, vol. 453, no. 7198, pp. 1023–1030, 2008.

[43] A. M. Tyryshkin, S. Tojo, J. J. Morton, H. Riemann, N. V. Abrosimov, P. Becker, H.-J. Pohl, T. Schenkel, M. L. Thewalt, K. M. Itoh, *et al.*, "Electron spin coherence exceeding seconds in high-purity silicon," *Nat. Mater.*, vol. 11, no. 2, pp. 143–147, 2011.

[44] M. Steger, K. Saeedi, M. Thewalt, J. Morton, H. Riemann, N. Abrosimov, P. Becker, and H.-J. Pohl, "Quantum information storage for over 180 s using donor spins in a 28si semiconductor vacuum," *Science*, vol. 336, no. 6086, pp. 1280–1283, 2012.

[45] J. Bardeen, L. N. Cooper, and J. R. Schrieffer, "Microscopic theory of superconductivity," *Phys. Rev.*, vol. 106, pp. 162–164, Apr 1957.

[46] J. Bardeen, L. N. Cooper, and J. R. Schrieffer, "Theory of superconductivity," *Phys. Rev.*, vol. 108, pp. 1175–1204, Dec 1957.

[47] E. Maxwell, "Isotope effect in the superconductivity of mercury," *Phys. Rev.*, vol. 78, pp. 477–477, May 1950.

[48] C. A. Reynolds, B. Serin, W. H. Wright, and L. B. Nesbitt, "Superconductivity of isotopes of mercury," *Phys. Rev.*, vol. 78, pp. 487–487, May 1950.

[49] D. J. Griffiths, *Introduction to electrodynamics*, vol. 3. Prentice Hall New Jersey, 1999.

[50] B. D. Josephson, "Possible new effects in superconductive tunnelling," *Phys. Lett.*, vol. 1, pp. 251–253, 1962.

[51] B. D. Josephson, "The discovery of tunnelling supercurrents," *Rev. Mod. Phys.*, vol. 46, pp. 251–254, Apr 1974.

[52] Y. Makhlin, G. Schön, and A. Shnirman, "Quantum-state engineering with josephson-junction devices," *Rev. Mod. Phys.*, vol. 73, pp. 357–400, May 2001.

[53] J. Clarke and F. K. Wilhelm, "Superconducting quantum bits," *Nature*, vol. 453, no. 7198, pp. 1031–1042, 2008.

[54] Y. Nakamura, Y. A. Pashkin, and J. Tsai, "Coherent control of macroscopic quantum states in a single-cooper-pair box," *Nature*, vol. 398, no. 6730, pp. 786–788, 1999.

[55] M. H. Devoret and R. J. Schoelkopf, "Amplifying quantum signals with the single-electron transistor," *Nature*, vol. 406, no. 6799, pp. 1039–1046, 2000.

[56] J. Koch, T. M. Yu, J. Gambetta, A. A. Houck, D. I. Schuster, J. Majer, A. Blais, M. H. Devoret, S. M. Girvin, and R. J. Schoelkopf, "Charge-insensitive qubit design derived from the cooper pair box," *Phys. Rev. A*, vol. 76, p. 042319, Oct 2007.

[57] C. Hood, T. Lynn, A. Doherty, A. Parkins, and H. Kimble, "The atom-cavity microscope: single atoms bound in orbit by single photons," *Science*, vol. 287, no. 5457, pp. 1447–1453, 2000.

[58] M. D. Reed, B. Johnson, A. Houck, L. DiCarlo, J. Chow, D. Schuster, L. Frunzio, and R. Schoelkopf, "Fast reset and suppressing spontaneous emission of a superconducting qubit," *Appl. Phys. Lett.*, vol. 96, no. 20, pp. 203110–203110–3, 2010.

[59] E. A. Sete, J. M. Gambetta, and A. N. Korotkov, "Purcell effect with microwave drive: Suppression of qubit relaxation rate," *Phys. Rev. B*, vol. 89, p. 104516, Mar 2014.

[60] E. Jeffrey, D. Sank, J. Y. Mutus, T. C. White, J. Kelly, R. Barends, Y. Chen, Z. Chen, B. Chiaro, A. Dunsworth, A. Megrant, P. J. J. O'Malley, C. Neill, P. Roushan, A. Vainsencher, J. Wenner, A. N. Cleland, and J. M. Martinis, "Fast accurate state measurement with superconducting qubits," *Phys. Rev. Lett.*, vol. 112, p. 190504, May 2014.

[61] E. A. Sete, J. M. Martinis, and A. N. Korotkov, "Quantum theory of a bandpass purcell filter for qubit readout," *Phys. Rev. A*, vol. 92, p. 012325, Jul 2015.

[62] E. M. Purcell, H. C. Torrey, and R. V. Pound, "Resonance absorption by nuclear magnetic moments in a solid," *Phys. Rev.*, vol. 69, pp. 37–38, Jan 1946.

[63] J. M. Gambetta, A. A. Houck, and A. Blais, "Superconducting qubit with purcell protection and tunable coupling," *Phys. Rev. Lett.*, vol. 106, p. 030502, Jan 2011.

[64] H. Paik, D. I. Schuster, L. S. Bishop, G. Kirchmair, G. Catelani, A. P. Sears, B. R. Johnson, M. J. Reagor, L. Frunzio, L. I. Glazman, S. M. Girvin, M. H. Devoret, and R. J. Schoelkopf, "Observation of high coherence in josephson junction qubits measured in a three-dimensional circuit qed architecture," *Phys. Rev. Lett.*, vol. 107, p. 240501, Dec 2011.

[65] L. S. Bishop, E. Ginossar, and S. M. Girvin, "Response of the strongly driven jaynes-cummings oscillator," *Phys. Rev. Lett.*, vol. 105, p. 100505, Sep 2010.

[66] M. Boissonneault, J. M. Gambetta, and A. Blais, "Improved superconducting qubit readout by qubit-induced nonlinearities," *Phys. Rev. Lett.*, vol. 105, p. 100504, Sep 2010.

[67] F. Mallet, M. A. Castellanos-Beltran, H. S. Ku, S. Glancy, E. Knill, K. D. Irwin, G. C. Hilton, L. R. Vale, and K. W. Lehnert, "Quantum state tomography of an itinerant squeezed microwave field," *Phys. Rev. Lett.*, vol. 106, p. 220502, Jun 2011.

[68] L. C. G. Govia, E. J. Pritchett, and F. K. Wilhelm, "Generating nonclassical states from classical radiation by subtraction measurements," *New J. Phys.*, vol. 16, no. 4, p. 045011, 2014.

[69] P. Campagne-Ibarcq, E. Flurin, N. Roch, D. Darson, P. Morfin, M. Mirrahimi, M. H. Devoret, F. Mallet, and B. Huard, "Persistent control of a superconducting qubit by stroboscopic measurement feedback," *Phys. Rev. X*, vol. 3, p. 021008, May 2013.

[70] A. N. Korotkov, "Quantum bayesian approach to circuit qed measurement," *arXiv:1111.4016.*

[71] H. M. Wiseman and G. J. Milburn, *Quantum Measurement and Control.* Cambridge University Press, Cambridge, 2010.

[72] M. O. Scully and M. S. Zubairy, *Quantum Optics.* Cambridge University Press, 1997.

[73] J. E. Johnson, C. Macklin, D. H. Slichter, R. Vijay, E. B. Weingarten, J. Clarke, and I. Siddiqi, "Heralded state preparation in a superconducting qubit," *Phys. Rev. Lett.*, vol. 109, p. 050506, Aug 2012.

[74] D. Ristè, J. G. van Leeuwen, H.-S. Ku, K. W. Lehnert, and L. DiCarlo, "Initialization by measurement of a superconducting quantum bit circuit," *Phys. Rev. Lett.*, vol. 109, p. 050507, Aug 2012.

[75] A. Galiautdinov, A. N. Korotkov, and J. M. Martinis, "Resonator˘zero-qubit architecture for superconducting qubits," *Phys. Rev. A*, vol. 85, p. 042321, Apr 2012.

[76] E. A. Sete, A. Galiautdinov, E. Mlinar, J. M. Martinis, and A. N. Korotkov, "Catch-disperse-release readout for superconducting qubits," *Phys. Rev. Lett.*, vol. 110, p. 210501, May 2013.

[77] V. B. Braginsky, F. Y. Khalili, and K. S. Thorne, *Quantum measurement.* Cambridge University Press, 1995.

[78] A. G. Fowler, M. Mariantoni, J. M. Martinis, and A. N. Cleland, "Surface codes: Towards practical large-scale quantum computation," *Phys. Rev. A*, vol. 86, p. 032324, Sep 2012.

[79] M. Boissonneault, J. M. Gambetta, and A. Blais, "Dispersive regime of circuit qed: Photon-dependent qubit dephasing and relaxation rates," *Phys. Rev. A*, vol. 79, p. 013819, Jan 2009.

[80] A. Wallraff, D. I. Schuster, A. Blais, L. Frunzio, R.-S. Huang, S. Kumar, S. M. Girvin, and R. J. Schoelkopf, "Strong coupling of a single photon to a superconducting qubit using circuit quantum electrodynamics," *Nature*, vol. 431, no. 7005, pp. 162–167, 2004.

[81] J. A. Schreier, A. A. Houck, J. Koch, D. I. Schuster, B. R. Johnson, J. M. Chow, J. M. Gambetta, J. Majer, L. Frunzio, M. H. Devoret, S. M. Girvin, and R. J. Schoelkopf, "Suppressing charge noise decoherence in superconducting charge qubits," *Phys. Rev. B*, vol. 77, p. 180502, May 2008.

[82] R. Barends, J. Kelly, A. Megrant, D. Sank, E. Jeffrey, Y. Chen, Y. Yin, B. Chiaro, J. Mutus, C. Neill, P. O'Malley, P. Roushan, J. Wenner, T. C. White, A. N. Cleland, and J. M. Martinis, "Coherent josephson qubit suitable for scalable quantum integrated circuits," *Phys. Rev. Lett.*, vol. 111, p. 080502, Aug 2013.

[83] G. de Lange, B. van Heck, A. Bruno, D. J. van Woerkom, A. Geresdi, S. R. Plissard, E. P. A. M. Bakkers, A. R. Akhmerov, and L. DiCarlo, "Realization of microwave quantum circuits using hybrid superconducting-semiconducting nanowire josephson elements," *Phys. Rev. Lett.*, vol. 115, p. 127002, Sep 2015.

[84] T. W. Larsen, K. D. Petersson, F. Kuemmeth, T. S. Jespersen, P. Krogstrup, J. Nygård, and C. M. Marcus, "Semiconductor-nanowire-based superconducting qubit," *Phys. Rev. Lett.*, vol. 115, p. 127001, Sep 2015.

[85] K. W. Murch, S. J. Weber, C. Macklin, and I. Siddiqi, "Observing single quantum trajectories of a superconducting quantum bit," *Nature*, vol. 502, no. 7470, pp. 211–214, 2013.

[86] J. M. Chow, J. M. Gambetta, A. D. Córcoles, S. T. Merkel, J. A. Smolin, C. Rigetti, S. Poletto, G. A. Keefe, M. B. Rothwell, J. R. Rozen, M. B. Ketchen, and M. Steffen, "Universal quantum gate set approaching fault-tolerant thresholds with superconducting qubits," *Phys. Rev. Lett.*, vol. 109, p. 060501, Aug 2012.

[87] R. Barends, J. Kelly, A. Megrant, A. Veitia, D. Sank, E. Jeffrey, T. C. White, J. Mutus, A. G. Fowler, B. Campbell, Y. Chen, Z. Chen, B. Chiaro, A. Dunsworth, C. Neill, P. O/'Malley, P. Roushan, A. Vainsencher, J. Wenner, A. N. Korotkov, A. N. Cleland, and J. M. Martinis, "Strong coupling of a single photon to a superconducting qubit using circuit quantum electrodynamics," *Nature*, vol. 508, no. 7497, pp. 500–503, 2014.

[88] J. M. Chow, J. M. Gambetta, E. Magesan, D. W. Abraham, A. W. Cross, B. R. Johnson, N. A. Masluk, C. A. Ryan, J. A. Smolin, S. J. Srinivasan, and M. Steffen, "Universal quantum gate set approaching fault-tolerant thresholds with superconducting qubits," *Nat. Commun.*, vol. 5, no. 4015, 2014.

[89] R. Vijay, D. H. Slichter, and I. Siddiqi, "Observation of quantum jumps in a superconducting artificial atom," *Phys. Rev. Lett.*, vol. 106, p. 110502, Mar 2011.

[90] A. Wallraff, D. I. Schuster, A. Blais, L. Frunzio, R.-S. Huang, S. Kumar, S. M. Girvin, and R. J. Schoelkopf, "Strong coupling of a single photon to a superconducting qubit using circuit quantum electrodynamics," *Nature*, vol. 482, no. 7385, pp. 382–385, 2012.

[91] J. Kelly, R. Barends, A. G. Fowler, A. Megrant, E. Jeffrey, T. C. White, D. Sank, J. Y. Mutus, B. Campbell, Y. Chen, Z. Chen, B. Chiaro, A. Dunsworth, I.-C. Hoi, C. Neill, P. J. J. O/'Malley, C. Quintana, P. Roushan, A. Vainsencher, J. Wenner, A. N. Cleland, and J. M. Martinis, "State preservation by repetitive error detection in a superconducting quantum circuit," *Nature*, vol. 519, no. 7541, pp. 66–69, 2015.

[92] A. Córcoles, E. Magesan, S. J. Srinivasan, A. W. Cross, M. Steffen, J. M. Gambetta, and J. M. Chow, "Demonstration of a quantum error detection code using a square lattice of four superconducting qubits," *Nat. Commun.*, vol. 6, no. 6979, 2015.

[93] D. Ristè, S. Poletto, M.-Z. Huang, A. Bruno, V. Vesterinen, O.-P. Saira, and L. DiCarlo, "Detecting bit-flip errors in a logical qubit using stabilizer measurements," *Nat. Commun.*, vol. 6, no. 6983, 2015.

[94] J. Gambetta, A. Blais, D. I. Schuster, A. Wallraff, L. Frunzio, J. Majer, M. H. Devoret, S. M. Girvin, and R. J. Schoelkopf, "Qubit-photon interactions in a cavity: Measurement-induced dephasing and number splitting," *Phys. Rev. A*, vol. 74, p. 042318, Oct 2006.

[95] M. Boissonneault, J. M. Gambetta, and A. Blais, "Nonlinear dispersive regime of cavity qed: The dressed dephasing model," *Phys. Rev. A*, vol. 77, p. 060305, Jun 2008.

[96] D. H. Slichter, C. Mller, R. Vijay, S. J. Weber, A. Blais, and I. Siddiqi, "Quantum zeno effect in the strong measurement regime of circuit quantum electrodynamics," *New J. Phys.*, vol. 18, no. 5, p. 053031, 2016.

[97] C. C. Bultink, M. A. Rol, T. E. O'Brien, X. Fu, B. C. S. Dikken, C. Dickel, R. F. L. Vermeulen, J. C. de Sterke, A. Bruno, R. N. Schouten, and L. DiCarlo, "Active resonator reset in the nonlinear dispersive regime of circuit qed," *Phys. Rev. Applied*, vol. 6, p. 034008, Sep 2016.

[98] D. Sank, Z. Chen, M. Khezri, J. Kelly, R. Barends, B. Campbell, Y. Chen, B. Chiaro, A. Dunsworth, A. Fowler, E. Jeffrey, E. Lucero, A. Megrant, J. Mutus, M. Neeley, C. Neill, P. J. J. O'Malley, C. Quintana, P. Roushan, A. Vainsencher, T. White, J. Wenner, A. N. Korotkov, and J. M. Martinis, "Measurement-induced state transitions in a superconducting qubit: Beyond

the rotating wave approximation," *Phys. Rev. Lett.*, vol. 117, p. 190503, Nov 2016.

[99] L. C. G. Govia and F. K. Wilhelm, "Entanglement generated by the dispersive interaction: The dressed coherent state," *Phys. Rev. A*, vol. 93, p. 012316, Jan 2016.

[100] L. C. G. Govia, E. J. Pritchett, C. Xu, B. L. T. Plourde, M. G. Vavilov, F. K. Wilhelm, and R. McDermott, "High-fidelity qubit measurement with a microwave-photon counter," *Phys. Rev. A*, vol. 90, p. 062307, Dec 2014.

[101] Y.-F. Chen, D. Hover, S. Sendelbach, L. Maurer, S. T. Merkel, E. J. Pritchett, F. K. Wilhelm, and R. McDermott, "Microwave photon counter based on josephson junctions," *Phys. Rev. Lett.*, vol. 107, p. 217401, Nov 2011.

[102] M. H. Devoret, A. Wallraff, and J. M. Martinis, "Superconducting qubits: A short review," *arXiv:cond-mat/0411174*.

[103] E. T. Jaynes and F. W. Cummings, "Comparison of quantum and semiclassical radiation theories with application to the beam maser," *Proc. IEEE*, vol. 51, no. 1, pp. 89–109, 1963.

[104] A. W. Cross and J. M. Gambetta, "Optimized pulse shapes for a resonator-induced phase gate," *Phys. Rev. A*, vol. 91, p. 032325, Mar 2015.

[105] M. Khezri, E. Mlinar, J. Dressel, and A. N. Korotkov, "Measuring a transmon qubit in circuit qed: Dressed squeezed states," *Phys. Rev. A*, vol. 94, p. 012347, Jul 2016.

[106] Y. Yin, Y. Chen, D. Sank, P. J. J. O'Malley, T. C. White, R. Barends, J. Kelly, E. Lucero, M. Mariantoni, A. Megrant, C. Neill, A. Vainsencher, J. Wenner, A. N. Korotkov, A. N. Cleland, and J. M. Martinis, "Catch and release of microwave photon states," *Phys. Rev. Lett.*, vol. 110, p. 107001, Mar 2013.

[107] J. Wenner, Y. Yin, Y. Chen, R. Barends, B. Chiaro, E. Jeffrey, J. Kelly, A. Megrant, J. Y. Mutus, C. Neill, P. J. J. O'Malley, P. Roushan, D. Sank, A. Vainsencher, T. C. White, A. N. Korotkov, A. N. Cleland, and J. M. Martinis, "Catching time-reversed microwave coherent state photons with 99.4May 2014.

[108] J. I. Cirac, P. Zoller, H. J. Kimble, and H. Mabuchi, "Quantum state transfer and entanglement distribution among distant nodes in a quantum network," *Phys. Rev. Lett.*, vol. 78, pp. 3221–3224, Apr 1997.

[109] S. L. Braunstein and H. J. Kimble, "Teleportation of continuous quantum variables," *Phys. Rev. Lett.*, vol. 80, pp. 869–872, Jan 1998.

[110] A. Furusawa, J. L. Sørensen, S. L. Braunstein, C. A. Fuchs, H. J. Kimble, and E. S. Polzik, "Unconditional quantum teleportation," *Science*, vol. 282, no. 5389, pp. 706–709, 1998.

[111] S. Lloyd, M. S. Shahriar, J. H. Shapiro, and P. R. Hemmer, "Long distance, unconditional teleportation of atomic states via complete bell state measurements," *Phys. Rev. Lett.*, vol. 87, p. 167903, Sep 2001.

[112] L.-M. Duan, M. D. Lukin, J. I. Cirac, and P. Zoller, "Long-distance quantum communication with atomic ensembles and linear optics," *Nature*, vol. 414, no. 6862, pp. 413–418, 2001.

[113] M. D. Lukin, "*Colloquium* : Trapping and manipulating photon states in atomic ensembles," *Rev. Mod. Phys.*, vol. 75, pp. 457–472, Apr 2003.

[114] C. Chou, H. de Riedmatten, D. Felinto, S. Polyakov, S. van Enk, and H. Kimble, "Measurement-induced entanglement for excitation stored in remote atomic ensembles," *Nature*, vol. 438, p. 828, 2005.

[115] M. Razavi and J. H. Shapiro, "Long-distance quantum communication with neutral atoms," *Phys. Rev. A*, vol. 73, no. 4, p. 042303, 2006.

[116] S. Ritter, C. Nölleke, C. Hahn, A. Reiserer, A. Neuzner, M. Uphoff, M. Mücke, E. Figueroa, J. Bochmann, and G. Rempe, "An elementary quantum network of single atoms in optical cavities," *Nature*, vol. 484, no. 7393, pp. 195–200, 2012.

[117] A. Stute, B. Casabone, B. Brandstätter, K. Friebe, T. Northup, and R. Blatt, "Quantum-state transfer from an ion to a photon," *Nat. photon.*, vol. 7, no. 3, pp. 219–222, 2013.

[118] K. Jahne, B. Yurke, and U. Gavish, "High-fidelity transfer of an arbitrary quantum state between harmonic oscillators," *Phys. Rev. A*, vol. 75, p. 010301, Jan 2007.

[119] A. N. Korotkov, "Flying microwave qubits with nearly perfect transfer efficiency," *Phys. Rev. B*, vol. 84, p. 014510, Jul 2011.

[120] T. Hime, P. A. Reichardt, B. L. T. Plourde, T. L. Robertson, C.-E. Wu, A. V. Ustinov, and J. Clarke, "Solid-state qubits with current-controlled coupling," *Science*, vol. 314, no. 5804, pp. 1427–1429, 2006.

[121] A. O. Niskanen, K. Harrabi, F. Yoshihara, Y. Nakamura, S. Lloyd, and J. S. Tsai, "Quantum coherent tunable coupling of superconducting qubits," *Science*, vol. 316, no. 5825, pp. 723–726, 2007.

[122] M. S. Allman, F. Altomare, J. D. Whittaker, K. Cicak, D. Li, A. Sirois, J. Strong, J. D. Teufel, and R. W. Simmonds, "rf-squid-mediated coherent tunable coupling between a superconducting phase qubit and a lumped-element resonator," *Phys. Rev. Lett.*, vol. 104, p. 177004, Apr 2010.

[123] R. C. Bialczak, M. Ansmann, M. Hofheinz, M. Lenander, E. Lucero, M. Neeley, A. D. O'Connell, D. Sank, H. Wang, M. Weides, J. Wenner, T. Yamamoto, A. N. Cleland, and J. M. Martinis, "Fast tunable coupler for superconducting qubits," *Phys. Rev. Lett.*, vol. 106, p. 060501, Feb 2011.

[124] A. J. Hoffman, S. J. Srinivasan, J. M. Gambetta, and A. A. Houck, "Coherent control of a superconducting qubit with dynamically tunable qubit-cavity coupling," *Phys. Rev. B*, vol. 84, p. 184515, Nov 2011.

[125] S. J. Srinivasan, N. M. Sundaresan, D. Sadri, Y. Liu, J. M. Gambetta, T. Yu, S. M. Girvin, and A. A. Houck, "Time-reversal symmetrization of spontaneous emission for quantum state transfer," *Phys. Rev. A*, vol. 89, p. 033857, Mar 2014.

[126] Y. Chen, C. Neill, P. Roushan, N. Leung, M. Fang, R. Barends, J. Kelly, B. Campbell, Z. Chen, B. Chiaro, A. Dunsworth, E. Jeffrey, A. Megrant, J. Y. Mutus, P. J. J. O'Malley, C. M. Quintana, D. Sank, A. Vainsencher, J. Wenner, T. C. White, M. R. Geller, A. N. Cleland, and J. M. Martinis, "Qubit architecture with high coherence and fast tunable coupling," *Phys. Rev. Lett.*, vol. 113, p. 220502, Nov 2014.

[127] J. D. Whittaker, F. C. S. da Silva, M. S. Allman, F. Lecocq, K. Cicak, A. J. Sirois, J. D. Teufel, J. Aumentado, and R. W. Simmonds, "Tunable-cavity qed with phase qubits," *Phys. Rev. B*, vol. 90, p. 024513, Jul 2014.

[128] M. Pierre, I.-M. Svensson, S. Raman Sathyamoorthy, G. Johansson, and P. Delsing, "Storage and on-demand release of microwaves using superconducting resonators with tunable coupling," *Appl. Phys. Lett.*, vol. 104, p. 232604, 2014.

[129] J. Q. You, Z. D. Wang, W. Zhang, and F. Nori, "Encoding a qubit with majorana modes in superconducting circuits," *Sci. Rep.*, vol. 4, 2014.

[130] S. J. Weber, A. Chantasri, J. Dressel, A. N. Jordan, K. W. Murch, and I. Siddiqi, "Mapping the optimal route between two quantum states," *Nature*, vol. 511, no. 7511, pp. 570–573, 2014.

[131] L. Sun, A. Petrenko, Z. Leghtas, B. Vlastakis, G. Kirchmair, K. M. Sliwa, A. Narla, M. Hatridge, S. Shankar, J. Blumoff, L. Frunzio, M. Mirrahimi, M. H. Devoret, and R. J. Schoelkopf, "Tracking photon jumps with repeated quantum non-demolition parity measurements," *Nature*, vol. 511, no. 7510, pp. 444–448, 2014.

[132] Z. Lin, K. Inomata, K. Koshino, W. Oliver, Y. Nakamura, J. Tsai, and T. Yamamoto, "Tracking photon jumps with repeated quantum non-demolition parity measurements," *Nat. Comm.*, vol. 5, no. 4480, 2014.

[133] M. Stern, G. Catelani, Y. Kubo, C. Grezes, A. Bienfait, D. Vion, D. Esteve, and P. Bertet, "Flux qubits with long coherence times for hybrid quantum circuits," *Phys. Rev. Lett.*, vol. 113, p. 123601, Sep 2014.

[134] L. Steffen, Y. Salathe, M. Oppliger, P. Kurpiers, M. Baur, C. Lang, C. Eichler, G. Puebla-Hellmann, A. Fedorov, and A. Wallraff, "Deterministic quantum teleportation with feed-forward in a solid state system," *Nature*, vol. 500, no. 7462, pp. 319–322, 2013.

[135] S. Gustavsson, O. Zwier, J. Bylander, F. Yan, F. Yoshihara, Y. Nakamura, T. P. Orlando, and W. D. Oliver, "Improving quantum gate fidelities by using a qubit to measure microwave pulse distortions," *Phys. Rev. Lett.*, vol. 110, p. 040502, Jan 2013.

[136] D. Riste, M. Dukalski, C. Watson, G. De Lange, M. Tiggelman, Y. M. Blanter, K. Lehnert, R. Schouten, and L. DiCarlo, "Deterministic entanglement of superconducting qubits by parity measurement and feedback," *Nature*, vol. 502, no. 7471, pp. 350–354, 2013.

[137] N. Roch, M. E. Schwartz, F. Motzoi, C. Macklin, R. Vijay, A. W. Eddins, A. N. Korotkov, K. B. Whaley, M. Sarovar, and I. Siddiqi, "Observation of measurement-induced entanglement and quantum trajectories of remote superconducting qubits," *Phys. Rev. Lett.*, vol. 112, p. 170501, Apr 2014.

[138] M. Pechal, L. Huthmacher, C. Eichler, S. Zeytinoğlu, A. A. Abdumalikov, S. Berger, A. Wallraff, and S. Filipp, "Microwave-controlled generation of shaped single photons in circuit quantum electrodynamics," *Phys. Rev. X*, vol. 4, p. 041010, Oct 2014.

[139] S. Zeytinoğlu, M. Pechal, S. Berger, A. A. Abdumalikov, A. Wallraff, and S. Filipp, "Microwave-induced amplitude- and phase-tunable qubit-resonator coupling in circuit quantum electrodynamics," *Phys. Rev. A*, vol. 91, p. 043846, Apr 2015.

[140] M. Keller, B. Lange, K. Hayasaka, W. Lange, and H. Walther, "Continuous generation of single photons with controlled waveform in an ion-trap cavity system," *Nature*, vol. 431, no. 7012, pp. 1075–1078, 2004.

[141] P. Kolchin, C. Belthangady, S. Du, G. Y. Yin, and S. E. Harris, "Electro-optic modulation of single photons," *Phys. Rev. Lett.*, vol. 101, p. 103601, Sep 2008.

[142] D. F. Walls and G. J. Milburn, *Quantum Optics.* Springer, Berlin, 2008.

[143] C. Gerry and P. Knight, *Introductory Quantum Optics.* Cambridge University Press, Cambridge, 2006.

[144] B. Yurke and J. S. Denker, "Quantum network theory," *Phys. Rev. A*, vol. 29, pp. 1419–1437, Mar 1984.

[145] M. A. Nielsen, "A simple formula for the average gate fidelity of a quantum dynamical operation," *Phys. Lett. A*, vol. 303, no. 4, pp. 249 – 252, 2002.

[146] M. Horodecki, P. Horodecki, and R. Horodecki, “General teleportation channel, singlet fraction, and quasidistillation,” *Phys. Rev. A*, vol. 60, pp. 1888–1898, Sep 1999.

[147] K. Keane and A. N. Korotkov, “Simplified quantum error detection and correction for superconducting qubits,” *Phys. Rev. A*, vol. 86, p. 012333, Jul 2012.

[148] M. Hofheinz, H. Wang, M. Ansmann, R. C. Bialczak, E. Lucero, M. Neeley, A. O’Connell, D. Sank, J. Wenner, J. M. Martinis, *et al.*, “Synthesizing arbitrary quantum states in a superconducting resonator,” *Nature*, vol. 459, no. 7246, pp. 546–549, 2009.

[149] M. Göppl, A. Fragner, M. Baur, R. Bianchetti, S. Filipp, J. M. Fink, P. J. Leek, G. Puebla, L. Steffen, and A. Wallraff, “Coplanar waveguide resonators for circuit quantum electrodynamics,” *J. Appl. Phys.*, vol. 104, no. 11, 2008.

Appendix A

Beam Splitter Approach to State Transfer Setup

In this Appendix we discuss the *quantum* theory of state transfer using the optical language of beam splitters. The starting point is Eq. (5.7), in which the resulting classical field $B(t_{\rm f})$ has the contribution $\sqrt{\eta}\, e^{i\varphi_{\rm f}}G(0)$ from the transferred field $G(0)$ and also contributions from other fields. This equation describes a unitary transformation, which can be modeled as a result of adding the (infinite number of) fields [$B(0)$ and time-binned $V(t)$] by using a system of (infinite number of) beam splitters. Then using linearity of the evolution, we can simply replace the classical fields with the corresponding annihilation operators for quantum fields, thus developing the quantum theory of the state transfer.

In the case when all other fields in Eq. (5.7) except $G(0)$ correspond to vacuum, it is sufficient to consider one beam splitter because a linear combination of vacua is still vacuum. This is why in this Appendix we mainly discuss one beam splitter

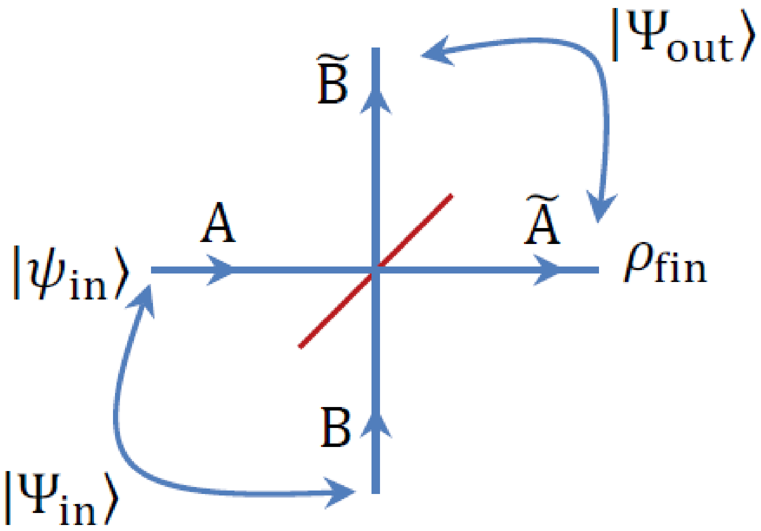

Figure A.1: A beam splitter with input classical fields A and B transformed into the output fields $\tilde{A}$ and $\tilde{B}$, with the main transformation $A \to \tilde{A}$ characterized by the amplitude $\sqrt{\eta}$ and phase shift $\varphi_{\rm f}$. In the quantum formulation the input state $|\Psi_{\rm in}\rangle$ is transformed into the output state $|\Psi_{\rm out}\rangle$. In particular, in Sec. A.1 we consider the input state $|\Psi_{\rm in}\rangle = |\psi_{\rm in}\rangle|0\rangle$, calculate $|\Psi_{\rm out}\rangle$, and then reduce it to the density matrix $\rho_{\rm fin}$ of the main output arm, by tracing over the other output arm.

(characterized by the amplitude $\sqrt{\eta}$ and phase $\varphi_{\rm f}$ in the main path), with the initial state to be transferred at one arm and vacuum state at the other arm. Note that notations in this Appendix are different from the notations in the main text.

Let us start with revisiting the quantum theory of a beam splitter [143] (Fig. A.1). The quantum theory follows the classical description of the beam splitter, which is characterized by the following relations between the input classical fields

A and B, and the output classical fields $\tilde{A}$ and $\tilde{B}$:

$$\tilde{A} = \sqrt{\eta}\, e^{i\varphi_1} A + \sqrt{1-\eta}\, e^{i\varphi_2} B, \tag{A.1}$$

$$\tilde{B} = \sqrt{\eta}\, e^{i\varphi_3} B - \sqrt{1-\eta}\, e^{i(\varphi_1-\varphi_2+\varphi_3)} A, \tag{A.2}$$

where $\varphi_1 = \varphi_{\rm f}$ and other phases are introduced to describe a general unitary transformation (these phases can include phase shifts in all four arms). Exactly the same relations also apply in the quantum case for the annihilation operators $\tilde{a}$ and $\tilde{b}$ of the fields at the output arms and the annihilation operators a and b of the fields at the input arms.

In general, we want to find an output quantum state $|\Psi_{\rm out}\rangle$ for a given input state $|\Psi_{\rm in}\rangle$, which in principle can be an entangled state of the two input modes. This can be done [143] by applying the following steps:

1. Express the input state $|\Psi_{\rm in}\rangle$ in terms of the input creation operators $a^\dagger$ and $b^\dagger$, and vacuum.
2. Using Eqs. (A.1) and (A.2), express A and B via $\tilde{A}$ and $\tilde{B}$. These are the equations expressing a and b in terms of $\tilde{a}$ and $\tilde{b}$. Conjugate these equations to express $a^\dagger$ and $b^\dagger$ in terms of $\tilde{a}^\dagger$ and $\tilde{b}^\dagger$.
3. Substitute the operators $a^\dagger$ and $b^\dagger$ used in the step 1 by their expressions in terms of $\tilde{a}^\dagger$ and $\tilde{b}^\dagger$ obtained in step 2. This substitution gives $|\Psi_{\rm out}\rangle$.

Now let us apply this substitution method to find the resulting state in the receiving resonator when an arbitrary quantum state is transferred from the emitting resonator.

A.1 Transfer of an arbitrary quantum state

Let us assume that the initial state $|\psi_{\rm in}\rangle$ in the emitting resonator is

$$|\psi_{\rm in}\rangle = \sum_n \alpha_n |n\rangle = \sum_n \frac{\alpha_n (a^\dagger)^n}{\sqrt{n!}} |0\rangle, \;\; \sum_n |\alpha_n|^2 = 1, \tag{A.3}$$

while all other fields involved in the transfer procedure are vacua (in particular, this assumes zero temperature). Then the two-arm input state $|\Psi_{\rm in}\rangle$ for the beam splitter is the same, except the vacuum $|0\rangle$ in Eq. (A.3) is now understood as the vacuum $|\mathbf{0}\rangle$ for all possible modes.

The transfer procedure is characterized only by the efficiency η and the phase $\varphi_{\rm f} = \varphi_1$, while other phases φ_2 and φ_3 in Eqs. (A.1) and (A.2) are undefined. However, even though the resulting state $|\Psi_{\rm out}\rangle$ will depend on φ_2 and φ_3, the resulting density matrix $\rho_{\rm fin}$, obtained from $|\Psi_{\rm out}\rangle$ by tracing over the other output arm, will not depend on φ_2 and φ_3. This is because arbitrary φ_2 and φ_3 can be produced by placing phase shifters in the ancillary input and output arms (B-arm and $\tilde{B}$-arm in Fig. A.1); shifting the phase of vacuum in the B-arm does not produce any effect, while shifting the phase in the $\tilde{B}$-arm cannot affect $\rho_{\rm fin}$ by causality. We have also checked independence of $\rho_{\rm fin}$ on φ_2 and φ_3 by explicit calculations. Therefore, we can choose any values of φ_2 and φ_3. For convenience, let us choose $\varphi_2 = \pi$ and $\varphi_3 = 0$. Then using step 2 of the substitution method we obtain

$$a^\dagger = \sqrt{\eta}\, e^{i\varphi_{\rm f}} \tilde{a}^\dagger + \sqrt{1-\eta}\, e^{i\varphi_{\rm f}} \tilde{b}^\dagger, \tag{A.4}$$

$$b^\dagger = \sqrt{\eta}\, \tilde{b}^\dagger - \sqrt{1-\eta}\, \tilde{a}^\dagger, \tag{A.5}$$

while step 1 was Eq. (A.3). Now substituting $a^\dagger$ in Eq. (A.3) with the expression in Eq. (A.4) (step 3), we obtain

$$|\Psi_{\rm out}\rangle = \sum_{n,k} \alpha_{n+k} \sqrt{(n+k)!/(n!k!)}\, \eta^{n/2} (1-\eta)^{k/2} \\ \times e^{i(n+k)\varphi_{\rm f}} |n\rangle |k\rangle, \tag{A.6}$$

where in the notation $|n\rangle|k\rangle = [(\tilde{a}^\dagger)^n (\tilde{b}^\dagger)^k / \sqrt{n!k!}\,]\, |\mathbf{0}\rangle$ the second state corresponds to the ancillary second arm (upper arm in Fig. A.1).

The final state at the receiving resonator can be calculated by tracing $|\Psi_{\rm out}\rangle\langle\Psi_{\rm out}|$ over the ancillary state $|k\rangle$, thus obtaining the density matrix

$$\rho_{\rm fin} = \sum_{j,n,m} \alpha_{n+j} \alpha^*_{m+j} \sqrt{(n+j)!(m+j)!}/(j!\sqrt{n!m!}) \\ \times \eta^{(n+m)/2} (1-\eta)^j e^{i(n-m)\varphi_{\rm f}})\, |n\rangle\langle m|, \tag{A.7}$$

where the sums over j, n, and m are all from 0 to ∞. Note that this result has been derived for a pure initial state (A.3) in the emitting resonator. However, it is easy to generalize Eq. (A.7) to an arbitrary initial state $\rho_{\rm in}$ by replacing $\alpha_{n+j}\alpha^*_{m+j}$ with $(\rho_{\rm in})_{n+j,m+j}$.

To find the fidelity of the quantum state transfer for the initial state (A.3), we calculate the overlap $\langle\psi_{\rm in}|\rho_{\rm fin}|\psi_{\rm in}\rangle$, thus obtaining

$$F_{\rm st} = \sum_{j,n,m} \frac{\sqrt{(n+j)!(m+j)!}}{j!\sqrt{n!m!}}\, \alpha_n^* \alpha_m \alpha_{n+j} \alpha_{m+j}^* \\ \times \eta^{(n+m)/2}(1-\eta)^j e^{i(n-m)\varphi_{\rm f}}, \tag{A.8}$$

which is Eq. (5.9) in the main text. For a mixed input state $\rho_{\rm in}$ we can find the resulting state $\rho_{\rm fin}$ as discussed above and then use the Uhlmann fidelity definition [1] $F_{\rm st} = [{\rm Tr}\sqrt{\sqrt{\rho_{\rm in}}\,\rho_{\rm fin}\sqrt{\rho_{\rm in}}}]^2$.

If instead of an arbitrary state (A.3) we transfer a qubit state $|\psi_{\rm in}\rangle = \alpha_0|0\rangle + \alpha_1|1\rangle$, then in Eq. (A.6) there are only three terms because $\alpha_{n+k} = 0$ if $n+k > 1$. This reduces Eq. (A.6) to Eq. (5.10) in the main text. Similarly, Eq. (A.7) reduces to Eq. (5.11) and Eq. (A.8) reduces to

$$F_{\rm st} = |\alpha_0|^4 + \eta|\alpha_1|^2 + |\alpha_0|^2|\alpha_1|^2(1-\eta+2\sqrt{\eta}\cos\varphi_{\rm f}). \tag{A.9}$$

To average this fidelity over the Bloch sphere of the initial state, we can either average it over 6 points at the ends of the three axes (±X, ±Y, ±Z) or use the averaging formulas $\overline{|\alpha_0|^4} = \overline{|\alpha_1|^4} = 1/3$, $\overline{|\alpha_0|^2|\alpha_1|^2} = 1/6$, thus obtaining average state fidelity

$$\overline{F}_{\rm st} = \frac{3+\eta+2\sqrt{\eta}\cos\varphi_{\rm f}}{6}, \tag{A.10}$$

which can be converted into the process fidelity F_χ using the standard rule, $F_\chi = 1-(3/2)(1-\overline{F}_{\rm st})$.

A.2 Decrease of the average state fidelity due to photons in the environment

So far we have assumed the initial state of the receiving resonator and all environmental modes in Eq. (5.7) to be vacuum. A natural question is what happens when there are some photons in the environment (including the initial state of the receiving resonator). In particular, it is interesting to determine whether the average fidelity $\overline{F}_{\rm st}$ of the qubit state transfer can increase, or always decreases. Below we show that the average fidelity always decreases due to a non-vacuum state of the environment.

We consider a simplified model, in which the main input of the beam splitter in Fig. A.1 is in a qubit state $|\psi_{\rm in}\rangle = \alpha_0|0\rangle + \alpha_1|1\rangle$, while the second input (modeling the environment) is in an arbitrary state, so that the total state is

$$|\Psi_{\rm in}\rangle = (\alpha_0|0\rangle + \alpha_1|1\rangle) \sum_n \beta_n |n\rangle, \tag{A.11}$$

where $|\alpha_0|^2 + |\alpha_1|^2 = 1$ and $\sum_n |\beta_n|^2 = 1$. Neglecting for simplicity the transfer phase, $\varphi_{\rm f} = 0$, choosing the other phases as $\varphi_2 = \pi$ and $\varphi_3 = 0$, and using the substitution method described above, we find the output state

$$\begin{aligned} |\Psi_{\rm out}\rangle = \sum_{k,m} \frac{\sqrt{(k+m)!}}{\sqrt{k!m!}} \, \beta_{k+m} (-\sqrt{1-\eta})^m (\sqrt{\eta})^k \\ \times \Big[\alpha_0 |m\rangle|k\rangle + \alpha_1 \sqrt{\eta}\, \sqrt{m+1}\, |m+1\rangle|k\rangle \\ + \alpha_1 \sqrt{1-\eta}\, \sqrt{k+1}\, |m\rangle|k+1\rangle \Big]. \end{aligned} \tag{A.12}$$

We then trace over the ancillary arm state to find the resulting density matrix $\rho_{\rm fin}$, which can now contain non-zero elements $(\rho_{\rm fin})_{mn}$ for arbitrary m and n. However, the state fidelity for the qubit transfer depends only on the elements within the qubit subspace, $F_{\rm st} = |\alpha_0|^2(\rho_{\rm fin})_{00} + |\alpha_1|^2(\rho_{\rm fin})_{11} + 2\,{\rm Re}[\alpha_0^*\alpha_1(\rho_{\rm fin})_{01}]$. Averaging $F_{\rm st}$ over the initial qubit state [145, 146, 147], we obtain after some algebra

$$\overline{F}_{\rm st} = \frac{1}{6}(3+\eta+2\sqrt{\eta}) - \sum_{n=1}^{\infty} C_n(\eta)\,|\beta_n|^2, \tag{A.13}$$

$$\begin{aligned} C_n(\eta) &= \frac{1}{6}\big\{(3+\eta+2\sqrt{\eta})(1-\eta^n) \\ &\quad +n(1-\eta)\eta^{n-1}[2\eta+2\sqrt{\eta}-(1-\eta)(2n+1)]\big\}. \quad . \end{aligned} \tag{A.14}$$

The first term in Eq. (A.13) is the average fidelity when there are no photons in the environment [see Eq. (A.10) with $\varphi_{\rm f} = 0$], while the second term is due to the environmental photons ($|\beta_n|^2$ is the probability of having n photons). We numerically checked that the coefficients $C_n(\eta)$ are always positive for $n \geq 1$ and $\eta \in [0,1]$. Therefore, the presence of photons in the environment always decreases the average fidelity of a qubit transfer. Note that Eq. (A.13) does not depend on the choice of φ_2 and φ_3, since these phases can be produced by phase shifters in the ancillary B-arm and $\tilde{B}$-arm in Fig. A.1. The phase shifter in the $\tilde{B}$-arm cannot affect $\rho_{\rm fin}$, while the phase shifter in the B-arm changes only the phase of the ancillary input state and therefore does not change $|\beta_n|^2$ in Eq. (A.13).

In the case when $\eta \approx 1$, we can approximate Eq. (A.14) as $C_n(\eta) \approx (5/3)(1-\eta)\,n$. The average fidelity is then

$$\overline{F}_{\mathrm{st}} \approx 1 - \frac{1-\eta}{3} - \frac{5}{3}\,(1-\eta)\,\overline{n}_{\mathrm{e}}, \tag{A.15}$$

where $\overline{n}_{\mathrm{e}} = \sum_n n|\beta_n|^2$ is the average number of photons in the environmental mode. Note that the effect of non-zero $\overline{n}_{\mathrm{e}}$ is suppressed at $1-\eta \ll 1$. Equation (A.15) can be used for an estimate of the effect of finite temperature. However, we emphasize that modeling of the environmental noise with a single beam splitter is an oversimplification, so Eq. (A.15) gives a qualitative description, but is not intended to accurately describe the effect of environmental noise on the quantum state transfer protocol.

Appendix B

Tunable Coupler Theory

In this Appendix we consider the tunable coupler realized experimentally in Refs. [106, 107], and derive formulas for the transmission and refection amplitudes $\mathbf{t}$ and $\mathbf{r}^{\text{in}}$ used in Sec. 5.5.2. We also discuss the change of the resonator frequency due to the changing complex phase of $\mathbf{r}^{\text{in}}$. Since the theory is the same for both resonators, we omit the resonator index, assuming, e.g., the receiving resonator. The discussion in this Appendix follows the discussion in Sec. III of the Supplementary Information of Ref. [106].

There will be a difference in the choice of rotating frame between the main text and this Appendix. In the main text we use the rotating frame $e^{-i\omega t}$, which is standard in optics. However, in this Appendix we will need a language of impedances, which traditionally assumes the rotating frame $e^{i\omega t}$. Therefore, we will have to derive formulas for $\mathbf{t}$ and $\mathbf{r}$ in the rotating frame $e^{i\omega t}$, and then we will need to conjugate the final results to convert them into for $\mathbf{t}$ and $\mathbf{r}$ for the rotating frame $e^{-i\omega t}$.

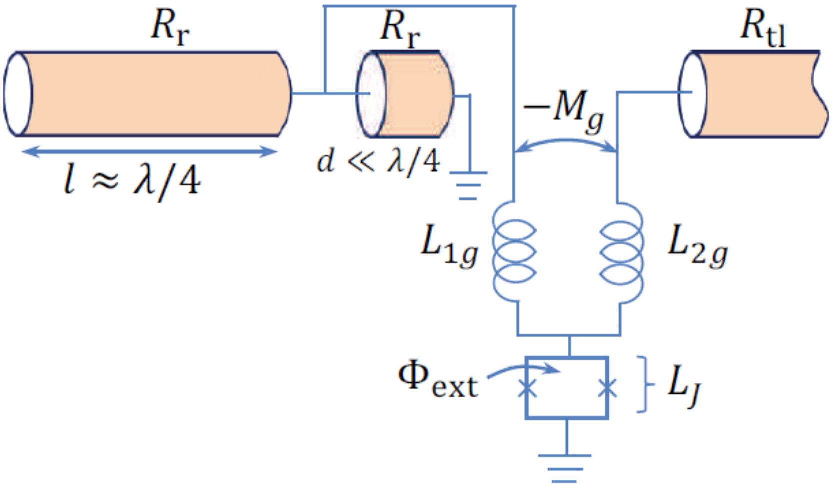

Figure B.1: Schematic of the tunable coupler of Refs. [106, 107] between the $\lambda/4$ microwave resonator (at the left) and the transmission line (at the right). A voltage taken at the distance d from the resonator end is applied to a transformer with a negative mutual inductance $-M_g$ and a SQUID providing positive Josephson inductance L_J. External flux Φ_{ext} controls L_J, thus controlling the effective mutual inductance $M = -M_g + L_J$. The wave impedances of the lines are R_{r} and R_{tl}.

The schematic of the tunable coupler is shown in Fig. B.1. A quarter-wavelength ($\lambda/4$) microwave resonator is divided into two unequal parts, and the voltage signal for the coupler is taken at the distance d ($d \ll \lambda/4$) from the end, which is shorted to the ground, while the other end is terminated with a break so that the total length is $l + d \approx \lambda/4$. The coupler consists of a transformer with geometrical inductances L_{1g} and L_{2g} and negative mutual inductance $-M_g$, which is in series with a dc SQUID, providing a positive Josephson inductance L_J. This inductance is controlled by an external magnetic flux Φ_{ext}, $L_J = \Phi_0/[2\pi\sqrt{I_{c1}^2 + I_{c2}^2 + 2I_{c1}I_{c2}\cos(2\pi\Phi_{\mathrm{ext}}/\Phi_0)}]$, where $\Phi_0 = h/2e$ is the magnetic flux quantum and I_{c1}, I_{c2} are the critical currents of two Josephson junctions, forming the SQUID. Thus the external flux controls the total mutual inductance

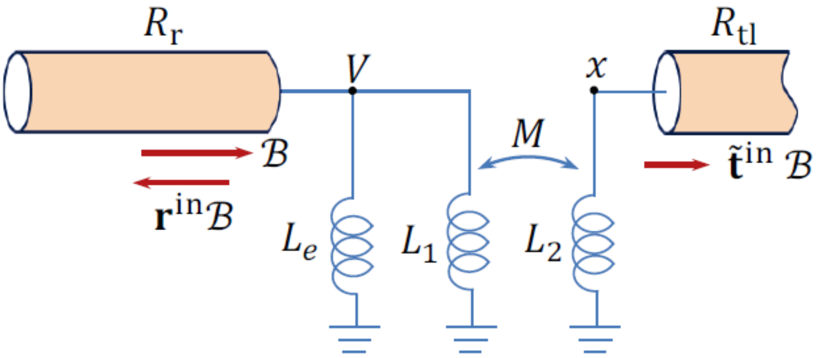

Figure B.2: The simplified schematic of Fig. B.1, with the d-long piece of the resonator replaced by inductance L_e, and the transformer in series with SQUID replaced by an effective transformer with mutual inductance M. An incident wave with voltage amplitude $\mathcal{B}$ creates voltages V and x across the inductors L_1 and L_2. The wave is reflected as $\mathbf{r}^{\rm in}\mathcal{B}$ and transmitted as $\tilde{\mathbf{t}}^{\rm in}\mathcal{B}$ (the superscript "in" indicates the wave coming from inside the resonator and the tilde sign indicates the actual transmission amplitude, as opposed to the effective amplitude $\mathbf{t}$). In our case $\mathbf{r}^{\rm in} \approx -1$ and $|\tilde{\mathbf{t}}^{\rm in}| \ll 1$.

$M = -M_g + L_J$, which determines the coupling between the resonator and transmission line; in particular, there is no coupling when $M = 0$. Note that the wave impedance $R_{\rm r}$ of the resonator may be different from the impedance $R_{\rm tl}$ of the transmission line.

For the analysis let us first reduce the schematic of Fig. B.1 to the schematic of Fig. B.2 by replacing the d-long part of the resonator with an effective inductance L_e and also replacing the transformer and SQUID with an effective transformer with inductances L_1, L_2, and mutual inductance M,

$$L_1 = L_{1g} + L_J, \quad L_2 = L_{2g} + L_J, \quad M = -M_g + L_J. \tag{B.1}$$

We emphasize that M can be both positive and negative, so the coupling changes sign when M crosses zero (the coupler is OFF when $M = 0$). Note that by varying M we also slightly change L_1 and L_2,

$$L_1 = L_{1g} + M_g + M, \quad L_2 = L_{2g} + M_g + M. \tag{B.2}$$

It is easy to calculate the effective inductance L_e. If there is no coupler ($L_1 = \infty$) and a voltage wave $\mathcal{B}e^{i\omega t}$ comes from the resonator side (from the left in Fig. B.1), then it is reflected as $-\mathcal{B}e^{i\omega t}$, and the voltage at a distance d is then $V = \mathcal{B}e^{i\omega t}[\exp(i\omega d/v) - \exp(-i\omega d/v)] = 2i\mathcal{B}e^{i\omega t}\sin(\omega d/v)$, where v is the speed of light in the resonator. The current (to the right) at this point is $I = (\mathcal{B}/R_\mathrm{r})e^{i\omega t}[\exp(i\omega d/v) + \exp(-i\omega d/v)] = 2(\mathcal{B}/R_\mathrm{r})\cos(\omega d/v)$. Therefore, the wave impedance is $Z = V/I = iR_\mathrm{r}\tan(\omega d/v)$, which is the same, $Z = i\omega L_e$, as for an inductance

$$L_e = \frac{R_\mathrm{r}}{\omega}\tan\frac{\omega d}{v} = \frac{R_\mathrm{r}}{\omega}\tan\frac{2\pi d}{\lambda}. \tag{B.3}$$

Next, let us calculate the transmission and reflection amplitudes $\tilde{\mathbf{t}}^\mathrm{in}$ and $\mathbf{r}^\mathrm{in}$ for the effective circuit shown in Fig. B.2. (Here the superscript "in" reminds us that the wave is incident from inside of the resonator, and the tilde sign in $\tilde{\mathbf{t}}^\mathrm{in}$ means that we consider the actual transmission amplitude, which is different from the effective amplitude $\mathbf{t}$). Assume that a voltage wave with amplitude $\mathcal{B}$ is incident onto the coupler from the resonator (we omit the exponential factor $e^{i\omega t}$). The wave is reflected as $\mathbf{r}^\mathrm{in}\mathcal{B}$ and transmitted as $\tilde{\mathbf{t}}^\mathrm{in}\mathcal{B}$. For a weak coupling, which we consider in this work (as continued from Ch. 5, $\mathbf{r}^\mathrm{in} \approx -1$ and $|\tilde{\mathbf{t}}^\mathrm{in}| \ll 1$. The voltage across L_1 is $V = (1 + \mathbf{r}^\mathrm{in})\mathcal{B}$, while the voltage across L_2 is denoted by x.

The current flowing into L_1 is $I_1 = (1 - \mathbf{r}^{\rm in})\mathcal{B}/R_{\rm r} - V/(i\omega L_e)$, while the current flowing (down) into L_2 is $I_2 = -x/R_{\rm tl}$. Using the currents I_1 and I_2, we write transformer equations for voltages x and V as

$$\begin{aligned} x &= i\omega M \left[\frac{(1-\mathbf{r}^{\rm in})\mathcal{B}}{R_{\rm r}} - \frac{(1+\mathbf{r})^{\rm in}\mathcal{B}}{i\omega L_e}\right] - i\omega L_2 \frac{x}{R_{\rm tl}}, && \text{(B.4)} \\ (1+\mathbf{r}^{\rm in})\mathcal{B} &= i\omega L_1 \left[\frac{(1-\mathbf{r}^{\rm in})\mathcal{B}}{R_{\rm r}} - \frac{(1+\mathbf{r}^{\rm in})\mathcal{B}}{i\omega L_e}\right] \\ &\qquad - i\omega M \frac{x}{R_{\rm tl}}. && \text{(B.5)} \end{aligned}$$

From these two equations we can find the reflection amplitude $\mathbf{r}^{\rm in}$ and the transmission amplitude $\tilde{\mathbf{t}}^{\rm in} = x/\mathcal{B}$ (note that $|\tilde{\mathbf{t}}^{\rm in}|^2 R_{\rm r}/R_{\rm tl} + |\mathbf{r}^{\rm in}|^2 = 1$):

$$\begin{aligned} \mathbf{r}^{\rm in} &= -\frac{1-b}{1+b}, && \text{(B.6)} \\ \tilde{\mathbf{t}}^{\rm in} &= i\frac{2\omega M}{1+b}\left(\frac{1}{R_{\rm r}} + \frac{ib}{\omega L_e}\right)\frac{1}{1+i\omega L_2/R_{\rm tl}}, && \text{(B.7)} \end{aligned}$$

where

$$\begin{aligned} b &= \frac{\dfrac{i\omega L_1}{R_{\rm r}} + \dfrac{\omega^2 M^2}{R_{\rm r} R_{\rm tl}(1+i\omega L_2/R_{\rm tl})}}{1 + \dfrac{L_1}{L_e} - \dfrac{i\omega M^2}{R_{\rm tl} L_e (1+i\omega L_2/R_{\rm tl})}} && \text{(B.8)} \\ &= \frac{i\omega L_1/R_{\rm r}}{\dfrac{L_1}{L_e} + \left[1 - \dfrac{i\omega M^2}{R_{\rm tl} L_1 (1+i\omega L_2/R_{\rm tl})}\right]^{-1}}. && \text{(B.9)} \end{aligned}$$

Note that the transmission and reflection amplitudes for the wave incident from outside of the resonator are

$$\tilde{\mathbf{t}}^{\rm out} = \frac{R_{\rm r}}{R_{\rm tl}}\,\tilde{\mathbf{t}}^{\rm in}, \;\; \mathbf{r}^{\rm out} = -\frac{\tilde{\mathbf{t}}^{\rm in}}{(\tilde{\mathbf{t}}^{\rm in})^*}\,\mathbf{r}^{\rm in}. \tag{B.10}$$

Since the transmission amplitude depends on the direction, it is convenient to introduce the effective amplitude $\mathbf{t}$, which does not depend on the direction,

$$\mathbf{t} = \sqrt{\frac{R_{\rm r}}{R_{\rm tl}}}\,\tilde{\mathbf{t}}^{\rm in} = \sqrt{\frac{R_{\rm tl}}{R_{\rm r}}}\,\tilde{\mathbf{t}}^{\rm out}, \;\; |\mathbf{t}|^2 + |\mathbf{r}^{\rm in(out)}|^2 = 1. \tag{B.11}$$

Equations (B.6)–(B.9) and (B.11) give us $\mathbf{t}$ and $\mathbf{r}$ in the rotating frame $e^{i\omega t}$. For the rotating frame $e^{-i\omega t}$ we need to conjugate $\mathbf{t}$ and $\mathbf{r}$ (and b), thus obtaining Eqs. (5.48)–(5.50) in the main text.

For an estimate let us use the following parameters (similar to the parameters of Ref. [106]): $R_{\rm r} = 80\,\Omega$, $R_{\rm tl} = 50\,\Omega$, $L_{1g} = L_{2g} = 480$ pH, $M_g = 140$ pH, $\omega/2\pi = 6$ GHz, and $L_e = 180$ pH (corresponding to $d/\lambda = 0.013$). Then Eqs. (B.6)–(B.9) and (B.11) for small M give $b \approx 0.066i$, $\mathbf{r}^{\rm in} \approx -e^{-0.13i}$, and $\mathbf{t} \approx 0.034ie^{-0.5i}M/M_g$. The resonator leakage time is then $\tau \approx (M_g/M)^2 \times 72$ ns.

Note that in the case when $\omega M \ll R_{\rm tl}$, we can replace the denominator of Eq. (B.9) with $L_1/L_e + 1$. Then

$$b \approx i\,\frac{\omega L_e/R_{\rm r}}{1 + L_e/L_1}, \tag{B.12}$$

and if $\omega L_e \ll R_{\rm r}$ (which means $d \ll \lambda/4$), then $|b| \ll 1$. In this case the reflection and effective transmission amplitudes (B.6) and (B.11) can be approximated (for the rotating frame $e^{i\omega t}$) as

$$\mathbf{r}^{\rm in} \approx -\exp\left[-\frac{2\omega L_e L_1}{R_{\rm r}(L_1+L_e)}\, i \right] \tag{B.13}$$

$$\mathbf{t} \approx i\, \frac{2\omega L_e M}{\sqrt{R_{\rm r} R_{\rm tl}}\,(L_1+L_e)}\, \frac{1}{1+i\omega L_2/R_{\rm tl}}. \tag{B.14}$$

The latter equation shows that in the first approximation the phase of $\mathbf{t}$ does not change with M, and for the case $\omega L_2 \ll R_{\rm tl}$ the value of $\mathbf{t}$ is close to being purely imaginary. Note that Eq. (B.14) uses the approximation $1+b \approx 1$ in the denominator of the first factor in Eq. (B.7). Without this approximation (still using the above formula for b), the factor L_1+L_e in the denominator of Eq. (B.14) should be replaced with a more accurate term $L_1+L_e+i\omega L_1 L_e/R_{\rm r}$. As we checked numerically, this gives a much better approximation for small M (mostly for the phase of $\mathbf{t}$), but there is no significant improvement of accuracy for intermediate values of M, corresponding to $|\mathbf{t}| \simeq 0.05$.

The resonator frequency $\omega_{\rm r}$ slightly changes when the mutual inductance M is varied, because this slightly changes the phase of the reflection amplitude $\mathbf{r}^{\rm in}$. The frequency change can be calculated as

$$\delta\omega_{\rm r} \approx 2\,\omega_0\, \frac{\delta(\arg \mathbf{r}^{\rm in})}{2\pi}, \tag{B.15}$$

where the factor of 2 comes from the assumption of a $\lambda/4$ resonator, and as ω_0 we choose the resonator frequency at $M=0$. [Note the sign difference compared with Eq. (5.51) because of the different rotating frame.]

To estimate the frequency change $\Delta\omega_{\rm r} = \omega_{\rm r}(M) - \omega_{\rm r}(0)$ to first order, we can expand Eq. (B.9) to linear order in M [which comes from changing L_1 in Eq. (B.12) – see Eq. (B.2)] and then use $\delta(\arg \mathbf{r}^{\rm in}) = -[2/(1+|b|^2)]\,\delta|b|$, which follows from Eq. (B.6) for a positive-imaginary b. Thus we obtain

$$\Delta\omega_{\rm r} \approx -\frac{\omega_0}{\pi}\,\frac{2}{1+|b|^2}\,\frac{\omega_0 L_e^2}{R_{\rm r}(L_1+L_e)^2}\,M, \tag{B.16}$$

where b is given by Eq. (B.12), and L_1 should be evaluated at $M=0$. Since $\mathbf{t}$ is also proportional to M in the first order [see Eq. (B.7)], the ratio $\Delta\omega_r/|\mathbf{t}|$ is approximately constant,

$$\frac{\Delta\omega_{\rm r}}{|\mathbf{t}|} \approx -\frac{\omega_0}{\pi}\,\frac{\sqrt{1+(\omega_0 L_2/R_{\rm tl})^2}}{\sqrt{1+|b|^2}}\sqrt{\frac{R_{\rm tl}}{R_{\rm r}}}\,\frac{L_e}{L_1+L_e}, \tag{B.17}$$

where L_1 and L_2 should be evaluated at $M=0$, and for typical experimental parameters $|b|^2$ can be neglected [we keep the very small terms with $|b|^2$ in Eqs. (B.16) and (B.17) to have exact formulas at $M\to 0$]. This formula describes the numerical dependence $\Delta\omega_{\rm r}(|\mathbf{t}|)$ shown in Fig. 5.12 very well, giving an exact result at $|\mathbf{t}|\to 0$ and a relative deviation of 3.2% at $|\mathbf{t}| = 0.1$. It is interesting that the dependences of $|\mathbf{t}|$ and $\Delta\omega_{\rm r}$ on M are both significantly nonlinear (see, e.g., the dashed line in Fig. 5.12); however, these nonlinearities partially compensate each other to produce a smaller nonlinearity in $\Delta\omega_{\rm r}(|\mathbf{t}|)$.

While Eq. (B.16) gives only the linear component of the dependence $\Delta\omega_{\rm r}(M)$, a better approximation can be based on using Eq. (B.12) to find $b(M) - b(0)$ and then convert it into $\Delta\omega_{\rm r}$ via Eq. (B.15). In this way we obtain

$$\Delta\omega_{\rm r} \approx -\frac{2\omega_0^2 L_e^2/(1+|b|^2)}{\pi R_{\rm r}(L_{1g}+M_g+L_e)(L_{1g}+M_g+L_e+M)}\,M, \tag{B.18}$$

in which the term $|b|^2$ can be neglected. This formula gives a nonlinear dependence $\Delta\omega_{\rm r}(M)$ due to the presence of M in the denominator. We checked that this formula correctly describes about 80% of the numerical nonlinearity of the $\Delta\omega_{\rm r}(M)$ dependence for the parameters of Fig. 5.12. There is a similar dependence on M in the denominator of Eq. (B.14) for $\mathbf{t}(M)$ dependence, thus explaining why the two nonlinearities partially cancel each other to produce a much more linear dependence $\Delta\omega_{\rm r}(|\mathbf{t}|)$ in Fig. 5.12.